



1980 North Atlantic Avenue • Suite 230 • Cocoa Beach, FL 32931 • 321-783-9735 • www.ensco.com

# **Global Environmental MEMS Sensors (GEMS): A Revolutionary Observing System for the 21<sup>st</sup> Century**

## **Phase I Final Report**

**Contract NAS5-98051  
Universities Space Research Association  
Grant Number 07600-093**

**Prepared for:  
NASA Institute for Advanced Concepts  
Atlanta, GA**

**Principal Investigator:**  
John Manobianco, Ph.D.  
manobianco.john@ensco.com

**2 December 2002**

## Executive Summary

Technological advancements in MicroElectroMechanical Systems (MEMS) have inspired a revolutionary observing system known as Global Environmental MEMS Sensors (GEMS). The GEMS concept features an integrated system of MEMS-based airborne probes that will be designed to remain suspended in the atmosphere for hours to days taking in situ measurements over all regions of the Earth with unprecedented spatial and temporal resolution. The GEMS concept is revolutionary because it foresees the future integration of evolving technologies to realize an observing system with scalability and applicability over a broad range of weather and climate phenomena. GEMS have the potential to expand our understanding of the Earth and improve weather forecast accuracy and efficiency well beyond current capability. Resulting improvements in forecast accuracy will translate directly into cost benefits for weather-sensitive industries worldwide, and mitigate the risk factors associated with life-threatening weather phenomena.

This final report summarizes the NASA Institute for Advanced Concepts (NIAC) Phase I project, focusing on validating the viability of GEMS and defining the major feasibility issues including probe design, power, communication, navigation, networking, measurement, deployment, dispersion, data impact, data collection and management, costs, and environmental concerns. Assessing the optimum probe design and deployment strategy requires an interdisciplinary collaboration to examine complex trade-off issues such as the number of probes necessary for communication and networking, development and manufacturing costs, and the impact of probe observations on forecast accuracy. The framework for a simulation-design-test (SDT) cycle was developed in Phase I as a cost-effective and controlled way to explore the trade-offs.

Each probe will be self-contained with a power source consisting of batteries, fuel cells, and/or solar power to provide sensing, data processing/computation, location/navigation, and communication functions. Materials science will play a key role to limit probe mass and potentially make them biodegradable or at least bioinert, thereby minimizing risks to the environment when the probes settle out of the atmosphere. The probes are envisioned to be mass produced at very low per-unit cost in 20 years.

Based on specific applications, the probes will be designed as small as 50–100 microns in one or more dimensions and lightweight enough to pose virtually no danger upon contact with persons or property. The size, mass, aspect ratio, component geometry, buoyancy control, and aerodynamic design will all determine how long probes remain airborne. Buoyancy control could be the most effective way to reduce the terminal velocity of probes and keep them suspended for much longer periods of time. The probes will have to be robust enough to ensure that the electronics are isolated from the effects of liquid and frozen water, dust, chemical pollutants, radiation, static electricity, and thermal noise. It is currently feasible for MEMS-based temperature, humidity, and pressure measurements to be modified for use in integrated, low-power applications such as GEMS.

The probes will communicate with other probes, remote receiving platforms, and data collectors using Radio Frequency (RF) and/or optical frequency transmissions to form a wireless, mobile, in situ network. As part of a wireless network, the probes will not require recovery to collect data and therefore will be disposable. With active RF transmissions, the power requirements are projected to be 100 times greater than free-space optical communication. Communication using optical frequencies can realize higher antenna gains than RF when the wavelength is small; however, optical signals cannot penetrate areas of dense cloud cover.

A critical challenge for GEMS is to define a viable networking solution given available power and probe separation. The separation distance, power constraints, and communication range will determine if each probe can transmit to a remote receiving platform or if mobile networking via multihop routing is viable. Global Positioning System (GPS)-aided inertial navigation and network localization will both be viable long-term options for probe navigation. Advances in GPS satellite technology and the implementation of GPS satellites that broadcast stronger signals could dramatically reduce the energy requirements for making probe position measurements. With network localization, only a fraction of the probes would have knowledge of their locations, and the remaining probes would estimate their positions dynamically.

Deployment of GEMS is envisioned from both ground sites and airborne platforms. The grand vision is to design a deployment strategy that could sustain global coverage. To explore the issues related to probe deployment and dispersion, a numerical weather prediction model coupled with a Lagrangian particle model was configured to run over most of the northern hemisphere for a period of 24 days, and simulate probe release from a hypothetical network of high altitude balloons. This simulation demonstrated that the large-scale atmospheric circulation patterns could disperse probes throughout the northern hemisphere in just 10 days with such a deployment scenario.

Observing system simulation experiments were used to assess the impact of simulated probe data on regional forecasts for a day with active convection over the Florida peninsula. The assimilation of probe data resulted in a substantial reduction of forecast errors and improvements in predicted precipitation patterns. Excluding GEMS temperature, humidity, or wind data significantly degraded the model forecast not only for the parameter excluded, but for the precipitation forecast as well. This sensitivity test indicated that, at least for the case studied, the maximum data impact resulted when GEMS provided a full suite of temperature, moisture, pressure, and wind measurements.

To achieve the global grand vision for GEMS could require as many as  $10^{10}$  airborne probes at any given time, assuming an average horizontal and vertical probe spacing of  $\sim 1$  km from the surface up to about 20 km above ground level. A rough estimate of the data rate produced by GEMS for a network with  $10^{10}$  probes would be  $\sim 10^{12}$  observations per day, assuming temperature, pressure, humidity, and wind velocity are measured once per hour. Although projected data rates from a network of that size are comparable with future observing systems in the next decade, significant advances in computing architectures, model/data assimilation systems, speed/bandwidth of communication systems, and data management algorithms will be needed to support such systems.

## Table of Contents

Executive Summary.....	ii
Table of Contents .....	iv
List of Figures .....	vi
List of Tables.....	viii
List of Tables.....	viii
1 Introduction .....	1
2 Concept Description .....	1
2.1 Historical Perspective.....	3
2.2 Limitations in Current Meteorological Observing Capabilities .....	3
2.3 Revolutionary Aspects of the Concept.....	3
2.4 Expected Significance.....	4
2.5 Previous Work Done .....	4
3 MEMS .....	5
3.1 Overall Design .....	5
3.2 Power .....	5
3.2.1 Batteries .....	6
3.2.2 Fuel Cells.....	7
3.2.3 Solar.....	8
3.2.4 Directed RF.....	9
3.2.5 Combustion.....	9
3.3 Communication.....	9
3.3.1 RF Communication.....	9
3.3.2 Optical Communication .....	12
3.4 Networking .....	17
3.5 Sensors .....	17
3.5.1 Current Technology .....	17

3.5.2	Temperature .....	18
3.5.3	Humidity .....	19
3.5.4	Pressure .....	19
3.5.5	Gas Sensors .....	20
3.6	Navigation .....	21
3.6.1	Existing GPS .....	21
3.6.2	Inertial Navigation .....	22
3.6.3	Future GPS .....	22
3.6.4	Localization .....	22
4	System Modeling .....	23
4.1	Numerical Weather Prediction Model .....	23
4.2	Probe Dispersion .....	24
4.3	Deployment Strategy .....	25
4.4	Simulated Observations .....	26
4.5	Observing System Simulation Experiments (OSSEs) .....	26
4.5.1	Methodology .....	26
4.5.2	Results .....	33
5	Other Issues .....	44
5.1	Hemispheric Deployment .....	44
5.2	Data Collection and Data Rate .....	46
5.3	Preliminary Cost Comparison with Other Future Observing Systems .....	47
5.4	Environmental Impact .....	48
6	Summary .....	48
7	Future Direction .....	50
8	Acknowledgements .....	51
9	References .....	52
	List of Abbreviations .....	58

## List of Figures

<b>Figure 2.1</b>	Conceptualization of GEMS illustrating both a global and local distribution of probes with communication and networking between probes and data collectors. ....	2
<b>Figure 3.1</b>	Lithium battery chemistry comparison (Tadiran 2002). ....	6
<b>Figure 3.2</b>	Zinc-air battery cross section from Eveready (2002b). Note in particular the air hole on the bottom surface. ....	8
<b>Figure 3.3</b>	Schematic of an aluminum-air fuel cell and of a zinc-air fuel cell. ....	8
<b>Figure 3.4</b>	A 2.4-GHz RF-ID tag with a 1024-bit read/write memory and a communication range of a few meters. ....	9
<b>Figure 3.5</b>	Signal strength versus distance for cellular telephones (from Lee 1995). ....	10
<b>Figure 3.6</b>	Typical low-frequency RF-ID tag system. ....	11
<b>Figure 3.7</b>	The Hitachi MY1007, an RF-ID system on a chip with no external components. ....	12
<b>Figure 3.8</b>	A dual-band 900/1800 MHz fractal antenna. ....	12
<b>Figure 3.9</b>	8mm <sup>3</sup> integrated MEMS laser transmitter. ....	14
<b>Figure 3.10</b>	Current beam steering devices (from left to right): voice-coil 2-axis mirror, 1- and 2- axis galvanometric scanners, and 1- and 2-axis piezoelectric fast-steering mirrors. ....	15
<b>Figure 3.11</b>	Three-axis MEMS gyroscope illustrating how all inertial sensors and control electronics are integrated on a single die (IMI 2002). ....	15
<b>Figure 3.12.</b>	VCSEL array. Circular regions are active regions of lasers (Lei et al. 1999). ....	16
<b>Figure 3.13</b>	RS90 radiosonde and sensor boom close-up (Vaisala 2002). ....	18
<b>Figure 3.14</b>	Inner detail of an RS80 radiosonde (from NSIDC 2002). ....	18
<b>Figure 3.15</b>	An interdigitated electrode. ....	19
<b>Figure 3.16</b>	Drive voltage vs. pressure from Gtierrez et al. (2001). ....	20
<b>Figure 3.17</b>	Piezoresistive cantilever array from Nascatec (2002). ....	21
<b>Figure 4.1</b>	Locations of the GEMS probe deployment and assimilation domains nested within the 4-km ARPS Nature simulation domain. ....	27
<b>Figure 4.2</b>	Three-dimensional display of the initial probe distribution at 1200 UTC 15 June 2001. ....	28
<b>Figure 4.3</b>	The number of probes as a function of time and altitude in the (a) deployment domain (outer dashed box in Fig. 4.1), and (b) assimilation domain (inner dotted box in Fig. 4.1). ....	28
<b>Figure 4.4</b>	Grid configuration for the ARPS Control and OSSE simulations. ....	29
<b>Figure 4.5</b>	Timeline of the Nature run for extracting simulated GEMS observations, the Control forecast, and OSSE experiments conducted on 15–16 June 2001. ....	31
<b>Figure 4.6</b>	Flowchart for the Control and OSSE forecast / DA cycle. ....	32
<b>Figure 4.7</b>	Graphs of the dew point root mean square (RMS) error and bias (Kelvin) for the Control and OSSE experiments 1 through 7. ....	36
<b>Figure 4.8</b>	Graphs of the temperature root mean square (RMS) error and bias (Kelvin) for the Control and OSSE experiments 1 through 7. ....	37
<b>Figure 4.9</b>	Graphs of the v-wind component root mean square (RMS) error and bias (m s <sup>-1</sup> ) for the Control and OSSE experiments 1 through 7. ....	38
<b>Figure 4.10</b>	Two-hour accumulated precipitation (mm) for the Nature simulation (a-d), Control simulation (e-h), Experiments 1 (i-l), and Experiment 2 (m-p). ....	40

<b>Figure 4.11</b>	Two-hour accumulated precipitation (mm) for the Nature simulation (a-d), Experiment 3 (e-h), Experiment 4 (i-l), and Experiment 5 (m-p).....	41
<b>Figure 4.12</b>	Two-hour accumulated precipitation (mm) for the Nature simulation (a-d), Experiment 6 (e-h) and Experiment 7 (i-l).....	42
<b>Figure 4.13</b>	Grid-averaged 2-hour accumulated precipitation (mm) for each ARPS simulation (Nature, Control, and Experiments 1 through 7) over the domain shown in Fig. 4.10. ....	43
<b>Figure 5.1</b>	Domain for the hemispheric ARPS simulations and probe positions at 1200 UTC 25 June 2001, 10.5 days after the model initialization time .....	44
<b>Figure 5.2</b>	Three-dimensional display of probe positions at 1200 UTC 25 June 2001 over the subset region delineated by the quadrilateral in Figure 5.1.....	45
<b>Figure 5.3</b>	The probe distribution as a function of time and altitude over the hemispheric domain shown in Figure 5.1.....	46

## List of Tables

<b>Table 3.1</b>	Energy densities of potential power sources in Watt-hours $\text{kg}^{-1}$ .....	6
<b>Table 3.2</b>	Optical link budgets. ....	13
<b>Table 4.1</b>	Summary of dynamical and physical features of the ARPS.....	24
<b>Table 4.2</b>	Resolution and coverage of terrain, soil, and vegetation data sets used in the ARPS simulation experiments. ....	24
<b>Table 4.3</b>	Summary of ARPS grid configurations for the Nature and Control simulations.....	29
<b>Table 4.4</b>	Summary of the simulations and OSSE experiments for 15–16 June 2001.....	33
<b>Table 5.1</b>	Variable specifications for each probe.....	46
<b>Table 6.1</b>	Key issues and enabling technologies affecting the design and development of GEMS.....	48

## 1 Introduction

Technological advancements in MicroElectroMechanical Systems (MEMS) have inspired the concept for a revolutionary new observing system called Global Environmental MEMS Sensors (GEMS). The GEMS concept is revolutionary because it foresees the future integration of evolving technologies to realize an observing system with scalability and applicability over a broad range of weather and climate phenomena that impact mankind. One of the key technologies is MEMS that combine electrical functions with sensors and other mechanical devices embedded in semiconductor chips.

GEMS have the potential to expand our understanding of the Earth system and improve weather forecast accuracy and efficiency well beyond current capability. Resulting improvements in forecast accuracy will translate directly into cost benefits for weather-sensitive industries worldwide, and mitigate the risk factors associated with life-threatening weather phenomena.

This final report summarizes the NASA Institute for Advanced Concepts (NIAC) Phase I GEMS project covering the period from 1 May through 30 October 2002. The Phase I effort focused on validating the viability of the GEMS concept and defining the major feasibility issues. The report is organized as follows. Section 2 provides concept description, background, expected significance and a summary of previous work done. Section 3 discusses the MEMS and engineering issues necessary for system design and development. Section 4 provides details of system modeling used to explore issues related to probe deployment/dispersion and the impact of simulated probe data on regional weather forecasts. Issues relating to environmental impact, data collection and data rates, and preliminary cost comparisons with other future observing systems are presented in Section 5. The report concludes with a summary of the Phase I work in Section 6 and plans for the Phase II project in Section 7.

## 2 Concept Description

The GEMS concept features an integrated system of MEMS-based probes that are envisioned to be mass produced at very low per unit cost in 20 years. The probes will be designed to remain suspended in the atmosphere for hours to days and take measurements of pressure, temperature, humidity, and wind velocity as they are carried by atmospheric currents. In addition to gathering meteorological data, the probes could be used for monitoring and predicting the dispersion of particulate emissions, organic and inorganic pollutants, ozone, carbon dioxide, and chemical, biological, or nuclear contaminants. Once the probes settle out of the atmosphere, they could continue taking surface measurements over land or water.

Based on specific applications, the probes will be as small as 50-100 microns in one or more dimensions and lightweight enough to pose virtually no danger upon contact with persons or property. Material science will play a key role to limit probe mass and potentially make them biodegradable or at least bioinert, thereby minimizing risks to the environment when the probes settle out of the atmosphere. The intricacy in nature has inspired us to explore nanobiotechnology as a possible means from which to create materials suitable for the probes. Nanobiotechnology merges biological systems with nanofabrication. For example, organic cells feature complex “machines” and systems that may guide the design and functionality of micro and nanoscale devices and components (Soong et al. 2000). Future advancements in materials science and nanotechnology could pave the way for the design and development of morphing probes that could change shape using smart materials and structures. Materials with morphing capabilities may enable probes to remain airborne for longer periods of time.

Each probe will be self-contained with a power source to provide sensing, data processing/computation, location/navigation, and communication functions. Since each probe will include sensors to measure all weather variables, there is significant redundancy if a single probe in the network fails. Sensing of pressure, temperature, and humidity on the probes will be accomplished using MEMS and/or nanotechnology-based hardware. Atmospheric wind velocity will be measured based on changes in probe position determined using a Global Positioning System (GPS)-aided Inertial Navigation System (INS) and network localization. With network localization, only several probes have knowledge of their locations while the remaining ones estimate their relative positions dynamically using on-board algorithms (Savvides et al. 2001).

The probes will communicate with other probes, intermediate nodes, data collectors (i.e. “mother ships”), and remote receiving platforms using radio and optical frequency transmissions to form a wireless, mobile, in

situ network (Fig. 2.1). As part of a wireless network, the probes will not require recovery to collect data and therefore will be disposable. The data collectors are envisioned to be larger than individual probes and distributed throughout the atmosphere. There will likely be intermediate nodes in the hierarchy as well, capable of longer-range communication and/or more data processing than the individual probes, but still autonomous. The largest data collectors are envisioned to be a series of ground- and space-based receiving platforms that relay data from the intermediate nodes and provide a means to acquire and process data within wired regional and/or global terrestrial networks.

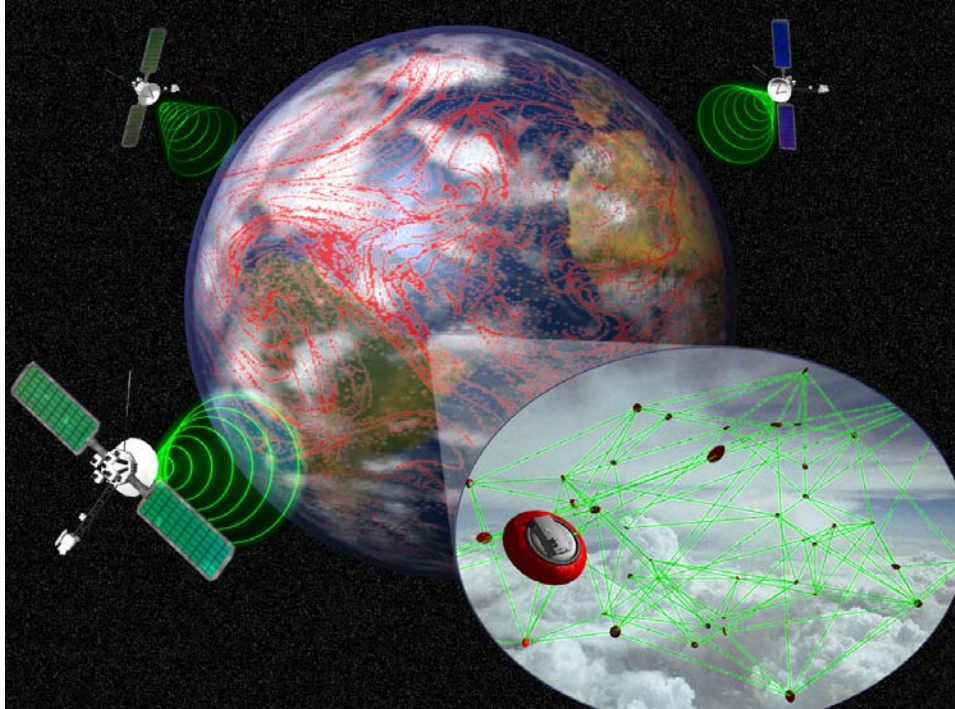


**Figure 2.1** Conceptualization of GEMS illustrating both a global and local distribution of probes with communication and networking between probes and data collectors.

The size, mass, aspect ratio, component geometry, buoyancy control, and aerodynamic design will all determine how long probes remain airborne. Buoyancy control could be the most effective way to reduce the terminal velocity of probes and keep them suspended for much longer periods of time. Recent work by Chambers et al. (1998) and Chen et al. (1999) demonstrated that hydrogen storage on nanocrystalline materials might be used to regulate buoyancy. Depending on the size and shape of the probes, aerodynamic design could also reduce their ballistic coefficient and terminal velocity. Many examples of such design exist in the natural world, including simple dandelion spokes and threads of balloon spiders, as well as sophisticated evolved forms like the auto-rotating samaras (Walker 1981).

Deployment of GEMS is envisioned from both ground sites and airborne platforms such as aircraft, unmanned aerial vehicles (UAVs), conventional weather balloons, and high altitude balloons (Girz et al. 2002; Pankine et al. 2002). There are numerous scenarios where high spatial and temporal resolution data would be valuable to assess the potential for and development of high impact weather such as tornadoes, severe thunderstorms, and hurricanes, or to support special operations in data limited or data denied regions. The grand vision is to design a deployment strategy that could sustain global coverage. To achieve the grand vision could require as many as  $10^{10}$  airborne probes at any given time, assuming an average horizontal and vertical probe spacing of  $\sim 1$  km from the surface up to about 20 km above ground level. The same number of probes over the volume of the atmosphere covering the state of Texas would provide measurements at an average spacing of 100 m. Clearly, such a concept stretches the imagination and involves many issues regarding feasibility, practicality, potential environmental impacts, and cost-benefit trade-offs.

A rough estimate of the data rate produced by GEMS for a regional or global network with  $10^{10}$  probes would be  $\sim 10^{12}$  observations per day, assuming temperature, pressure, humidity, and wind velocity are measured once per hour. Projected data rates from a network of that size are comparable with future observing

systems in the next decade (Uccellini et al. 2001; NASA 2002). To support such a vision for GEMS and/or other future observing systems will require significant advances in computing architectures, model/data assimilation (DA) systems, speed/bandwidth of communication systems, and data management algorithms including new paradigms for data mining, sampling and selection techniques (Clausen et al. 2002; NASA 2002). The projected advances in these areas will be important considerations in developing a technology roadmap for GEMS planned for the Phase II effort.

## **2.1 Historical Perspective**

The field of meteorology has been revolutionized by many unprecedented technological breakthroughs during the past two centuries. Our increased understanding of atmospheric processes resulting from these technological breakthroughs has led to vast improvements in the accuracy of weather forecasts, and subsequent protection of life and property. Dating back to 1870, the telegraph enabled the development of synoptic meteorology and the creation of surface weather maps. Weather balloons led to the analysis of the atmosphere in three dimensions, enabling our understanding of the vertical structure in features such as fronts and jet streams. Weather radars revolutionized the forecaster's ability to monitor, track, and issue warnings for severe thunderstorm and tornadoes.

With the advent of the computer age, meteorologists were provided with automated forecast guidance from numerical weather prediction (NWP) models capable of rapidly solving the equations of atmospheric motion, and integrating these solutions forward in time. Tremendous advances in forecast accuracy have been made ever since the advent of NWP. The beginning of the space age and rocket propulsion allowed for geostationary and polar-orbiting satellites to provide remote sensing of clouds, temperatures, and other parameters with nearly continuous regional to global coverage, improving our awareness of features such as tropical storms and local convection for the past 40 years. While the field of meteorology has continued to evolve in recent years, it has not realized the benefit of any revolutionary technological breakthroughs for decades.

## **2.2 Limitations in Current Meteorological Observing Capabilities**

Significant progress has been made in observing the atmosphere at finer spatial and temporal scales over many areas of the world; however, in situ observations are not distributed evenly around the globe, and are sparse over oceans, high latitudes, and politically sensitive regions. Space-based observing technology such as Low Earth Orbiting (LEO) satellites currently provide high spatial resolution, but suffer from inadequate temporal resolution, insufficient vertical resolution, and uncertain or unknown calibration and accuracy between years (Unninayar and Schiffer 1997). The most sophisticated current-generation sensors (e.g. ground or space-based lidars and infrared instruments) do not provide all-weather capability since they cannot penetrate optically thick clouds.

NWP models have become increasingly important to generate forecast guidance for operational meteorologists since their introduction over four decades ago (Shuman 1989). Satellites, radars, and other remote sensors do not currently provide a complete data set required to initialize NWP models since they measure radiance or reflectivity instead of model dependent variables such as temperature and moisture. Because of these limitations, operational centers are required to use complex and computationally expensive DA methods to transform measurements from remote sensors into dependent variables to initialize models.

Technological advances in computer speed and memory size over the past few decades have enabled significant reductions in horizontal and vertical grid spacing, advancements in model physics, and development of more sophisticated procedures to initialize NWP models. This trend of increasing complexity in weather models has resulted in improved weather forecasts; however, chaotic systems like the Earth's atmosphere have a limit of predictability even with perfect models due to differences between the true and observed state of the atmosphere (Lorenz 1969). Without high-resolution observational data to improve the initial conditions, progress toward attaining the theoretical upper limit of predictability with NWP models will likely be halted prematurely. Overcoming limitations with current meteorological sensor technology and providing observation capabilities that are commensurate with advances in NWP models will require revolutionary technologies such as GEMS to gather and transmit real-time weather data. GEMS can enable that revolution.

## **2.3 Revolutionary Aspects of the Concept**

While GEMS will likely complement the current and even next-generation suite of in situ sensors and ground/space-based remote sensing platforms, the concept is revolutionary because it will:

- Provide a 100-fold increase in the horizontal resolution of current in situ, tropospheric, and lower stratospheric observations that are most easily assimilated by NWP models,
- Use the natural dispersive characteristics of the atmosphere to transport probes into regions where it is not practical or possible to obtain data and where very few or no in situ observations currently exist,
- Provide observing capabilities spanning an extremely broad range of temporal and spatial scales from the detailed life cycle of individual clouds through planetary-scale weather and climate change, and
- Be much more cost effective than existing in situ platforms such as aircraft, which can obtain high spatial and temporal resolution measurements, but only over limited domains and at high costs.

## 2.4 Expected Significance

The Department of Commerce estimates that \$3 trillion dollars of the U.S. economy has weather and climate sensitivity (Dutton 2002). For example, the best hurricane track forecasts still have errors of more than 200 nautical miles at 72 hours; thus, over-warning of affected areas is required to account for such uncertainty (Franklin et al. 2001). Since it costs more than half of a million dollars to evacuate one linear mile of coastline (OFCM 1997), a 10% reduction in forecast track errors would result in a potential savings of at least \$10 million for each storm affecting populated areas. In addition, severe weather is estimated to cause billions of dollars in damages annually throughout the U.S. (Pielke et al. 1997); so there are enormous economic incentives to improve the forecasts of high impact weather events. Ultra-high spatial and temporal resolution measurements could lead to dramatic improvements in basic science including a more thorough understanding of physical processes in the atmosphere (e.g. cloud physics) and thereby improved representation of such processes in NWP models. A long-term observational database from GEMS could prove valuable to monitor climate changes.

Weather-sensitive customers worldwide including those in areas of ground transportation, agriculture, aviation, utilities, insurance, air quality monitoring, operational/research meteorology, and other earth sciences could benefit from improved observations and forecasts enabled by GEMS. With a modular sensor suite, probes could be used to measure acoustic, chemical, biological, nuclear, or other parameters of interest to defense agencies for intelligence gathering, battlefield situational awareness, and urban warfare monitoring. The probes could monitor oceans, rivers, and other surface water bodies as well as take measurements on land once they complete the airborne portion of their mission.

## 2.5 Previous Work Done

The design and development of prototype, millimeter-scale probes using MEMS sensors has been the focus of the “Smart Dust” project at University of California (UC) Berkeley since 1998 (Kahn et al. 2000). Kahn et al. (2000) envision numerous applications for smart dust and suggest that air currents could transport the probes to record meteorological observations for as long as they remain suspended in the atmosphere. Engineers at the Center for Wireless Integrated Microsystems (University of Michigan) have developed an integrated gas chromatography system operating at 1 milliwatt of power in a volume of 1 cubic centimeter, capable of detecting over 40 specific gases (Adrian 2001).

The probe size is important because the devices must ultimately be small enough to remain suspended in the atmosphere for periods of time on the order of hours to days. At the current millimeter size, a probe deployed at 20-km altitude would reach the ground in less than 0.5 hours in the absence vertical air motion. Under identical conditions, a probe size on the order of 100  $\mu\text{m}$  would take nearly 70 hours to fall from the same altitude. Studies of natural aerosols such as African dust and volcanic ash indicate that micron-size particles remain suspended in the atmosphere for days to weeks (Sarna-Wojcicki et al. 1981; Prospero 1999).

### 3 MEMS

In order to substantiate the GEMS concept, the Phase I effort focused on defining the major feasibility issues for miniaturizing the volume of current prototypes, describing baseline parameters, and providing realistic projections for probe characteristics as described in the following subsections. Assessment of the optimum probe design and deployment requires an interdisciplinary collaboration to examine complex trade-off issues such as the number of probes necessary for communication and networking, development and manufacturing costs, and the impact of probe observations on forecast accuracy. The large number of possible trade-offs constitutes a multi-dimensional parameter space. Because of the high dimensionality and complexity of the parameter matrix, it is not reasonable to examine every possible combination and permutation. The framework for a simulation-design-test (SDT) cycle was developed in Phase I as a cost-effective and controlled way to explore the trade-offs.

#### 3.1 Overall Design

A global network of wireless probes distributed in the atmosphere will require a variety of system components. The probes themselves are the critical element, but at a minimum, they will communicate with some form of data collection nodes. The hierarchy will most likely include intermediate nodes capable of longer-range communication and/or more data processing than the individual probes, but still autonomous. In the simplest scenario, the data collection terminals could be other probes that are plugged into an internet-connected computer. These fixed nodes would be part of the overall peer-to-peer network of airborne probes, and transmit their data from the wireless atmospheric network into the wired terrestrial network.

Probes will consist of at least the following subsystems: sensing, sensor data processing, power, and communication. In addition, there may be dedicated subsystems for location/navigation and other functions. Sensing on the probes will be accomplished using MEMS and/or nanotechnology-based hardware. Micromachined sensors for temperature and barometric pressure are already widely available commercially. Miniature humidity sensors, including a MEMS dew-point hygrometer, have already been demonstrated (Hoenk et al. 1996).

Sensor data processing includes the analog front-end circuitry to amplify, filter, and digitize the sensor signals, as well as the digital back-end circuitry to filter, calibrate and compensate, analyze, and compress the sensor data. Of these functions, fundamental lower limits on power consumption apply to the analog front end. These limits create a real, and in some cases severe, limit to the miniaturization of wireless probes because of the requirements on the power supply. While there are also fundamental limits on the power associated with digital computation, they are in general so many orders of magnitude below the limits to the analog front-end that they will be ignored.

Communication from probes to the data collection terminals will be achieved by a combination of Radio Frequency (RF) and optical methods, using peer-to-peer networking between the probes as well as possibly relaying through larger autonomous atmospheric nodes and satellites in a hierarchical system.

As part of the Phase II effort, a complete probe power budget will be developed to study the enabling technologies and the trade-offs in communication, networking, computation, sensing, and navigation that will impact system design, cost, practicality, and feasibility.

#### 3.2 Power

Power for the probes will come from a combination of batteries, fuel cells, and solar power. Battery series resistance will be a problem at the very cold temperatures of the upper atmosphere. Currently demonstrated power systems are sufficient to supply the energy densities illustrated in Table 3.1.

Table 3.1 Energy densities of potential power sources in Watt-hours kg <sup>-1</sup> .		
Material system	Energy density (Wh kg <sup>-1</sup> )	Comments
Alkaline batteries	120	
Lithium (rechargeable)	150	Commercially available
Lithium (primary) Thionyl Chloride	740	Commercially available Large temperature range
Zinc/air	400	Commercially available
Aluminum/air	800	Demonstrated
	8,000	Material limit
Methane	13,900	Material limit
Gasoline	12,700	Material limit
Hydrogen	40,000	Material limit

### 3.2.1 Batteries

Compared to alkaline batteries with an energy density of ~120 Watt-hours (Wh) kg<sup>-1</sup>, lithium/FeS<sub>2</sub> batteries provide 200 Wh kg<sup>-1</sup> at 1.3 V with a temperature range of -20° C to 60° C. LiCoO<sub>2</sub> provide 300 Wh kg<sup>-1</sup>, whereas lithium ion rechargeable batteries provide 150 Wh kg<sup>-1</sup> at 3.5 V.

The best off-the-shelf lithium batteries available today are lithium-thionyl-chloride that provide 740 Wh kg<sup>-1</sup> at a nominal 3.6 V. This chemistry is still able to provide reasonable current densities even above 3 V and -50° C, and is also stable up to above 85° C, making it the most attractive of the established battery chemistries (Figure 3.1). It is important to note, however, that lithium-thionyl-chloride batteries are ten times more expensive than alkaline batteries.

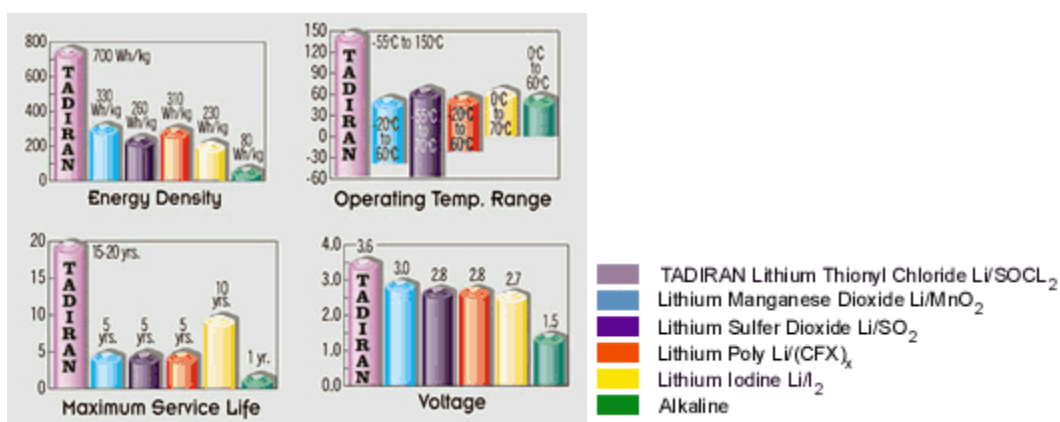


Figure 3.1 Lithium battery chemistry comparison (Tadiran 2002).

Thin film (sputtered) lithium rechargeable batteries have been manufactured in research labs for more than a decade (Bates et al. 2000). Thousands of charge/discharge cycles have been demonstrated, and energy densities near the theoretical limit have been achieved. Thick film (sol-gel, screen-printed, and spin-cast) lithium batteries have been a more recent addition (Doherty et al. 2002). Again, charge/discharge cycles and energy densities are impressive.

### 3.2.2 Fuel Cells

Fuel cells are a very promising long-term solution for autonomous system power generation. The energy densities of fuel cells is dramatically higher than that of batteries, largely because the oxygen needed to release that energy is not counted in the mass balance of the system. Fuel cells are not nearly as compelling for undersea or extraterrestrial power applications where oxygen is not readily available and must be carried along and counted in the mass budget. Demonstrated fuel cell conversion efficiencies (from stored chemical energy in the fuel to useable electrical energy output) are above 80%. Problems with fuel cells include storage and plumbing of the fuel, fouling or poisoning of the chemistry, and elevated temperatures required for operation of most chemistries (including all of the current high performance chemistries).

The two basic classes of fuel cells that appear to be potentially useful for GEMS are hydrocarbon-based and metal-based. Hydrocarbon-based fuel cells derive their electrical energy from the oxidation of hydrogen, whereas metal-based fuel cells derive their energy from the oxidation of either zinc or aluminum. Zinc/air batteries are commercially available today and widely used in hearing aids. Both zinc/air and aluminum/air batteries are advertised for applications from cell phones to electric vehicles and emergency power systems, but it is not clear if these metal/air fuel cell systems are actually in commercial use at this time.

#### 3.2.2.1 Hydrogen/Air

The majority of technical problems with hydrocarbon fuel cell systems today come from the challenges associated with converting common hydrocarbons into hydrogen. This generalized process of fuel reforming is responsible for most of the issues of elevated temperature and chemical poisoning of the fuel cell. In large fuel-cell systems, these issues cause inconvenience, but can be amended by fairly standard chemical engineering techniques, with additional cost and complexity of the resulting power generation system. In an airborne autonomous probe, however, the complexity and weight of fuel-reforming systems may not be acceptable. Direct storage of hydrogen is the most attractive alternative, but requires fundamental breakthroughs before it can be made commercial.

Recent results in hydrogen storage on nanocrystalline materials are quite favorable (Chambers et al. 1998; Chen et al. 1999). Using carbon nanotubes, graphite fibers, and a variety of other (mostly carbon-based) materials, hydrogen storage in the tens of percent by weight has been achieved, with one claim of 20% by weight at atmospheric pressure, and 67.5% by weight at elevated pressures (roughly 100 atmospheres). Chambers et al. (1998) reported room temperature storage of 67.5% hydrogen by weight on graphite nanofibers at a pressure of 114,000 hPa.

#### 3.2.2.2 Zinc/Air

Zinc-air batteries are commercially available in a variety of forms, and provide high energy density (400 Wh kg<sup>-1</sup>; Eveready 2002a) when used in short duration applications. Because the battery will self-discharge over a period of a few months once the initial air seal is broken, zinc-air batteries are not useful for long-term applications (Fig. 3.2).

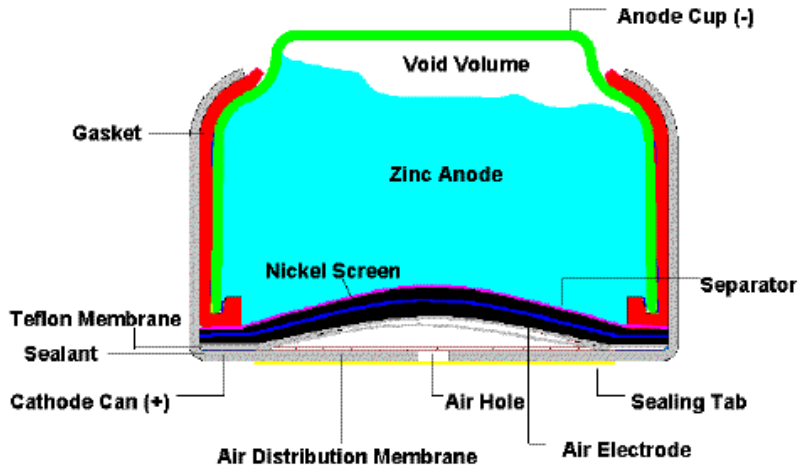


**Figure 3.2** Zinc-air battery cross section from Eveready (2002b). Note in particular the air hole on the bottom surface. Typical dimensions of this type of hearing aid cell are 5 mm diameter and height.

MEMS technology may have a positive impact on zinc-air batteries if a low-cost air valve can be manufactured and integrated into the battery package. By shutting off the air, the self-discharge of the battery can be minimized, and the lifetime of the battery can be determined solely by load-current drain, rather than self-discharge.

### 3.2.2.3 Aluminum/Air

Aluminum-air fuel cells have even higher energy densities, with a theoretical value of  $8100 \text{ Wh kg}^{-1}$  and achieved energy density of  $800 \text{ Wh kg}^{-1}$  using “green” technology (Aluminum Power 2001; Fig. 3.3).

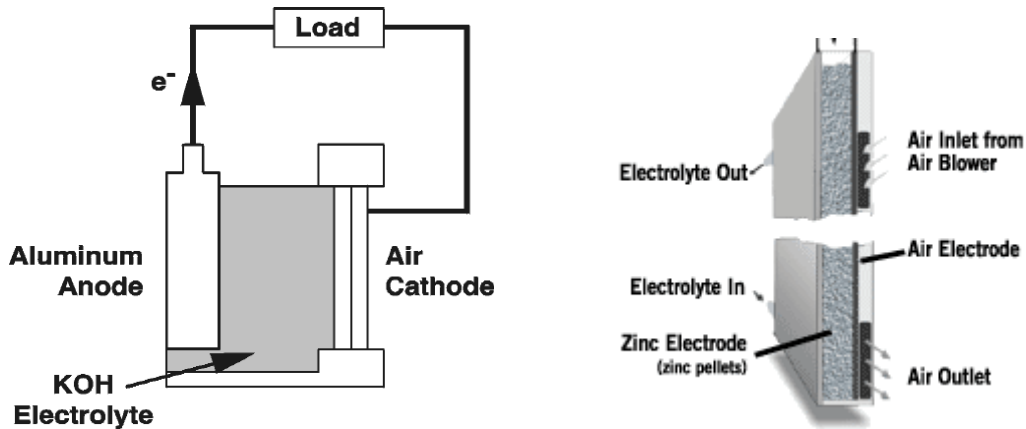


**Figure 3.3** Schematic of an aluminum-air fuel cell and of a zinc-air fuel cell.

### 3.2.3 Solar

Solar illumination in orbit is approximately  $1.3 \text{ kW m}^{-2}$ . Under optimal conditions on the surface of the planet, this drops to approximately  $1 \text{ kW m}^{-2}$ . Light levels from a full moon are roughly six orders of magnitude lower than solar illumination, and starlight is another three orders of magnitude below full moonlight.

Silicon solar cells are simple and inexpensive, and offer conversion efficiencies between 10% and 20% (Zhao et al. 1998). More sophisticated cells achieve roughly twice these efficiencies (Green et al. 2001;

Ohmori et al. 1996). Under clear conditions, this leads to power generation of about  $100 \mu\text{W mm}^{-2}$  or a daily energy generation of more than  $1\text{--}10 \text{ J mm}^{-2}$ .

### 3.2.4 Directed RF

RF power can be beamed to autonomous probes and rectified, as in many commercially available RF-ID systems (Fig. 3.4). This approach is quite effective at short range (e.g. meters), but is more difficult at ranges above one kilometer. To be useful for GEMS, harvestable power levels on the order of at least a microwatt would need to be available. Assuming a 900-MHz antenna, this implies a power density of several tens of  $\mu\text{W m}^{-2}$  at the probe. With a 3-meter aperture interrogating/powering beam, there is a beam divergence of roughly 30 degrees and an effective “powered area” of  $(R/2)^2$ . At a range of 20 km, the required transmitted power is several hundred watts for an effective area of  $10^8 \text{ m}^2$ . This is an achievable power transmission, but only to power probes within 20 km of the transmitter. Tens of thousands of these transmitters would be necessary to cover the continental U.S. Using longer wavelengths leads to longer ranges, but implies that the probes will carry antennas that are more than ten centimeters long. An appropriate band for this type of power supply would also need to be identified.

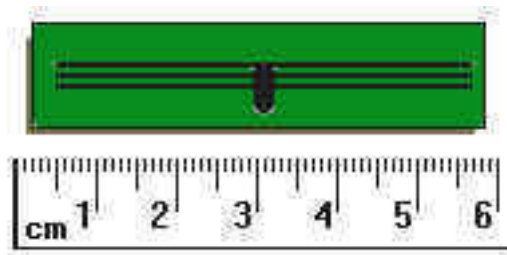


**Figure 3.4** A 2.4-GHz RF-ID tag with a 1024-bit read/write memory and a communication range of a few meters. Fifty tags can be read per second (from RF-ID 2002).

### 3.2.5 Combustion

The Defense Advanced Research Projects Agency (DARPA) Microsystems Technology Office funds a large research program in MicroPower Generation (DARPA 2002a). Most of these projects funded under this program are related to micro fuel cells using hydrocarbon fuels. There are several other approaches to the conversion of hydrocarbons to electricity under this program. These approaches involve combustion and either thermoelectric conversion or mechanical/electromagnetic conversion of the resulting heat energy to electricity. Direct combustion of hydrocarbons has promise for scaling into the centimeter size range, but does not appear to be a reasonable approach for smaller autonomous systems.

## 3.3 Communication

### 3.3.1 RF Communication

RF communication systems consist of a transmitter radiating power and a receiver detecting it. It is difficult to make generalizations about power consumption in communication systems, because there are so many variables that come into play in evaluating performance of these systems. However, the fundamental limits are again related to thermal noise. For a receiver with a noise bandwidth  $B$  (roughly the bit rate), the thermal noise power from the antenna is  $kTB$  (where  $k$  = Boltzmann’s constant and  $T$  = temperature). The quality of the electronics in the receiver determines how close the actual noise performance is to this theoretical limit, and is represented by the noise figure of the receiver  $N_f$ , which is the ratio of the actual noise to the thermal limit. The strength of the radio signal received needs to be greater than the noise by an amount determined by the down-stream signal processing of the signal, and is given by Signal to Noise Ratio  $(\text{SNR})_{\text{min}}$ . This means that overall, the signal power received by the antenna must be greater than  $kTB N_f \text{SNR}_{\text{min}}$ .

For specific calculations, consider the Global System for Mobile (GSM) communications cellular phone standard. The noise bandwidth is roughly 200 kHz for a 115 kbps link. The receiver has about 8 times more

noise than the thermal limit, and the downstream electronics needs a SNR of about 10 to achieve an adequately low bit error rate. In decibels relative to 1 mW (dBm), that gives a sensitivity of -102 dBm or just under one tenth of a picoWatt (pW).

The signal transmitted by the probe must be much greater than the received level because of the inverse square attenuation between the probe and the receiving antenna. With line-of-sight and no nearby objects, the power lost between the transmitter and the receiver is proportional to the square of the distance divided by the wavelength. In addition, reflections off of the ground, buildings, trees, etc., cause the overall attenuation to be proportional to approximately the fourth power of distance (Fig. 3.5).

For a 1-GHz signal, transmitting at a distance of 300 m yields an attenuation of roughly 12 orders of magnitude. Traveling 3 km gives an attenuation of 16 orders of magnitude, reducing a 1-W transmitted signal down to 0.1 pW. The power used by the GSM receiver is roughly 200 mW, and the power used in the transmitter is roughly 4 W. With a data rate of 115 kbps, the energy cost to receive a bit is about 2  $\mu$ J, and 50  $\mu$ J to send a bit. Cordless phones operate with similar data rates at less than one tenth the power, but with a range of only 10–100 m. An average cost on the order of 1  $\mu$ J bit<sup>-1</sup> is common.

The Bluetooth radio (Bluetooth 2002) is designed for short range, 1-Mbps communication in a household or office environment. Transmit power is 1 mW, but the total radio power is still roughly 100 mW regardless of transmit power due to the radio circuit overhead. Despite this limitation, the Bluetooth standard is still the most promising technology for civilian sensor networks such as GEMS with short-range communication cost of roughly 100 nJ bit<sup>-1</sup> in the 2.4-GHz band.

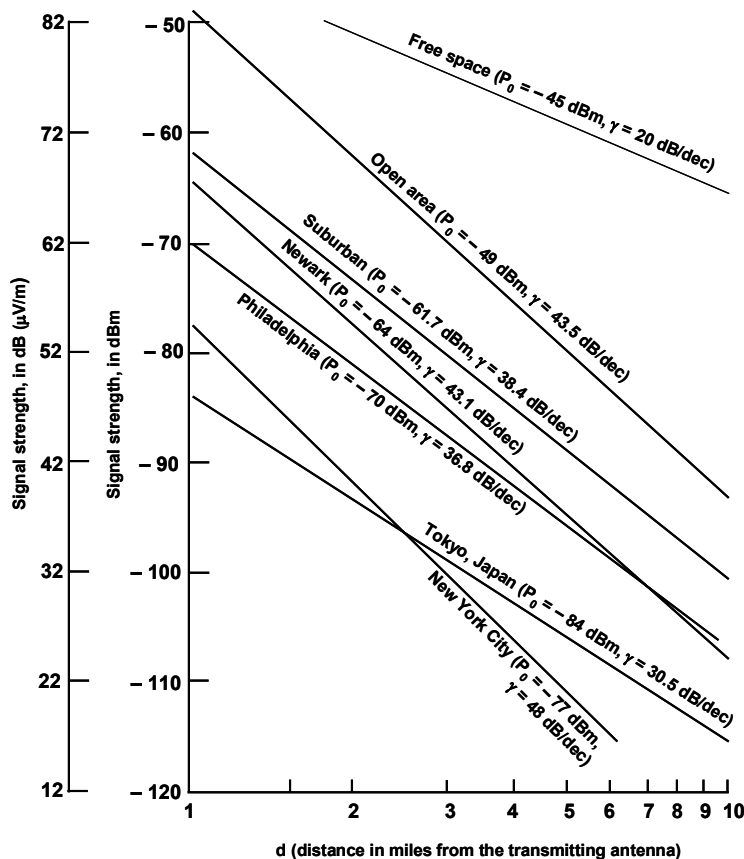


**Figure 3.5** Signal strength versus distance for cellular telephones (from Lee 1995).  $P_0$  is the signal strength (power received, in dB relative to 1 mW) at 1 mile, and gamma is the attenuation exponent, giving power loss in dB per decade of increased frequency. Note that in all surface/land environments, attenuation goes as roughly the fourth power of distance (gamma=40), but for free-space communication it goes as distance squared (gamma=20).

With current Complementary Metal-Oxide Semiconductor (CMOS) technology it is possible to make very low power single-chip radios with reasonable efficiency in the low GHz frequency range. Several research groups around the country are working on a 1 mW CMOS radio with output power on the order of 100  $\mu$ W using traditional super heterodyne designs as well as a variety of novel tricks including ultra-wide-band (Lee 1995).

As CMOS electronics improves, it will be possible to move from the low GHz range (e.g. the 902-928 MHz and 2.45-GHz bands) up to 5–10 GHz or higher. The implications of this frequency shift are that the effective antenna aperture is decreased as the square of the increase in frequency, but the size of the antenna (in both length and cross-sectional area) is decreased as well.

### 3.3.1.1 RF-ID Tags

Originally RF-ID tags were nearly passive devices with almost no on-board energy storage. They consisted of an inductor/antenna, capacitive power storage, and a single CMOS chip with a pre-programmed ID number (Fig. 3.6). These devices were powered by an RF pulse, and they responded using the energy harvested and stored from that pulse with their pre-coded ID.

Modern derivatives of this original concept now contain read/write memory in the kbit range. As the technology has gained acceptance, a new class of RF-ID tag has emerged with on-board power. These new tags have the ability to contain sensors and sample their environment even when they are not in communication with the interrogator.

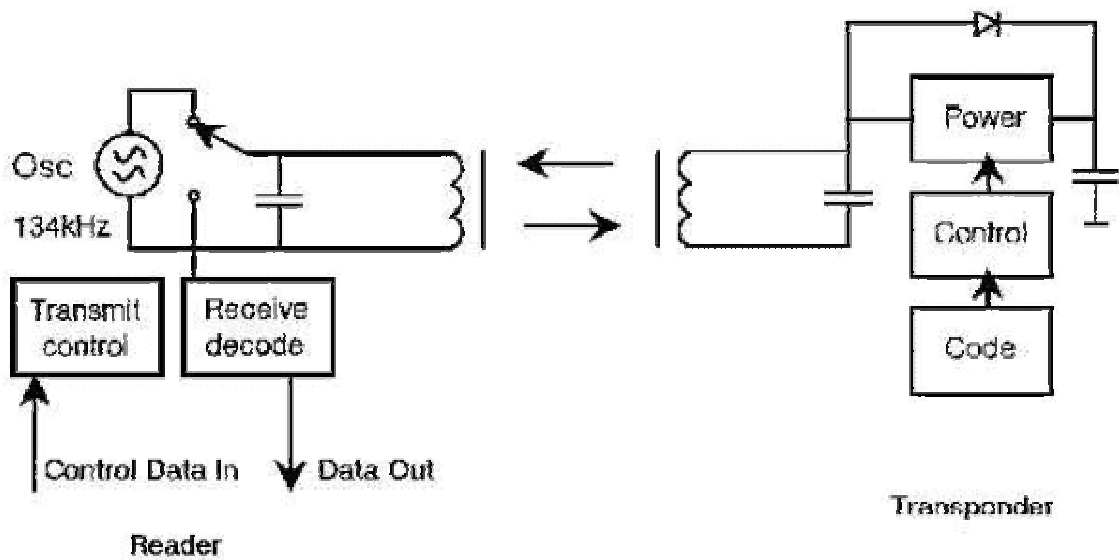


**Figure 3.6** Typical low-frequency RF-ID tag system. Similar designs are available at frequencies up to 2.4 GHz (RF-ID 2002).

The first fully-integrated RF-ID tag was recently announced by Hitachi (2002). This system consists of 1 kbyte on-board memory, on-chip coil antenna, bidirectional communication circuitry at 13.56 MHz, and data rates of 26 kbps. The Hitachi RF-ID tag is the first complete system on a chip (Fig. 3.7). The chip measures 2.3 mm and addition of a MEMS sensor to this chip would be a matter of some research, but not fundamentally difficult. The drawback of the on-chip antenna is that the communication range is currently limited to less than 3 mm. For smart-card and smart-token applications, where the device will be inserted into a slot, this range is perfectly acceptable; however, for the communication ranges required by GEMS, it appears that RF-ID tags will not be a feasible communication technology.



**Figure 3.7** The Hitachi MY1007, an RF-ID system on a chip with no external components.

### 3.3.1.2 Antenna Design

The simplest antennas are quarter-wave monopoles and half-wave dipoles, consisting of a straight piece of wire (or two, for a dipole). At 1 GHz, a wavelength is roughly 30 cm, so a quarter-wave is 7.5 cm. Constraints on the acceptable transmitted power loss due to resistance lead to a minimum cross-sectional area of on the order of ten square microns leading to a total antenna volume of roughly  $0.01 \text{ mm}^3$  when coupled with the length of the antenna.

Other options for small antennas in MEMS probes are fractal antennas (Du et al. 2001) and metamaterials. Fractal antennas are a proven technology which give modest (e.g. 2x) improvement in antenna performance (Fig. 3.8). Metamaterials are a new class of engineered materials with remarkable RF properties. Metamaterials were predicted by the Russian physicist Veselago in 1964, and have recently been demonstrated (DARPA 2002b). It has been shown that periodic arrays of normal materials can create an artificial material with an effective permittivity and permeability that is negative. Such a material has a variety of remarkable properties, including the fact that Snell's law operates in reverse, and waves entering the material are bent away from the normal rather than toward the normal, meaning that a diverging wave will be focused as it transitions between a normal material and a metamaterial. The result is that focused beams can be generated from sub-wavelength antennas.

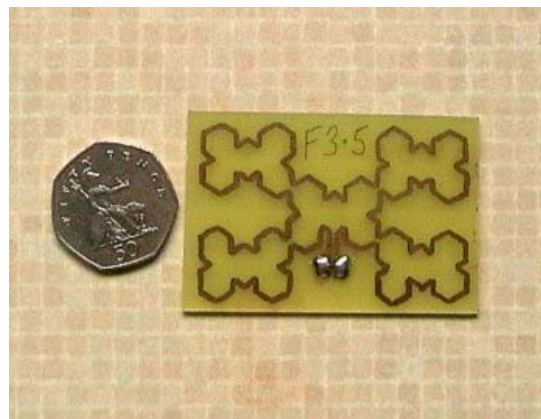


**Figure 3.8** A dual-band 900/1800 MHz fractal antenna.

### 3.3.2 Optical Communication

Communication from airborne probes using optical frequencies can have some advantages over using RF due to the high antenna gains available when the wavelength is small. For instance, a green light emitter (600 terahertz) only needs to be half a millimeter across in order to emit a milliradian-divergence beam. In contrast, a gigahertz radio emitter would need to be a 100 meters in diameter to match the diffraction-limited performance of the optical approach. This six order-of-magnitude difference in wavelength between the two transmitted frequencies translates to a 60-dB antenna gain – more of the transmitted power will find its way to

the receiver (assuming the transmitter and receiver are aligned properly). This high antenna gain is the basis for the interest in optical communication for GEMS.

There are some drawbacks to using optical communication. In addition to the obvious application issues (e.g. clouds and fog will block any optical communication signal and the transmitted signal needs to be aimed), there are some other fundamental limits on the efficacy of optical communication. Radio-frequency receivers will always have higher sensitivity than optical receivers. Since high-performance receivers count individual photons at either radio or optical frequencies, more low-energy RF photons can be sent for a given amount of energy. This fact is not important because the higher antenna gain overpowers the linear increase in energy per photon. Similarly, it takes more energy at shorter wavelengths to generate an electron at the receiver, but this is more than compensated for by the larger number of photons arriving at the receiver.

### 3.3.2.1 Link Budgets

The longest-range laser communication link demonstrated to date is a test performed as the Galileo space probe passed by Earth in 1992. This link consisted of a 0.6 m ground-based telescope, a high-powered laser (20.8 MW peak power), and a Charge Coupled Device (CCD) camera onboard the spacecraft. A 15 bps, a 6,000,000-km long link was demonstrated using this system.

In 1999, personnel at Dr. Pister’s lab performed a similar experiment to start exploring the limits of low-power, long-range laser communication. Using an off-the-shelf laser pointer and CCD camera with a narrowband filter, several long-range laser links were established. The longest link was 21 km from Twin Peaks (near San Francisco) to Dr. Pister’s office at the UC Berkeley campus. The communication bandwidth of 4 bps was limited by the speed of the computer used to decode the data embedded in the video stream.

The experiment at UC Berkeley showed that it is possible to perform long-range terrestrial links using milliradian-divergence beams with only a few milliwatts of optical power. The terrestrial link is technically more challenging than the Earth-to-Galileo link because of factors such as lower optical power at the receiver, more optically dense atmosphere, unfavorable illumination conditions (looking into the sun), and automatic data extraction in a noisy image (Last et al. 2001).

Although not yet possible with today’s technology, it is straightforward to extrapolate to millimeter-size airborne probes utilizing steered optical communication to download data while still in-flight. The proposed optical system would be asymmetric, i.e. probes would not necessarily communicate with one another; instead a large-aperture base station receiver would interrogate probes up to 50 km away. This base station could be located on the ground, in a small UAV, or in a piloted aircraft flying among the deployed sensors. Table 3.2 provides an overview of the optical link budgets.

<b>Table 3.2</b> Optical link budgets.			
	<b>Table Mtn to Galileo Spaceship</b>	<b>Twin Peaks to Cory Hall</b>	<b>Airborne Probe to Ground Station</b>
Transmit power	20.8 MW peak	0.005 W peak	0.001 W peak
Transmit wavelength	532 nm	650 nm	320 nm
Transmitter diameter	0.6 m	0.001 m	0.001 m
Link Range	6,000,000 km	21 km	50 km
Receiver Aperture	25 cm	6 cm	10 cm
Bit Rate	15 bps	4 bps	1,000,000 bps
Beam Divergence	60 microradian	~2 milliradian	0.4 milliradian
<i>Received power (photons/bit)</i>	<i>400,000,000,000</i>	<i>1,300,000,000</i>	<i>40,000</i>

It might also be useful to consider an optical communication system where the airborne probes communicate with one another to form an ad-hoc, peer-to-peer, wireless optical network. Due to the extremely

small receiver apertures (no larger than a square millimeter or so), the range of this type of peer-to-peer link is extremely limited. Link ranges in the tens of meters are possible using the same technologies as in the 50-km link. To extend the link range, either the transmitter or receiver technology will have to improve. On the transmitter end, the new technology could be composed of shorter wavelength lasers, or higher peak power with lower duty cycle. On the receiver end, the new technology could consist of optical bandpass filters with large acceptance angles, amplifiers with built-in thermoelectric cooling to decrease thermal noise in the electronics, ultra short gating to block out background noise, and/or optical homodyne receivers to increase the SNR.

### 3.3.2.2 Transmitter

The main advantage of optical communication is high antenna gain – a very narrow beam of energy will be radiated from the transmitter. This beam needs to be aimed at the receiver. For an airborne probe that will most likely not be stable, this necessitates an active beam steering system. A proposed optical transmitter consists of three parts: a laser source, collimating optics, and a beam steering system. Today’s free-space optical transmitters are benchtop affairs, weighing over 5 kg even for space-based systems where weight is optimized (Wilson and Enoch 2000). The UC Berkeley lab has demonstrated a proof-of-concept transmitter consisting of an edge-emitting laser diode, sapphire ball lens, and 2-axis beam steering MEMS mirror that fits in an 8 mm<sup>3</sup> bounding box and weighs a few tens of micrograms (Last and Pister 2000; Figure 3.9). With the development of high-yield laser arrays, optical transmitters with tens of thousands of laser “pixels” will enable the creation of laser transmitters capable of steering milliradian beams at gigahertz speeds from a cubic millimeter transmitter.

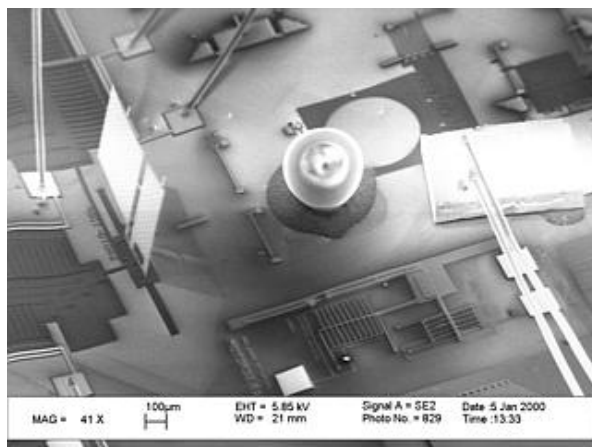


**Figure 3.9** 8mm<sup>3</sup> integrated MEMS laser transmitter. From R to L: 650-nm edge-emitting laser diode, 250 μm diameter sapphire ball lens, 2-axis surface micromachined beam steering mirror.

### 3.3.2.3 Laser Source

The current Vertical Cavity Surface Emitting Lasers (VCSELs) provide up to 100 mW output power (in rare cases) with slope efficiencies above 50% and wall plug efficiencies exceeding 20% (DARPA 1998). Able to be modulated at up to several gigahertz, these lasers are compact, efficient sources for an optical transmitter. The major drawback to using VCSELs instead of edge-emitting lasers is the comparatively wide spectral linewidth. This wide bandwidth limits how narrow a bandpass filter can be used at the receive-end of the optical link. The background light that makes it past this bandpass filter forms the dominant optical noise source in most free-space optical communication systems. Linewidths today are significantly below 1 nm (Coldren et al. 1998). The most room for improvement in VCSEL performance is in output power and process uniformity – current VCSELs typically output mW (though higher-power diode-pumped VCSELs exist) and no two VCSELs on any given wafer are exactly alike (Lei et al. 1999).

### 3.3.2.4 Beam steering

As shown in Figure 3.10, current fine-angle beam steering is accomplished using macro-scale mirrors driven by magnetic [voice-coil (Ball Aerospace 2002) or galvanometer (Cambridge Technologies 2002)] or piezoelectric actuators (PhysikInstrumente 2002). These actuators have bandwidth in the few kilohertz range, microradian pointing precision, and beam steering angles up to a couple of tens of degrees. Power consumption is in the Watt range and above, with control electronics consuming most of the power. In contrast, MEMS mirrors have comparable bandwidths and beam steering angles (Conant et al. 2000), but operate using tens of mW – again, with control electronics responsible for most of the power consumption.



**Figure 3.10** Current beam steering devices (from left to right): voice-coil 2-axis mirror, 1- and 2- axis galvanometric scanners, and 1- and 2- axis piezoelectric fast-steering mirrors.

Fundamentally, the power consumption required to move an electrostatically-actuated micromirror is proportional to the capacitance of the actuator array, the frequency of operation, and the square of the drive voltage. The mirrors developed at UC Berkeley (Milanovic et al. 2001) have a capacitance of around 1 picoFarad (pF), drive voltage of  $\sim 100$  V, and resonant frequency of  $\sim 5$  kHz. Only  $25 \mu\text{W}$  are actually required to drive this mirror – in the next few years the drive electronics will impose less overhead. Using an electrostatically-actuated MEMS mirror, a collimating lens, a VCSEL source, and a BiCMOS driver chip, an entire transmitter can be integrated into just a few cubic millimeters. Stabilization of the beam steering system can be performed with gyros. MEMS gyros can be fabricated in the same process that generated the mirror (Fig. 3.11). Combined with a CMOS hall-effect sensor, gyro-stabilization of the laser against thousands of degrees per second of rotation (such as tumbling airborne probes) is possible (IMI 2002). The gyros would also be part of the navigation system, described in Section 3.6.2.

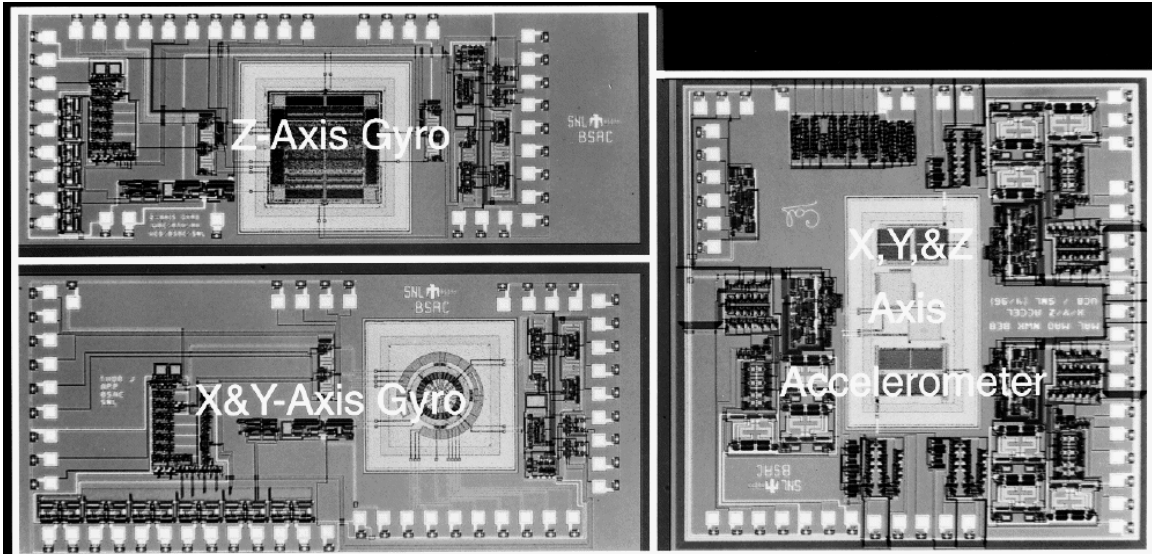


**Figure 3.11** Three-axis MEMS gyroscope illustrating how all inertial sensors and control electronics are integrated on a single die (IMI 2002).

Eventually, the desire for higher levels of integration, faster beam steering, more flexible beamshaping, and lower-power operation will push the design towards a solid-state solution. A 1-mm cube consisting of a collimating lens on one side and a VCSEL array on the opposite side will provide 40,000 electrically-switchable, non-overlapping, milliradian-divergence beams. Beam shaping can be provided by turning on more than one laser at a time. Although not capable of steering over as wide a range as the mirror-based system (200 spots versus 1000 for a mirror capable of scanning  $\pm 0.5$  radian), this system has the advantage in size, power, and speed (Fig. 3.12).

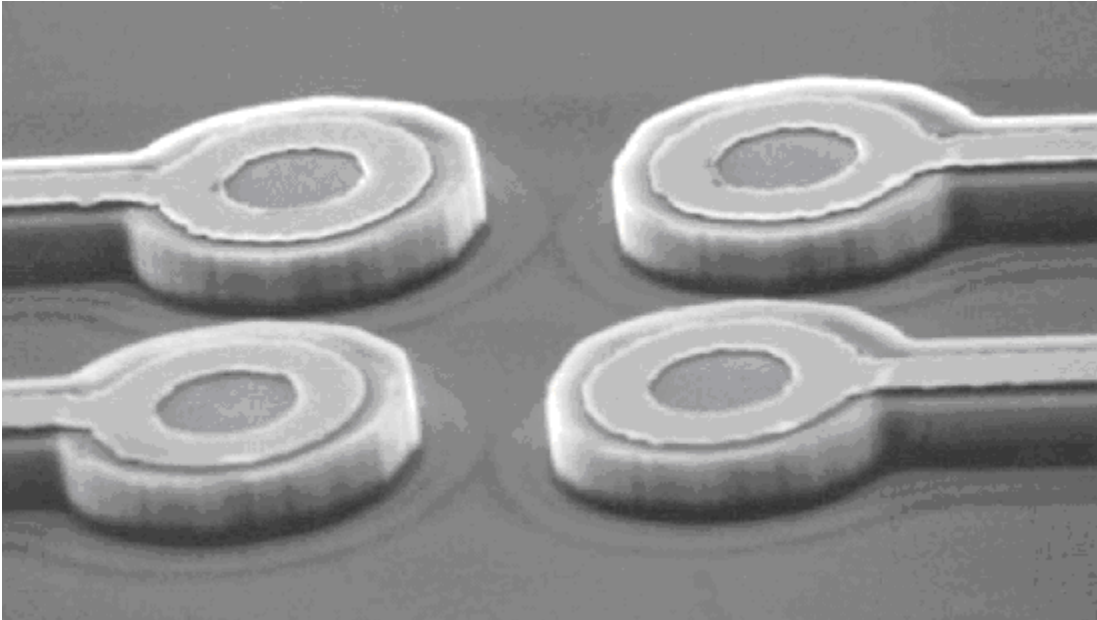


**Figure 3.12.** VCSEL array. Circular regions are active regions of lasers (Lei et al. 1999).

Fundamentally, the transmitter is limited by the energy required to sense its attitude in space, move its beam steering subsystem and hold it in place during the transmission window, and fire off the data payload over the laser. For a kilobit payload transmitted at 1 Mbps from an airborne probe flipping over 5 times per second, this would require the transmitter to maintain a link for 1 ms, during which time the node will have spun only 1.8 degrees. This will require roughly 0.3  $\mu\text{J}$  to drive the gyroscopes (0.1  $\mu\text{J}$  per axis: driving a 1 pF capacitive load with 100 Vp-p at 20 kHz for 1 ms), 0.2  $\mu\text{J}$  to rotate the mirror into position and keep it there during the transmission window (0.1  $\mu\text{J}$  per axis, same capacitance/drive as before), and 12.5  $\mu\text{J}$  to fire off one thousand bits from the laser (5 mW peak optical power, 50% duty cycle, at 20% wall-plug efficiency). Altogether this requires 12.8  $\mu\text{J}$  for a packet burst, with the vast majority consumed by the laser. An autonomous airborne sensor probe would have over 75 such bursts available from a 1 Joule battery.

Unfortunately, this analysis so far neglects the need for the transmitter to find the receiver in the first place. The overhead required for acquisition is one of the larger drawbacks to the optical communication approach. If there is no prior knowledge of the location of the receiver, the transmitter must send up to 10-50 bits to scan every possible direction the beam steering system can aim – an expenditure of up to 0.125 Joule. The resulting drain on the battery might not be acceptable for many sensing applications.

There are several ways to reduce the magnitude of this problem. One is to perform a more intelligent search – for instance, by performing a binary search through range space. This involves transmitting with a wide beam to find receivers close to the transmitter and narrowing down the beam to find receivers further away. If this approach is used instead of an exhaustive, one-point-at-a-time search, the energy required to perform a full acquisition can be reduced by a factor of up to 50,000 (for a binary search through a 1000 x 1000 point field-of-view). Not only does this approach save time and power during the acquisition phase, but also once the link is established. If the receiver is close to the transmitter, the transmitter can turn down the laser power to save energy. Another approach to intelligent acquisition is for the sensor node to know in advance where to aim its laser. This information, in conjunction with its current orientation, is enough to reduce the scope of the search that the transmitter must perform.

### 3.4 Networking

A critical challenge for GEMS is to define viable communication and networking solutions given available power and probe separation. The probe separation distance as well as power constraints and communication range will determine if each probe can transmit to a remote receiving station (aircraft, LEO satellite, etc.) or if mobile networking via multihop routing (Delin and Jackson 2000; Kahn et al. 2000) is viable. To study the network design issues in detail as part of the Phase II effort, it will be necessary to consider fault tolerance, scalability, production costs, operating environment, network topology, hardware constraints, transmission media, and power consumption as identified by Akyildiz et al. (2002) in a recent review of wireless sensor networks. For example, RF communication would likely follow the Industrial, Scientific, and Medical (ISM) standards to ensure license-free bands worldwide. The size, shape and power constraints of the probes will necessitate trade-offs in antenna design (as highlighted above) thereby limiting the choice of ISM carrier bands to the ultrahigh frequencies  $> 1$  GHz.

### 3.5 Sensors

Three parameters are seen to be core to any atmospheric in situ system: temperature, relative humidity (RH), and pressure (NWS 2002). The velocity can be extracted from the positional data of the probes and will not be discussed here (see section on navigation). Microfabricated devices for sensing these core parameters are well developed (Sze 1994; Kovacs 1998). In most cases, it is relatively straightforward to show how existing technologies can be modified and used in integrated, low-power applications. The brief overview below presents a handful of technologies that fit the following criteria:

- Microfabricated technology is based on standard, low-cost Integrated Circuit (IC) fabrication,
- Integration of various sensor types on a single platform is straightforward,
- Technology lends itself or can be modified for low-power operation,
- Lifetimes measured in months to years,
- Operational temperature range of  $-100^{\circ}\text{C}$  to  $100^{\circ}\text{C}$ ; pressure range of 1013.5 hPa to  $\sim 1$  hPa; humidity range of 0 to 100% RH.

#### 3.5.1 Current Technology

As a comparison, Figure 3.13 shows a modern radiosonde (RS90). The radiosonde can operate for 135 minutes on a 19-V battery. The sensor suite is assembled into a projecting boom which extends ahead of the radiosonde path, thereby sensing undisturbed air. The temperature sensor is based on a hermetically sealed ceramic dielectric; it is designed for  $-60^{\circ}\text{C}$  to  $90^{\circ}\text{C}$  operation with a resolution of  $0.1^{\circ}\text{C}$  and a response time of 0.5 s. The humidity sensor is based on water absorbent dielectric polymer film and it measures 0–100% RH with a resolution of 1% RH and a 1 s lag. Finally, the pressure sensor is a silicon pressure transducer with a 3–1080 hPa range, and a resolution of 0.10 hPa. Most of the radiosonde weight comes from the transmitter and battery units (Fig. 3.14).

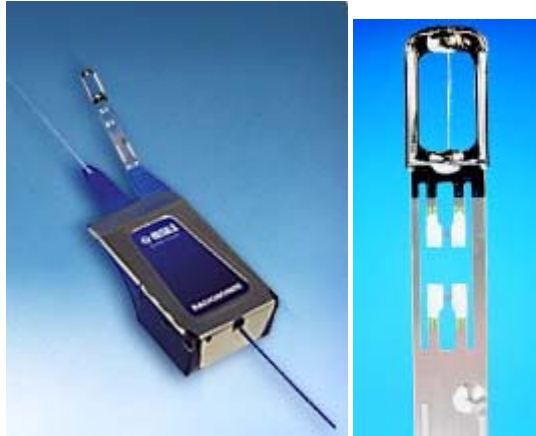


**Figure 3.13** RS90 radiosonde and sensor boom close-up (Vaisala 2002). The radiosonde body measures 15 cm x 9 cm x 5 cm and weighs ~0.3 kg. The sensor head itself measures approximately 2 cm x 8 cm.

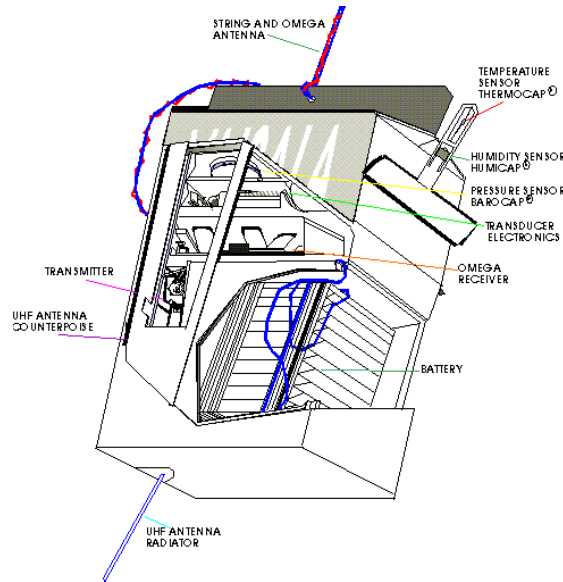


**Figure 3.14** Inner detail of an RS80 radiosonde (from NSIDC 2002). Note the bulk of the unit is comprised of the battery and transmission units.

### 3.5.2 Temperature

There are a wide variety of techniques applicable to microfabricated temperature sensors. In particular, thermistors and Proportional-To-Absolute-Temperature (PTAT) sensors are well suited for low-power applications. A thermistor is simply a resistor whose resistance varies as a function of temperature in a known, and hopefully linear fashion. The typical thermal coefficients of resistance for polysilicon are  $\sim 10^{-3} \text{ }^\circ\text{C}^{-1}$ . Operation would merely entail applying a known voltage and measuring the resultant current. Additionally, a separate reference resistor and/or a digital logic look-up table would provide the needed calibration information.

As an example, a 1 M $\Omega$  polysilicon thermistor queried for 10  $\mu\text{s}$  [as for a 100 kSamples  $\text{s}^{-1}$  (kS  $\text{s}^{-1}$ ) Analog to Digital Conversion (ADC)] at 1 V would require 10 pJ energy per reading. The noise voltage associated with such a device would be  $<100 \text{ nV } (\sqrt{\text{Hz}})^{-1}$ . Assuming digital logic densities increase along projected roadmaps, the required digital look-up table would have a resolution well below 0.01 $^\circ\text{C}$  with each look-up consuming  $<1 \text{ fJ}$  per look-up. The major drawback for a thermistor system comes from the initial calibration of each device. Each device would need to be queried at start-up (at some known temperature) to determine the

Direct Current (DC) offset associated with fabrication mismatches; which serves to adjust the look-up table information, derived initially from known material data.

A second approach to temperature sensing is the PTAT sensor (Kovacs 1998). At its simplest, this device is a four-transistor current source whose bias currents vary as a linear function of the absolute temperature. As with the thermistor, the PTAT needs a digital look-up table to account for DC offsets associated with transistor mismatch. With advances in low-power analog circuit technology, a 1V PTAT drawing  $\sim 100$  nA will be fabricated in the next few years. Queried for 10  $\mu$ s, this device would require  $\sim 1$  pJ of energy per measurement.

Since both of these methods require relatively simple IC processing, they can be fully integrated with other microfabricated components. This is an important requirement as temperature compensation of other sensor types is absolutely required at the defined temperature ranges. Importantly, both of these technologies can be implemented directly below the sensors, allowing for little to no temperature differences between the compensator and sensor.

### 3.5.3 Humidity

Modern dielectric polymer humidity sensors are readily scalable into the sub-mm<sup>2</sup> range. These humidity sensors employ a water absorbent polymer coated onto interdigitated or parallel-plate electrodes (Fig. 3.15). The amount of water present in the polymer correlates with the RH in the surrounding ambient producing a change in the dielectric constant of the polymer capacitor (Boltshauser et al. 1993; Qui et al. 2001).



**Figure 3.15** An interdigitated electrode.

The ease of integration of this technology with conventional CMOS IC processing has resulted in a recent interest in miniaturization of polymer humidity sensors. A recent comparison of several design variations is illustrative of current microfabricated humidity sensor performance (Laville and Pellet 2002). A typical interdigitated structure has ten 25  $\mu$ m-wide electrodes with a total sensor area of 1 mm<sup>2</sup>. The polymer coating is 650 nm thick polyimide. The total capacitance (C) of the sensor is 8 pF at 0% RH with a relative sensitivity of 27%. The sensors operate easily between -50 to 200° C with current lifetimes measured in months.

A reduction in sensor area of at least two orders of magnitude is possible even with existing state-of-the-art fabrication technologies and would yield a sensor with 100 femtoFarrad (fF) at zero relative humidity. If the noise voltage for this capacitor and amplification stage is assumed to be on the order of several  $\sqrt{KT/C}$  volts/ $\sqrt{\text{Hz}}$  (where C is the value of the capacitor, K is the Boltzmann constant and T is temperature), that would yield a  $\sim 200$   $\mu$ V noise level. This falls well within the currently achievable sampling Least Significant Bit of  $\sim 4$  mV for a low-power 8-bit ADC. Operating at 1 V with 100 kS s<sup>-1</sup>, sampling the resistor would require 50 fJ per measurement.

Temperature compensation of these devices would be readily achievable with integrated temperature sensors (described above). Advances in polymer technologies are likewise yielding materials with larger temperature ranges, larger sensitivity to moisture and longer lifetimes (Matsuguchi et al. 1998). Therefore, dielectric polymer sensors are readily amenable to ultra-miniaturized, low power applications such as GEMS with near-term technology.

### 3.5.4 Pressure

Pressure sensors were one of the earliest successes of micromachining technology (Kovacs 1998). A wide variety of designs exist for measuring pressure; most make use of micromachined silicon diaphragms whose deflection is measured in a variety of ways (Kovacs 1998). In conjunction with piezoresistive sensing, micromachined diaphragms have the advantage of very low-power operation (sensing is done by running current through a resistor, as with the thermistor above); however, they do not scale well below diaphragms of less than a few 100  $\mu$ m on a side (Rossing and Fletcher 1995). This is alleviated in part by scaling down the

thin-film thickness of the diaphragm but at polysilicon or metal thicknesses  $< 100$  nm, gas diffusion through the diaphragm limits pressure ranges and useful lifetimes (Gosele 1998).

A favorable, emerging technology for pressure sensing in GEMS is the use of damped microfabricated resonators (Gtierrez et al. 2001). In these resonators, the friction caused by air molecules brushing against a resonant structure dampens the amplitude of motion. This dampening can be readily measured since the quality factor ( $Q$ ) of the resonator is inversely proportional to the rate of dampening. The rate of dampening is proportional to the surrounding air pressure. A first generation device had a dynamic range of  $10^{-6}$  to 0.01 hPa, and an upper range of 10,000 hPa was thought readily achievable with minor modifications. Figure 3.16 shows the sensor response versus pressure.

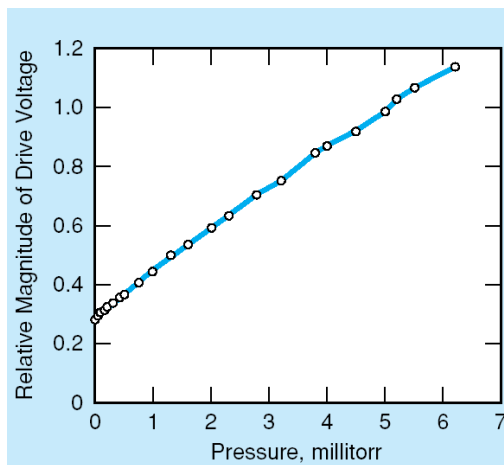


**Figure 3.16** Drive voltage vs. pressure from Gtierrez et al. (2001).

This scheme scales well into the sub-micron regime. The system is inherently low-loss, with a  $Q$  reported near  $10^5$ . In particular, since the operating power is proportional to resonator mass, scaling down should yield very low power devices. Constraints include designing resonant frequencies well below the ADC sampling rate, isolation from external gas flows and possible temperature non-linearities at extremely cold temperatures.

The scaling down of microfabricated resonant structures is the subject of intense research, but several rough statements can be made regarding the scale down of such a pressure sensor over the next decade. Current microfabricated thin-film resonators typically operate at frequencies of  $\sim 100$  kHz and have areas  $\sim 0.01$  mm<sup>2</sup>. Maintaining film thicknesses while scaling areas down maintains the ratio of surface damping effects to inertial effects. With the advent of radio-frequency, nanoscale resonator technologies,  $100 \mu\text{m}^2$  area resonators operating at gigahertz frequencies with motional resistances  $\sim 100 \Omega$  are foreseeable in the near future (Martin et al. 1996; Nguyen 1999; Nguyen 2001). Assuming a sensor capacitance of  $\sim 1$  fF, an operational frequency of 1 GHz, and an operating voltage of 1 mV, the power required to operate such a device is  $\sim 1$  pW. Neglecting parasitic capacitances and losses in the drive and sense circuitry, the argument is compelling even if this simple approximation is an order of magnitude too low. Resonators of this scale would likely be largely insensitive to external vibration and perturbation.

### 3.5.5 Gas Sensors

Microfabricated chemical sensors have matured rapidly over the last decade, with a vast and growing library of target compounds (Madou and Morrison 1989; Kovacs 1998). Already employed in many areas, microfabricated chemical sensors lend themselves readily to the same type of integration discussed for the core sensor technologies. One method in particular, resonant beam sensing, looks very promising for sub-micron, low-power miniaturization for a wide range of chemistries. Discussion of general principles can be found in Baltes et al. (1997) and Martin et al. (1996).

This method employs a micromechanical cantilever whose end is coated with an appropriate chemically sensitive film (Fig. 3.17). As the gas reacts with the sensitive film, the mechanical characteristics of the cantilever beam changes. This change can be easily measured most commonly by looking for a frequency shift

in the fundamental resonant frequency of the system. Current cantilevers measure  $300\ \mu\text{m} \times 100\ \mu\text{m} \times 2\ \mu\text{m}$ , resonate at  $\sim 30\ \text{kHz}$  with a tip amplitude of  $22\ \text{nm}\ (\text{mW})^{-1}$ , and a  $Q$  of  $\sim 300$ . Current sensed compounds include alkanes, aromatic and hydrogenated hydrocarbon vapors (Hierlemann et al. 2000).

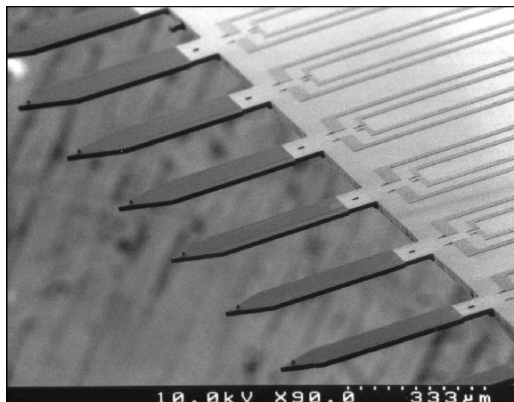


**Figure 3.17** Piezoresistive cantilever array from Nascatec (2002).

Bending mode cantilevers will be designed into the nanometer range in the next few years. Since the compound sensed is dependent entirely on the reactive film at the cantilever tip, arrays of tens of nanometer-scale cantilevers each with a different sensing chemistry are feasible within the next ten years. Power consumption and energy requirement analysis follows exactly as for the pressure sensor resonators above. External noise and vibration become much less relevant at nanometer scales.

### 3.6 Navigation

Since atmospheric wind velocity will be measured based on changes in probe position, it is necessary to assess whether miniaturization of accelerometer, gyroscope, and GPS technology (Allen et al. 1998) will provide viable opportunities for navigation. It appears that a long-term solution using a GPS-aided Inertial Navigation System (INS) would be a viable option for GEMS. In addition, network localization is another option as discussed below.

#### 3.6.1 Existing GPS

The GPS consists of a constellation of earth-orbiting satellites that transmit pseudo-random bit sequences with extreme time precision, providing position and time information to receivers within range. GPS receivers must decode the incoming Code Division Multiple Access signals from at least four satellites in order to estimate their position in three dimensions, along with the current time. With an additional local transmitter, GPS receivers can achieve an accuracy less than 1 cm. Without the local transmitter, the accuracy is on the order of 10 meters and 1 nanosecond.

The GPS signal is at approximately 1.6 GHz, and the raw analog signal is approximately ten times weaker than the background noise at the same frequency band. Only with substantial coding gain can the -10dB SNR signal (on the order of femtoWatts) be converted into a valid digital data stream. This coding gain comes at the expense of decoding time. From a “cold start”, GPS receivers can take up to several minutes of full-power operation before they can lock on to the satellite signals and determine their position. Once the rough position is known, a “warm start” lock-in takes substantially less time, but still on the order of 10s of seconds.

Building an RF front end that can provide sufficiently low noise under these conditions is very challenging. The fundamental tradeoff in well-designed RF front ends is between noise, bandwidth, and power. The fundamental limits to the current consumption of the front-end RF amplifiers are between 10 and 100 milliamps.

In addition to the analog front end, there is substantial power consumed in modern GPS receivers in the digital decoding of the signals. The latest GPS chipsets consume between 1 and 200 milliamps from a 3 V supply, which is the sum of the analog and digital components.

Advances in circuit technology (e.g. finer linewidth CMOS, and even nanotech-based electronics which at this point is only theoretical) will have a substantial positive impact on the power consumption of the digital circuits in the GPS receiver, but will have very little impact at all on the analog front end. The current consumption in the analog front end is fixed by the noise requirements. Improved process control and linewidth will perhaps allow the supply voltage for the analog front end to be decreased, but not by more than a factor of two or three. This sets a fundamental lower limit on the power consumption of the analog front end of GPS receivers at something between 10 and 100 mW. This lower limit on power consumption, combined with the basic requirement for a 10 second “warm start” on position acquisition, means that the energy cost for a probe to acquire position via the existing GPS is on the order of 0.1 to 1 J.

### **3.6.2 Inertial Navigation**

All of the components of a GPS-aided INS can be fabricated with MEMS and integrated circuit technology as part of the probe. A complete navigation system includes 3 accelerometers, 3 gyros, and GPS or other location determination. Navigation and filtering software combines data from all sensors to provide optimum determination of position and attitude. MEMS accelerometers are commercially available and MEMS gyros, as described in Section 3.3.2.4, are coming into production.

Many types of MEMS accelerometers are available commercially. As an example, the Analog Devices Inc. ADXL105 is a single Axis,  $\pm 5g$ , low noise, wide bandwidth, analog output accelerometer. It has 2 mg resolution, 10 kHz bandwidth, and an on-board temperature sensor. Two MEMS gyros are available from Analog Devices (Analog 2002). The ADXRS300 provides a dynamic range of  $300^\circ \text{ s}^{-1}$ , and the ADXRS150 provides a dynamic range of  $150^\circ \text{ s}^{-1}$ .

### **3.6.3 Future GPS**

Looking forward several decades, a substantial improvement in the energy cost to acquire position can be envisioned if a future generation of GPS satellites is launched which broadcasts a stronger signal. Increasing the broadcast power of the GPS satellites has a nonlinear effect on the energy required for a probe to perform a location measurement. A one hundred fold increase in the signal received from the satellites would lead directly to a one hundred fold decrease in the power consumption of the RF front end analog circuitry. In addition, the ability to have a positive SNR would dramatically decrease the time required for the digital circuitry to achieve a lock on the incoming signal. While the digital circuit power is assumed to be a small fraction of the analog power in GPS receivers using future technologies, the decrease in the acquisition time would reduce the time that the power-hungry front ends need to operate. Hence, a one-hundred-fold increase in received signal strength would result in at least a thousand fold decrease in the energy required for a cold- or warm-start position measurement.

This level of increase in signal strength received from the satellite network is easily achieved by some combination of increasing transmit power and decreasing range. Currently there are 24 satellites orbiting at 12,000 miles, and transmitting 50 W. Modern telecommunications satellites transmit with over 1 kW of power, more than twenty times the power of the current GPS signal. With line-of-site signal strength varying as the square of the distance between transmitter and receiver, the signals from a larger constellation of low-earth-orbit satellites at 1000 miles would be roughly one hundred times stronger even with constant broadcast power. Hence, given an improved GPS satellite constellation in the future, and improved circuit processes for the GPS receivers, position measurements could be made at an energy cost of only tens of  $\mu\text{J}$ .

### **3.6.4 Localization**

Although future GPS may be suitable for GEMS in the long term, another option for navigation is network localization. With this solution, only several probes (or remote nodes such as UAVs) have knowledge of their locations and the remaining probes estimate their position dynamically using an on-board algorithm (Savvides et al. 2001). Further study of this issue in a Phase II effort will be necessary especially for scalability to determine if localization can be accomplished given power requirements and on board processing power as the network size increases from hundreds to potentially millions of probes.

## 4 System Modeling

The probe design characteristics, networking, and communication as described in Section 3 will affect the quantity and latency of data available for assimilation into NWP models as well as the subsequent forecasts initialized using such data. The large number of possible trade-offs based on design characteristics such as sensor accuracy and sampling frequency, DA methodologies, weather scenarios, and other factors constitute a multi-dimensional parameter space. System modeling is used as a cost-effective and controlled way to explore these trade-offs.

### 4.1 Numerical Weather Prediction Model

The nature of atmospheric flow patterns is sufficiently variable that probes could remain near their release point or be rapidly swept away by the wind, depending on the weather regime. NWP models are capable of resolving this variability and are therefore ideal tools to simulate probe dispersion and deployment. In addition, simulated measurements of atmospheric temperature, pressure, humidity, and wind velocity can be used to evaluate the impact of these observations on meteorological analyses and forecasts for different weather regimes. Measurements from the probe network must be of sufficient accuracy and spatial coverage to improve the diagnosis and forecasting of weather patterns, above and beyond the skill obtainable with conventional weather observations. Simulation experiments can also provide guidance for probe requirements relating to sampling frequency, data storage and processing, networking and navigation algorithms, and communications capability.

The NWP model of choice is the Advanced Regional Prediction System (ARPS; Xue et al. 2000; Xue et al. 2001). The ARPS is a complete, fully automated, stand-alone system designed to forecast storm- and regional-scale weather phenomena. The ARPS includes a data ingest, quality control, and objective analysis package known as ADAS (ARPS Data Analysis System; Brewster 1996), a prediction model, and a post-processing package. Table 4.1 provides a brief summary of the major dynamical and physical features of the ARPS used for the impact-analysis simulations presented in Section 4.5.

Table 4.2 summarizes the resolution and coverage of the terrain and surface characteristics data sets used in the simulations. All terrain data sets used in the ARPS are based on Digital Elevation Model data available from the U.S. Geological Survey sites, which are also used by the National Imagery and Mapping Agency. The ARPS pre-processors perform additional adjustments to the elevation data for oceans and lakes, and to ensure that terrain, soil and vegetation data are consistent. Global sea-surface temperatures were interpolated from the Navy Operational Global Atmospheric Prediction System (NOGAPS) model initial conditions, whereas soil moisture was initialized using fixed values based on climatological soil types.

The ADAS generates initial conditions for the ARPS model by combining weather observations with a background grid, typically provided by a larger-scale atmospheric model. ADAS utilizes the Bratseth objective analysis procedure (Bratseth 1986) consisting of an iterative successive corrections method (SCM) that converges to the statistical or optimum interpolation (OI). The Bratseth scheme is superior to traditional SCM methods because it accounts for variations in data density and observational errors, similar to OI. This capability is critical to determine how the accuracy and distribution of simulated MEMS-based observations affect meteorological analyses and forecasts.

<b>Feature</b>	<b>Description</b>
Equations	Nonhydrostatic and fully compressible
Coordinate system	Generalized terrain-following height coordinate (sigma-z) with stretching
Geometry	Full 3-D configuration
Prognostic variables	u, v, and w wind components, Potential temperature and pressure, Subgrid-scale turbulent kinetic energy (TKE), Mixing ratios for water vapor, cloud and rainwater, and ice species
Initial Condition	Operational forecast models ADAS
Lateral boundary conditions	Operational forecast models ARPS
Top / bottom boundary conditions	Radiation condition and rigid boundary with Rayleigh sponge layer
Nesting	1-way interactive mode
Subgrid scale turbulence	1.5-order closure TKE-based scheme, fully 3-D in sigma-z
PBL turbulence parameterization	1.5-order TKE based non-local mixing
Cloud microphysics	Lin/Tao five-category ice microphysics
Cumulus parameterization	Kain / Fritsch
Soil model	Two-layer soil-vegetation model with surface energy budget
Radiation	Full shortwave / longwave schemes with cloud-radiation interaction

<b>Data Set</b>	<b>Resolution</b>	<b>Coverage</b>
Terrain	1 degree 5 minute 30 second	Global Global North America
Soil Type	1 degree 1 km	Global Continental U.S.
Vegetation Type	10 minute 1 km	Global Global
NDVI <sup>1</sup>	10 minute 1 km	Global Global

<sup>1</sup>Normalized Difference Vegetation Index

#### 4.2 Probe Dispersion

The ARPS is coupled with a Lagrangian particle model (LPM) to simulate the dispersion of and observations collected by an ensemble of probes. The LPM is developed specifically to run within the framework of the ARPS and is based on the Hybrid Particle And Concentration Transport model (Walko et al. 2001).

The LPM tracks the location of each probe based on three-dimensional (3-D) wind components and updates probe position (x, y, z) from the following:

$$x(t + \Delta t) = x(t) + [ u(t) + u'(t) ] \Delta t \quad (4.1)$$

$$y(t + \Delta t) = y(t) + [ v(t) + v'(t) ] \Delta t \quad (4.2)$$

$$z(t + \Delta t) = z(t) + [ w(t) + w'(t) + w_d ] \Delta t \quad (4.3)$$

where  $\Delta t$  is the model time step,  $u$ ,  $v$ , and  $w$  are the resolvable-scale west-east, north-south, and vertical components of wind velocity, respectively, obtained directly from the ARPS model, and  $u'$ ,  $v'$ , and  $w'$  are the turbulent velocity fluctuations estimated from a Sub-Grid Scale (SGS) turbulence parameterization (Mellor and Yamada 1982) similar to the SGS scheme of Deardorff (1980) used in the ARPS model. The turbulent velocity components are derived from a first-order Markov scheme assuming that turbulence is Gaussian and nonhomogeneous in the vertical but locally homogeneous in the horizontal. In addition, the probes are assumed to be passive tracers moving independent of one another and transported by the wind. The current version of the LPM for ARPS does not include corrections for inertia and cross trajectory effects to account for the dynamic response of heavier probes to turbulent flow different from fluid elements (i.e. passive tracers).

The  $w_d$  term in equation (4.3) is the vertical slip velocity that is modeled as a function of probe diameter and density, dynamic air viscosity, air density, and acceleration due to gravity (Bacon and Sarma 1991). For all simulations discussed in this report, probes are negatively buoyant with  $w_d$  held constant at  $-0.08 \text{ m s}^{-1}$  based on an assumed probe diameter of  $40 \text{ }\mu\text{m}$  and air density of  $0.16 \text{ kg m}^{-3}$ , typical for the upper troposphere and lower stratosphere. With appropriate buoyancy control or aerodynamic design, probes with larger diameters could have equal or smaller negative slip velocities and remain airborne longer given identical patterns of vertical air motion.

At this time, the LPM does not include a parameterization for wet deposition or precipitation scavenging to simulate the processes by which material is removed from the atmosphere (Seinfeld and Pandis 1998). As wind currents transport probes through areas of precipitation, liquid or frozen hydrometeors impacting the probes could alter their trajectories and/or cause them to washout of the air. The probability that a probe will be scavenged by hydrometeors can be modeled as a function of probe size, precipitation rate, hydrometeor size, and collision efficiency following Aylor and Sutton (1992). Although beyond the scope of the Phase I project, precipitation scavenging may significantly affect probe lifetime (i.e. how long probes remain airborne). Therefore, it will be important to include scavenging in the LPM as part of the Phase II effort to study the relationship between dispersion, scavenging, data impact, communication, and networking issues within the overall SDT cycle.

### 4.3 Deployment Strategy

A large number ( $> 10^6$ ) of simulated probes can be deployed any time during the model integration at any latitude, longitude, and altitude within the 3-D model domain. The LPM provides accurate position information because the velocity variables in equations (4.1) – (4.3) are updated every model time step by trilinear interpolation to the actual probe locations. The probes are assumed to have an infinite lifetime until the wind carries them beyond the boundaries of the model domain. The probes are not tracked within six grid zones of the lateral boundaries where enhanced numerical diffusion is used in the transition to external model boundary conditions.

Simulated or virtual weather scenarios make it possible to test a variety of deployment strategies and evaluate how deployment patterns affect probe dispersion, separation distance, and transport lifetime. Candidate deployment patterns include release from: (a) a network of stations at or above the surface of the Earth, (b) UAVs (Holland et al. 2001) for selected remote deployments, (c) conventional aircraft and ocean going vessels, and (d) high-altitude balloons (Girz et al. 2002; Pankine et al. 2002). An important objective for Phase II is to examine in detail the effects of dispersion and the resulting probe distributions from these potential deployment strategies.

Rather than assume a specific deployment strategy for the Phase I project, a random distribution was chosen for the initial positions of the simulated probes in the GEMS network. A pre-determined number of probes were placed randomly into a 3-D domain in order to achieve a desired average probe spacing (see Section 4.5.1 for specific details). The randomization was designed to simulate a well-mixed distribution of probes that retain little memory of the initial deployment pattern. It was assumed that the highly non-linear dynamics of the atmosphere would create such a distribution after several days. However, additional experiments are required over larger domains with simulated deployments continuing for days or weeks to determine whether randomization is realistic or achievable for different weather scenarios and deployment strategies.

## 4.4 Simulated Observations

To simulate measurements obtained from probes or conventional instrumentation, the tri-linear interpolation algorithm is used to extract values of temperature, humidity, and pressure at locations throughout the model integration. Assuming the probes are passive tracers, temporal changes in their absolute or relative position are used to estimate wind velocities. Finally, a random component to represent instrument error can be added to the simulated observations in order to address questions regarding instrument accuracy.

## 4.5 Observing System Simulation Experiments (OSSEs)

OSSEs are used to assess the impact of simulated probe data on forecasts of the selected weather event within a regional domain. OSSEs have been conducted for decades in meteorology to (a) evaluate the potential impact of proposed remote and in situ observing systems, (b) determine trade-offs in instrument design, and (c) evaluate the most effective DA methodologies to incorporate the new observations into regional and global NWP models (Arnold and Dey 1986; Rohaly and Krishnamurti 1993; Atlas 1997; De Ponca and Zou 2001). A framework following Atlas (1997) and Lord et al. (1997) is used to perform the OSSEs.

The results from OSSEs are generally considered more robust if (a) different models are used for the reference run and subsequent assimilation and forecasts, and (b) benchmark experiments are performed with the system using real observations to assess the actual impact of current operational systems and compare these results with the OSSEs. While these characteristics of an OSSE design are desirable, they were beyond the scope of the NIAC Phase I effort and were not essential to obtain meaningful OSSE results as demonstrated recently by Kuo et al. (1997).

### 4.5.1 Methodology

This section describes the configuration of ARPS and ADAS in a series of regional OSSEs to demonstrate the potential impact of a network of GEMS over the Florida peninsula and adjacent coastal waters. The case selection for the OSSEs is 15 June 2001, when strong thunderstorm activity developed during the afternoon hours along the sea-breeze fronts across central and southern Florida. The purpose of these experiments is not to replicate the real atmosphere from 15 June, but rather to establish a framework for demonstrating the impact of a hypothetical network of probes.

The OSSE methodology consists of three steps:

- **Reference or Nature simulation.** This forecast run is considered “truth”, and the trajectories of all simulated probes are tracked and extracted from this model simulation.
- **Control simulation.** The Control run is configured in such a manner as to generate a significantly different solution from the Nature simulation to approximate the differences between a state-of-the-art model and the real atmosphere (Atlas 1997). This is accomplished by using initial and boundary conditions from a different operational model than used for the Nature simulation, and by initializing ARPS 12 hours earlier than the Nature simulation.
- **OSSEs.** The various OSSEs are identical to the Control forecast run, except that simulated probe data are intermittently assimilated into ARPS at specified times.

Each step in the OSSE methodology is described in more detail in the following sub-sections.

#### 4.5.1.1 Nature Simulation

For the Nature simulation, the ARPS/LPM was configured for a high-resolution regional domain covering all of the Florida peninsula and adjacent coastal waters with 4-km horizontal grid spacing (Fig. 4.1). The ARPS was initialized at 1200 UTC 15 June and integrated for 12 hours to 0000 UTC 16 June. The Nature simulation obtained its initial and boundary conditions from bi-hourly analyses of the Rapid Update Cycle (RUC) model (Benjamin et al. 1998) from 1200 UTC 15 June to 0000 UTC 16 June 2001. No observational data were assimilated into the ARPS for the Nature simulation.

A total of 34,560 probes were randomly placed in a subset domain within the 4-km simulation grid from the surface to 15 km. The probe deployment domain is shown in Fig. 4.1. The 3-D distribution of probes at 1200 UTC 15 June 2001 shown in Figure 4.2 was designed to simulate average probe separation distances of roughly 16 km in the horizontal and 1 km in the vertical directions. Since probes were removed from the domain at the downwind boundaries by the simulated environmental flow, probes were replenished at each boundary assuming a random distribution. At every 15 minutes of integration, 720 probes were introduced at each lateral boundary (the westernmost and easternmost y-z planes, and northernmost and southernmost x-z planes) for a total of 2,880 additional probes. This random re-introduction of probes continued during the 6-hour deployment window from 1200 to 1800 UTC 15 June (0- to 6-h forecast times).

The probes positions were tracked during all 12 hours of integration and the simulated meteorological measurements of temperature, pressure, relative humidity, and winds were recorded every 15 minutes during the lifetime of each probe within the deployment domain of Figure 4.1. Simulated probe measurements were subsequently assimilated in the OSSEs over a subset area of the deployment domain. The number of probes as a function of time and altitude over the deployment and assimilation domains are given in Figure 4.3 for all 12 hours of the ARPS Nature simulation. Note that the number of probes at upper levels decreases with time due to the  $-0.08 \text{ m s}^{-1}$  terminal velocity for each probe.

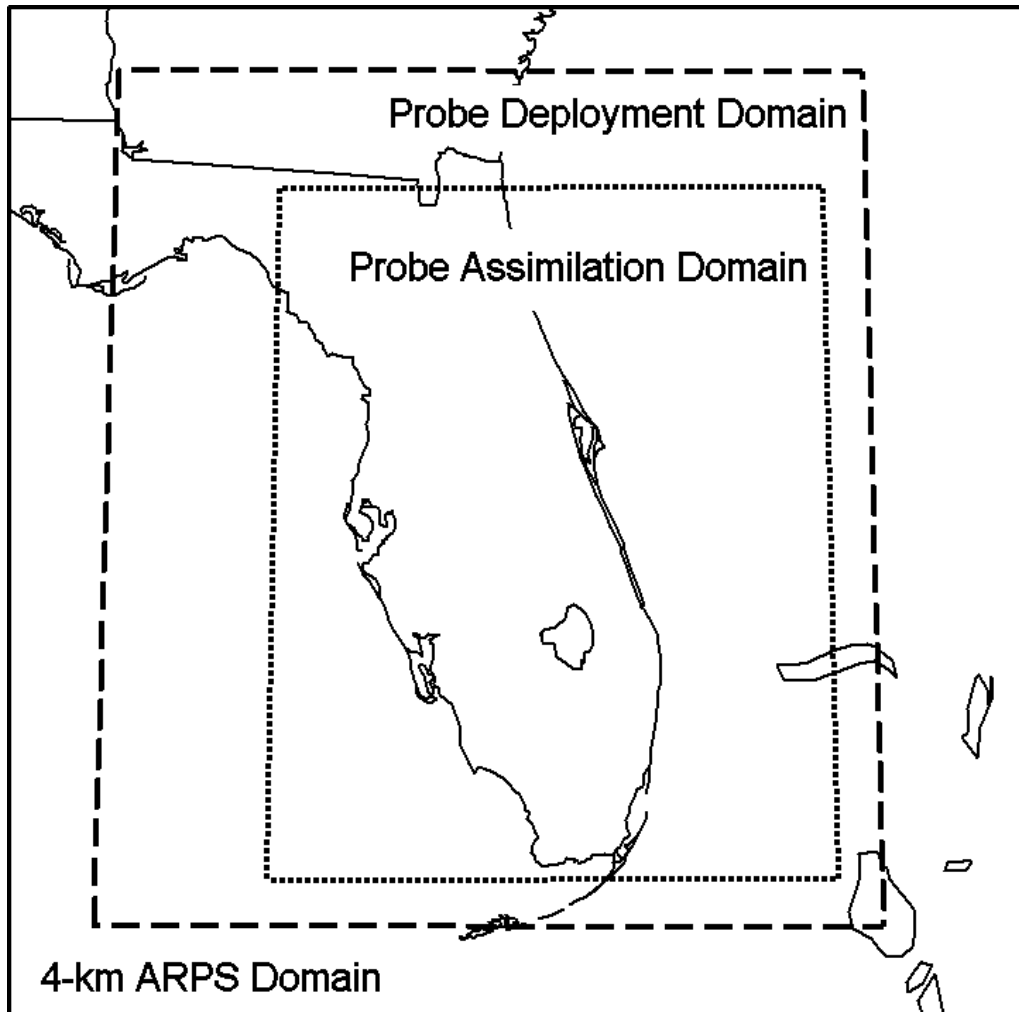


**Figure 4.1** Locations of the GEMS probe deployment and assimilation domains nested within the 4-km ARPS Nature simulation domain. The area inside the box bounded by the long dash lines represents the probe deployment domain while the subset area bounded by the dotted lines represents the probe assimilation domain.

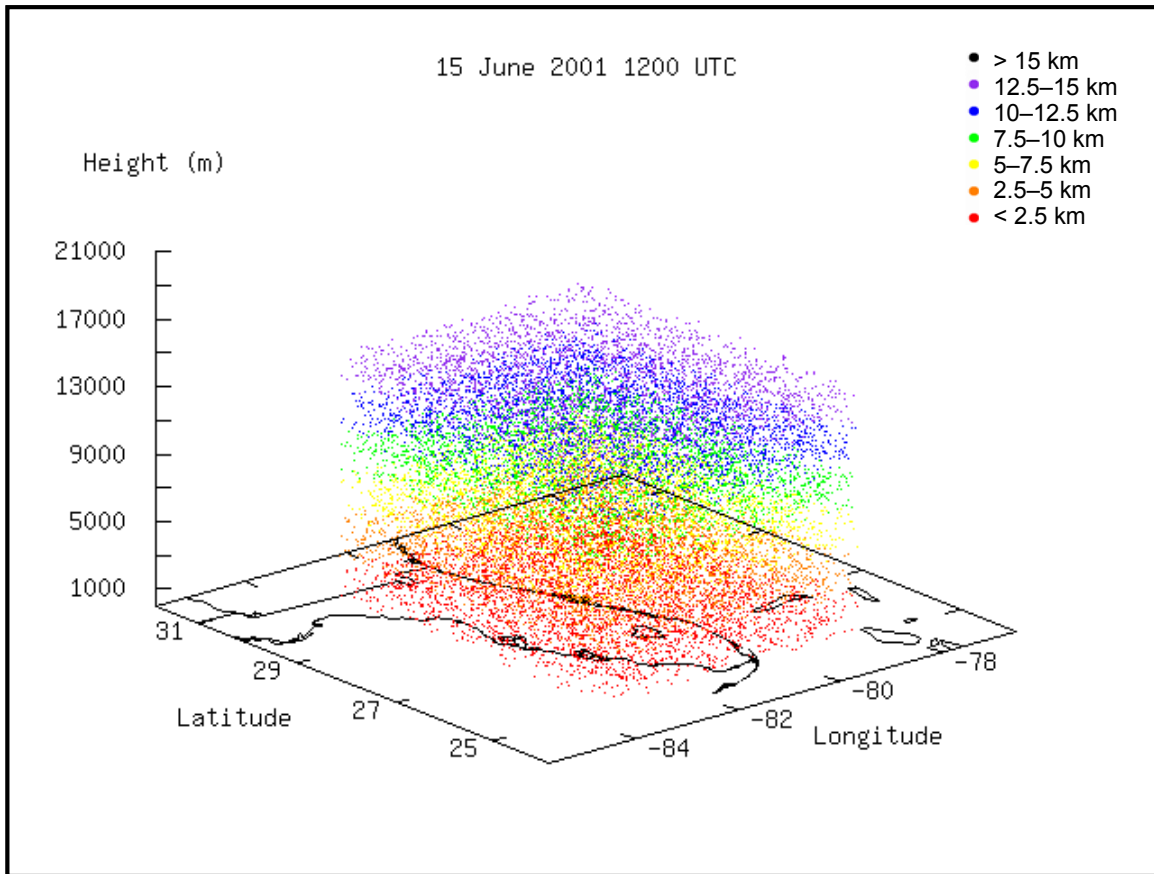


**Figure 4.2** Three-dimensional display of the initial probe distribution at 1200 UTC 15 June 2001. The altitude is denoted by colors according to the key provided in the upper right, where red represents the lowest altitudes and black represents the highest altitudes.

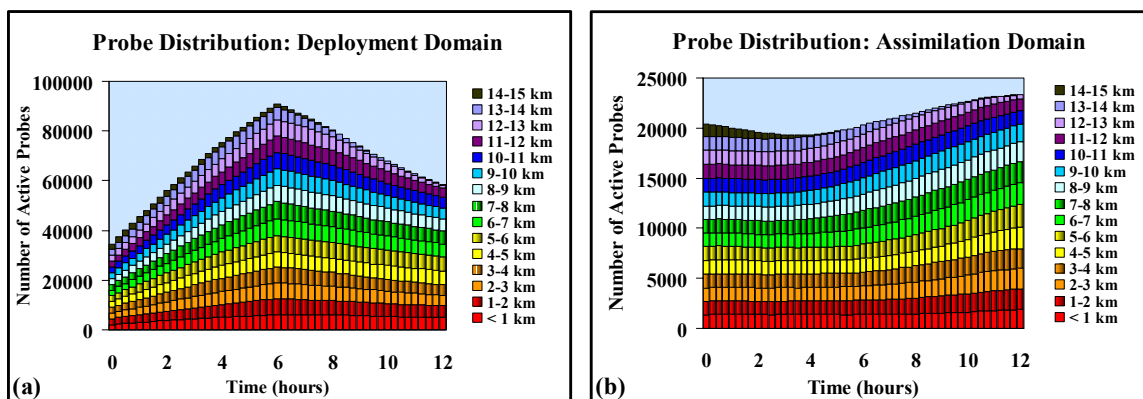


**Figure 4.3** The number of probes as a function of time and altitude in the (a) deployment domain (outer dashed box in Fig. 4.1), and (b) assimilation domain (inner dotted box in Fig. 4.1). The y-axis ranges from 0 to 100000 in (a), and from 0 to 25000 in (b).

#### 4.5.1.2 Control Simulation

Unlike traditional OSSEs, the Control and OSSEs conducted in this study used the same NWP model as in the Nature simulation, which is referred to as the “identical twin” configuration following Kuo et al. (1997). To achieve a significantly different forecast relative to the Nature simulation, the initialization time, initial

conditions, and boundary conditions were changed. In addition, the Control simulation was conducted on three separate grids with one-way interactive nesting, compared to the single 4-km forecast grid in the Nature simulation.

The Control experiment was started at 0000 UTC 15 June, or 12 h earlier than the Nature run. The initial conditions were obtained from the NOGAPS forecast run initialized at 0000 UTC 15 June; thus, the NOGAPS 0-h forecast served as the initial condition for the Control simulation. The outermost ARPS Control run (Grid A in Fig. 4.4 with 64-km horizontal resolution) used NOGAPS forecast output every 6 hours as boundary conditions (6-, 12-, 18-, and 24-h NOGAPS forecasts).

Once the 64-km ARPS Control simulation completed, the Control forecast on the first nested grid was run using the 64-km ARPS forecast output every hour as boundary conditions (Grid B in Fig. 4.4 with 16-km horizontal resolution). Finally, the ARPS Control simulation on the innermost grid was conducted using the 16-km ARPS hourly forecast output as boundary conditions (Grid C in Fig. 4.4 with an identical grid configuration to the Nature run). The multiple one-way nested grids for the Control and OSSEs were used to cascade the scales from the coarse NOGAPS horizontal resolution ( $1^\circ \times 1^\circ$ , or about 111 km), to the finer 4-km regional grid over Florida and surrounding waters. OSSEs conducted on the 4-km grid also used hourly boundary conditions from the 16-km ARPS Control run. The physical grid configurations for all three grids of the Control simulation are summarized in Table 4.3.



**Figure 4.4** Grid configuration for the ARPS Control and OSSE simulations. Grid A is the outer ARPS Control domain with 64-km grid spacing, grid B is the ARPS Control domain with 16-km grid spacing, and grid C is the ARPS Control and OSSE domain with 4-km grid spacing. Grid C is identical to the 4-km Nature simulation domain shown in Figure 4.1.

**Table 4.3** Summary of ARPS grid configurations for the Nature and Control simulations. The number of grid points in the east-west, north-south, and vertical directions is given by NX, NY, and NZ respectively. Only Grid C was used for the Nature simulation.

Grid	Horizontal Resolution (km)	Average Vertical Resolution (m)	NX	NY	NZ	Domain Size (km)
A	64	425	153	73	45	9792 x 4672 x 19
B	16	425	303	193	45	4848 x 3088 x 19
C	4	425	225	223	45	900 x 892 x 19

### 4.5.1.3 OSSEs

The configuration of the OSSEs is identical to the Control configuration, except that simulated probe data were assimilated at selected times of the model integration. For the experiments presented in this report, all simulated probe data were assimilated into the model between 1500 and 1800 UTC 15 June, prior to and during convective initiation across the Florida peninsula in the Nature run.

Figure 4.5 depicts a timeline summary of the relationships between Nature, Control, and the OSSE configurations on 15 June. The Control and OSSEs began at 0000 UTC 15 June and were integrated for 24 h to 0000 UTC 16 June. The simulated probe data were extracted from the 12-h Nature run beginning at 1200 UTC 15 June. Each OSSE assimilated the simulated probe data over the same time window and comparison error statistics were computed from 1200 UTC 15 June to 0000 UTC 16 June over the area of the probe assimilation domain in Figure 4.1. The error statistics include the root mean square (RMS) error, bias, and the error standard deviation (SD) following Nutter and Manobianco (1999). If  $\Phi$  represents a predicted variable from the Control simulation or OSSEs, then forecast error is defined as

$$\Phi' = \Phi_{\text{exp}} - \Phi_{\text{nat}}, \quad (4.4)$$

where the subscripts *exp* and *nat* denote the experiment (Control or OSSE) and Nature quantities, respectively. The bias represents the average model error of the Control or OSSEs, and is computed as

$$\text{Bias} = \frac{1}{N} \sum_{i=1}^N \Phi', \quad (4.5)$$

where N represents the total number of grid points at any given height in the atmosphere. The RMS error is calculated as

$$\text{RMS Error} = \sqrt{\frac{1}{N} \sum_{i=1}^N (\Phi')^2}, \quad (4.6)$$

By applying the Murphy (1988) decomposition for RMS error, the SD of the errors is given by

$$\text{SD} = \sqrt{\text{RMS}^2 - \text{Bias}^2} \quad (4.7)$$

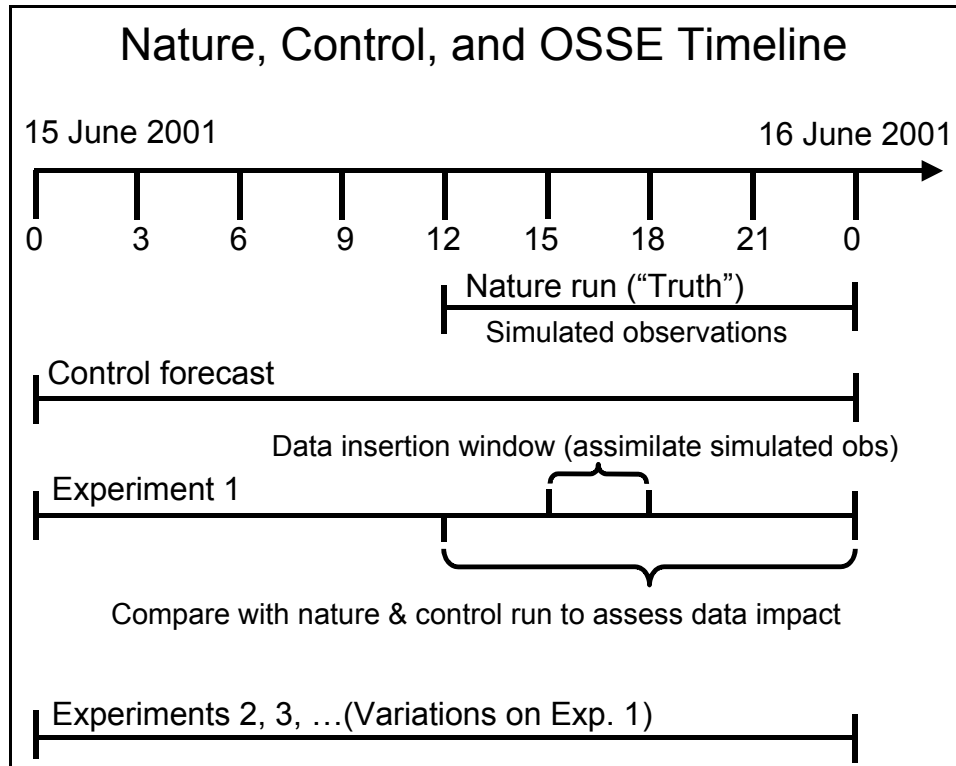


**Figure 4.5** Timeline of the Nature run for extracting simulated GEMS observations, the Control forecast, and OSSE experiments conducted on 15–16 June 2001.

Data were assimilated into the OSSE using an intermittent DA technique (Rogers et al. 1996). This technique incorporated information from the simulated probe data into the model integration by alternately generating an ADAS analysis and integrating the ARPS NWP model for short time intervals using the ADAS initial condition. This process continued for a sufficient length of time to allow for the model to achieve a dynamical balance.

The intermittent DA process used during the 3-h data insertion window (Fig. 4.5) is illustrated by the flowchart in Figure 4.6. Once the Control simulations were completed, the first ADAS analysis with GEMS data was performed at 1500 UTC (given by  $T$ ) using the Control ARPS forecast as a first-guess field, and represented the beginning of the DA cycle. After the initial ADAS analysis, the ARPS model was integrated for 30 minutes (given by  $dt$ ) using the ADAS analysis as the initial condition. The subsequent ADAS analysis incorporated new probe data at  $t + dt$  minutes, and used the ARPS forecast at  $t + dt$  as the new first-guess field for the analysis. The intermittent cycle was repeated  $n$  times, where  $n$  is an integer counter. The final  $n$  was 6 in these OSSEs based on the frequency and length of the data insertion window.

The preferred DA method for incorporating the simulated data into the ARPS model is incremental analysis update (IAU, Bloom et al. 1996); however, this portion of the ARPS source code has not yet been optimized for the message passing interface (MPI) software. Code design with the MPI is required to perform the grid computations across multiple processors and communicate this information to each separate node of the hardware cluster. Because of the large computational grids developed for these experiments and time constraints of the Phase I effort, it would not have been efficient to perform the DA on a single processor using IAU. However, it is goal to ensure that a DA scheme such as IAU is utilized for OSSEs conducted within the Phase II effort.

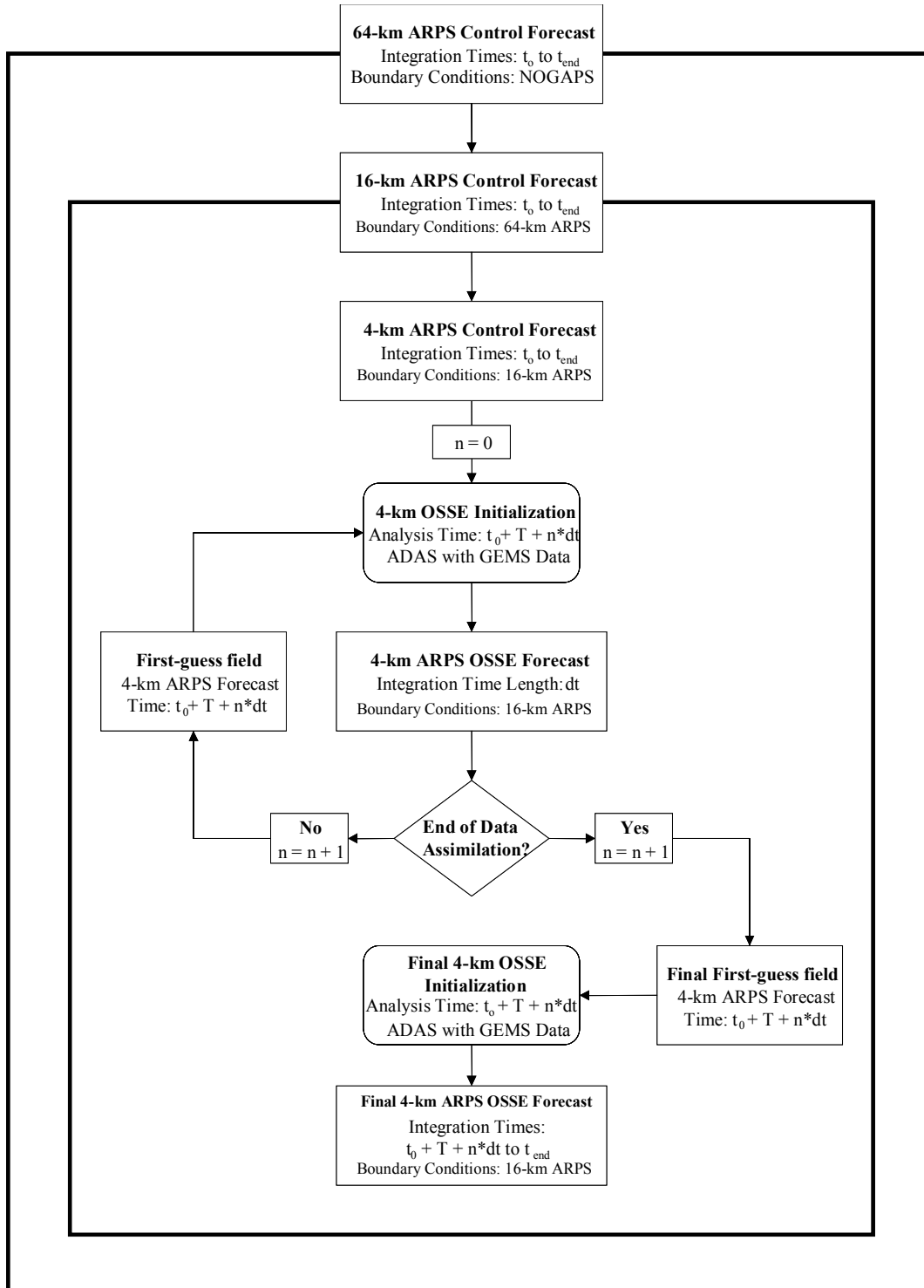


**Figure 4.6** Flowchart for the Control and OSSE forecast / DA cycle. The Control forecast is initially run on the 64-km, 16-km, and 4-km grids from  $t_0$  to  $t_{end}$ , where  $t_0 = 0000$  UTC 15 June 2001 and  $t_{end} = 0000$  UTC 16 June 2001 (24 total forecast hours). The outer (inner) box represents the 64-km (16-km) ARPS forecasts that force the 16-km (4-km) ARPS forecasts at the lateral boundaries in a 1-way nested mode.

A total of 7 OSSEs were conducted for this project, and the details of each experiment are summarized in Table 4.4 along with the Nature and Control simulations. Each OSSE with the exception of Experiment 5 assumed perfect observations with no instrument errors. In Experiment 5, random errors of the following magnitude were added to each variable, commensurate with typical errors of MEMS sensors (Kristofer S. J. Pister, personal communication):

- Temperature:  $\pm 0.5^{\circ}\text{C}$
- Relative Humidity:  $\pm 5\%$  ( $\sim \pm 2^{\circ}\text{C}$  dew point)
- Pressure:  $\pm 1$  hPa
- u- / v- winds:  $\pm 1$  m s<sup>-1</sup>

Experiment 1 assimilated all variables from the simulated probe data, whereas Experiments 2–4 withheld RH, winds, and temperature, respectively. Finally, Experiments 6 and 7 reduced the total number of probes by 50% and 25%, respectively. The probes were excluded randomly throughout the probe assimilation domain to reduce the effective resolution of the assimilated data. The results of these OSSEs are presented in the next section and compared to the Nature and Control simulations.

<b>Table 4.4</b> Summary of the simulations and OSSE experiments for 15–16 June 2001. For each experiment, the variables assimilated into the OSSE (if applicable) are provided, along with a description of the model initial and boundary conditions and DA details.		
<b>Simulation</b>	<b>Variables Assimilated</b>	<b>Experiment Description</b>
Nature	N/A	<i>Initial conditions:</i> 1200 UTC RUC analysis <i>Boundary Conditions:</i> RUC analyses every two hours <i>ARPS 12-h simulation</i>
Control	N/A	<i>Initial conditions:</i> 0000 UTC NOGAPS analysis <i>Boundary Conditions:</i> 0- to 24-h NOGAPS forecasts <i>ARPS 24-h simulation</i>
OSSE Experiment 1	T, p, RH, u, v*	Same as Control, but including GEMS DA <i>Frequency:</i> every 30 minutes <i>Time window:</i> 1500 to 1800 UTC
OSSE Experiment 2	T, p, u, v	Same as Exp. #1, but excluding RH
OSSE Experiment 3	T, p, RH	Same as Exp. #1, but excluding u, v (winds)
OSSE Experiment 4	p, RH, u, v	Same as Exp. #1, but excluding T
OSSE Experiment 5	T, p, RH, u, v	Same as Exp. #1, but including random probe errors
OSSE Experiment 6	T, p, RH, u, v	Same as Exp. #1, but using only 50% of GEMS data
OSSE Experiment 7	T, p, RH, u, v	Same as Exp. #1, but using only 25% of GEMS data

\*T = temperature, p = pressure, RH = relative humidity, u = u-wind component, v = v-wind component.

#### 4.5.2 Results

The OSSEs were designed to test the sensitivity of ingesting or excluding various probe measurements into the model simulations using a comparison to the Nature simulation. These experiments provided information that will be needed in the future to help design and develop the probes and their measurement capabilities. There are many ways to assess the sensitivity of varying inputs but this analysis focused on comparing some basic statistics and analyzing model-predicted precipitation fields.

The statistics provide a straightforward comparison of the model simulations with the Nature and Control simulations. The statistics were computed from gridded forecast error fields where the Nature simulation represented the “observed” field and the Control and experiment simulations represented the “forecast” field.

These statistics reveal the immediate positive impact of GEMS data insertion for the primary variables (e.g. temperature, humidity, wind).

The precipitation fields provide an additional composite comparison by varying the inputs on the experiment simulations with the Nature and Control simulations. Precipitation is a quantity that requires the correct prediction and interaction of all the non-linear effects of varying input parameters to be forecast accurately. Forecast precipitation reflects how well the four-dimensional (space and time) dynamical and physical processes in the NWP model are working.

Overall, the OSSEs demonstrated that the assimilation of probe observations extracted from the Nature simulation had a significant impact on improving the predicted primary variables and precipitation forecasts over the Control simulation. The results also showed that simulated temperature and humidity observations had the largest impact on the subsequent forecasts.

#### **4.5.2.1 Sensitivity Analysis**

For this report, graphs of the bias and RMS error at the 850-, 500-, and 300-hPa levels of the atmosphere were generated to summarize the statistics for the OSSEs (Figs. 4.7 through 4.9). For brevity in this report, the graphs for the random errors (e.g. SD) were not shown since they were all similar to the RMS errors. These pressure levels were chosen to represent fields for the lower, middle, and upper troposphere, respectively. The graphs provide tools for assessing the sensitivity of including or excluding various probe measurements. It should be noted that the temperature errors were small since this was a summer case and the horizontal temperature gradients were not large. The dew point rather than relative humidity was used for verification purposes because with perfect forecasts of absolute moisture variables (e.g. mixing ratio, dew point, etc.), there can still be relative humidity errors due to erroneous temperature forecasts. The relative humidity errors can mask the actual moisture bias and effectively indicate a saturation bias only.

#### **Experiment 1**

Experiment 1 ingested simulated data from the probe assimilation domain shown in Figure 4.1. All sampled primary meteorological variables were assimilated into this OSSE (Table 4.4). Following the initial assimilation of probe data at 1500 UTC, the dew point biases and RMS errors decreased substantially compared to the Control simulation at each level (Fig. 4.7). After the assimilation window, the RMS error increased from 1–2 K at all three levels at 1800 UTC to 4–6 K after 2300 UTC (Figs. 4.7d-f). At 500 hPa, the Control simulation was too dry late in the simulation with a bias of -6 K, whereas Experiment 1 showed a vast improvement with a bias at the 500-hPa level near 0 K (Fig. 4.7b). Meanwhile, the Control simulation had much larger RMS errors, ranging from 5–9 K after 1800 UTC at all levels.

The graphs of the temperature bias comparing the Control and Experiment 1 show little bias at the 850-hPa level but indicate a cold bias at the higher levels (500 and 300 hPa, Figs. 4.8a-c). The temperature RMS errors (Fig. 4.8d-f) showed quite a different pattern when comparing Experiment 1 to the Control simulation. The temperature RMS error in Experiment 1 increased from 0.3 K at 1800 UTC at the 850-hPa level up to 1.2 K by 0000 UTC while the temperature RMS error for the Control simulation at 850 hPa decreased from 1.3 K at 1800 UTC to 0.8 K by 0000 UTC (Fig. 4.8f). The Control simulation actually had temperature RMS errors that were less than or equal to the Experiment 1 RMS errors for the final two hours of the simulation (2200–0000 UTC). The reason for the decreased RMS errors in the temperature during the final two hours of the Control simulation could be related to the delayed onset of clouds and precipitation compared to the Nature run.

The v-wind component errors show that the Experiment 1 simulation had smaller RMS errors and biases compared to the Control simulation at all times during and following the assimilation window (Fig. 4.9). In fact, all of the experiment simulations produced very similar RMS errors and biases except for Experiment 3, which is the simulation made with no wind data. The trend between 1800 and 0000 UTC indicates that the differences in errors between the various experiments and the Control simulation become more similar with time; however, the experiment simulations all have lower biases and RMS errors overall.

#### **Experiment 2 – No Relative Humidity**

Experiment 2 included the same probes as in Experiment 1 but the RH variable was excluded from assimilation. The most significant impact of excluding the RH data was on the forecast dew point results. The graphs of dew point RMS error showed that the Experiment 2 errors were the same or worse than the Control

simulation at all levels for the entire simulation time after 1400 UTC (Fig. 4.7 d-f). The graphs of dew point bias showed that the bias after 2000 UTC at 850 and 500 hPa was better than the Control simulation but was worse than the Control simulation at 300 hPa (Fig. 4.7 a-c).

### **Experiment 3 – No Wind**

Experiment 3 included the same probes as in Experiment 1 but the wind data were excluded from assimilation. Excluding the wind data had virtually no effect on the dew point and temperature forecast errors (Figs. 4.7 and 4.8, respectively) but had significant influence on the v-wind errors (Fig. 4.9). The graphs of the v-wind bias and RMS error show very little difference between Experiment 3 and the Control simulation at the 850- and 500-hPa levels; however, at 300 hPa, the v-wind RMS errors for Experiment 3 were 1-2  $\text{m s}^{-1}$  lower than the Control simulation, and about 1  $\text{m s}^{-1}$  larger than the other experiments for the period 1800 to 0000 UTC (Figs. 4.9d-f).

### **Experiment 4 – No Temperature**

Experiment 4 included the same probes as in Experiment 1 but the temperature data were excluded from assimilation. By excluding temperature, the magnitude of the dew point errors of Experiment 1 degraded to that of the Control simulation (Fig. 4.7). This result in combination with Experiment 2 indicates the importance of incorporating both temperature and moisture data from GEMS in order to obtain an improved moisture forecast during a convective weather situation. Interestingly, the temperature errors do not show as much degradation as the dew point errors; however, the errors do approach the magnitude of the Control errors, particularly at 850 hPa (Fig. 4.8). Excluding temperature data had no significant impact on the forecast v-wind errors at the 850- and 500-hPa levels but the 300-hPa RMS errors exceeded the Control simulation errors for the period 2300–0000 UTC (Fig. 4.9d).

### **Experiment 5 – Instrument Errors**

Experiment 5 included the same probes as in Experiment 1 but the probe data were perturbed by introducing random errors for temperature, relative humidity, pressure, and winds as described in Section 4.5.1.3. Introducing random error made very little difference in the model results when comparing the RMS errors and biases between Experiments 5 and 1. The bias and RMS errors were nearly identical for all times, levels, and variables (Figs. 4.7–4.9).

### **Experiment 6 – 50% of probe data and Experiment 7 – 25% of probe data**

Experiment 6 included data from 50% of the probes used in Experiment 1 and Experiment 7 included data from 25% of the probes. The methodology for excluding the probes was described in Section 4.5.1.3. Excluding probes from the DA into the model did not substantially degrade the forecast of temperature, dew point, or winds when comparing the RMS errors and biases of Experiments 6 and 7 to Experiment 1 (Figs. 4.7–4.9). The only notable exception was slightly higher dew point RMS errors (by approximately 1–2 K) in each of the reduced probe simulations at the 300-hPa level during the period 1900–0000 UTC (Fig. 4.7d).

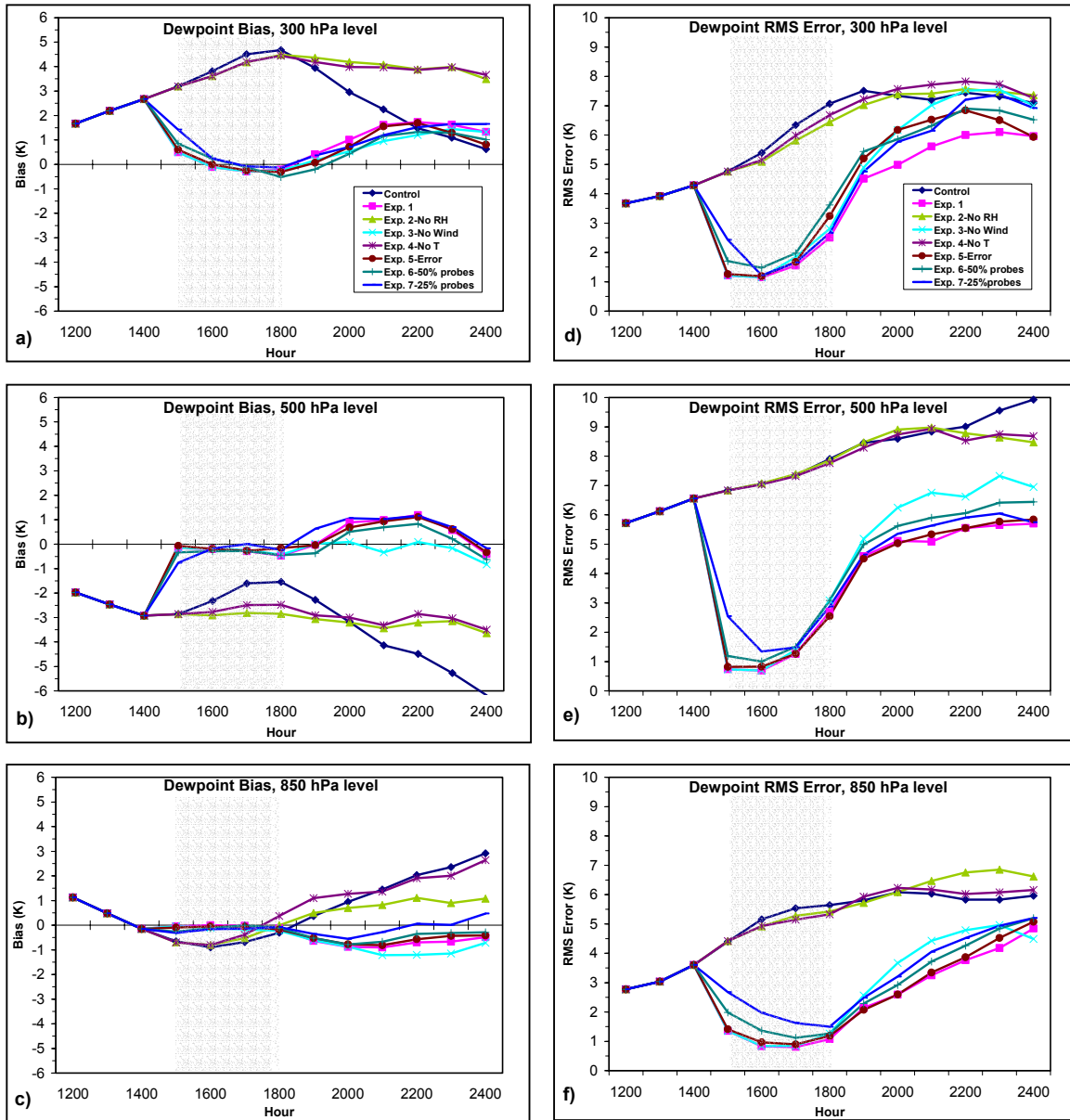


**Figure 4.7** Graphs of the dew point root mean square (RMS) error and bias (Kelvin) for the Control and OSSE experiments 1 through 7. Data are presented for the 300-, 500-, and 850-hPa levels for the period 1200 UTC 15 June to 0000 UTC 16 June 2001. The shaded area denotes the period of data insertion from 1500 to 1800 UTC. Statistics were computed for the probe assimilation domain shown in Figure 4.1.

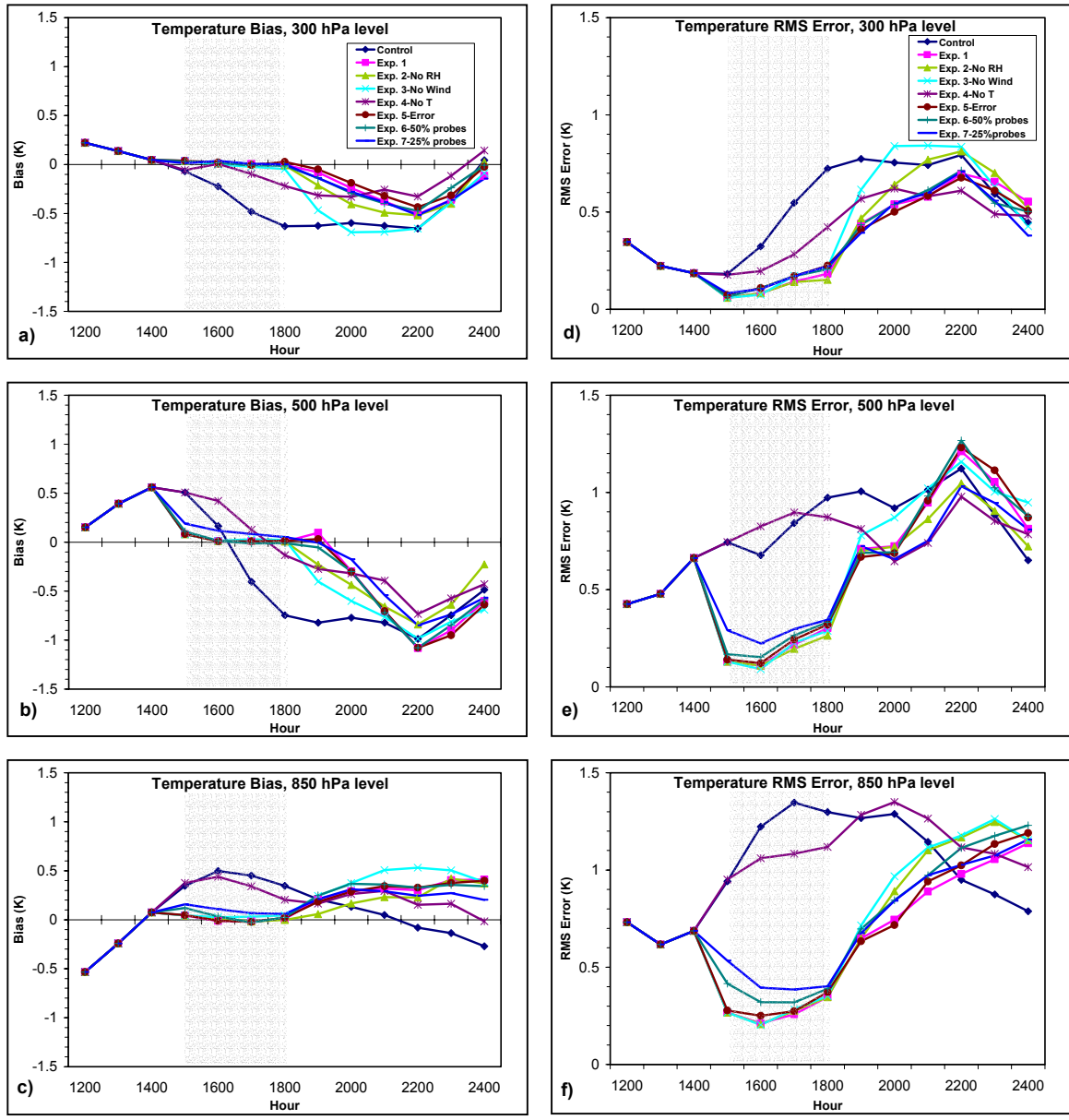


**Figure 4.8** Graphs of the temperature root mean square (RMS) error and bias (Kelvin) for the Control and OSSE experiments 1 through 7. Data are presented for the 300-, 500-, and 850-hPa levels for the period 1200 UTC 15 June to 0000 UTC 16 June 2001. The shaded area denotes the period of data insertion from 1500 to 1800 UTC. Statistics were computed for the probe assimilation domain shown in Figure 4.1.

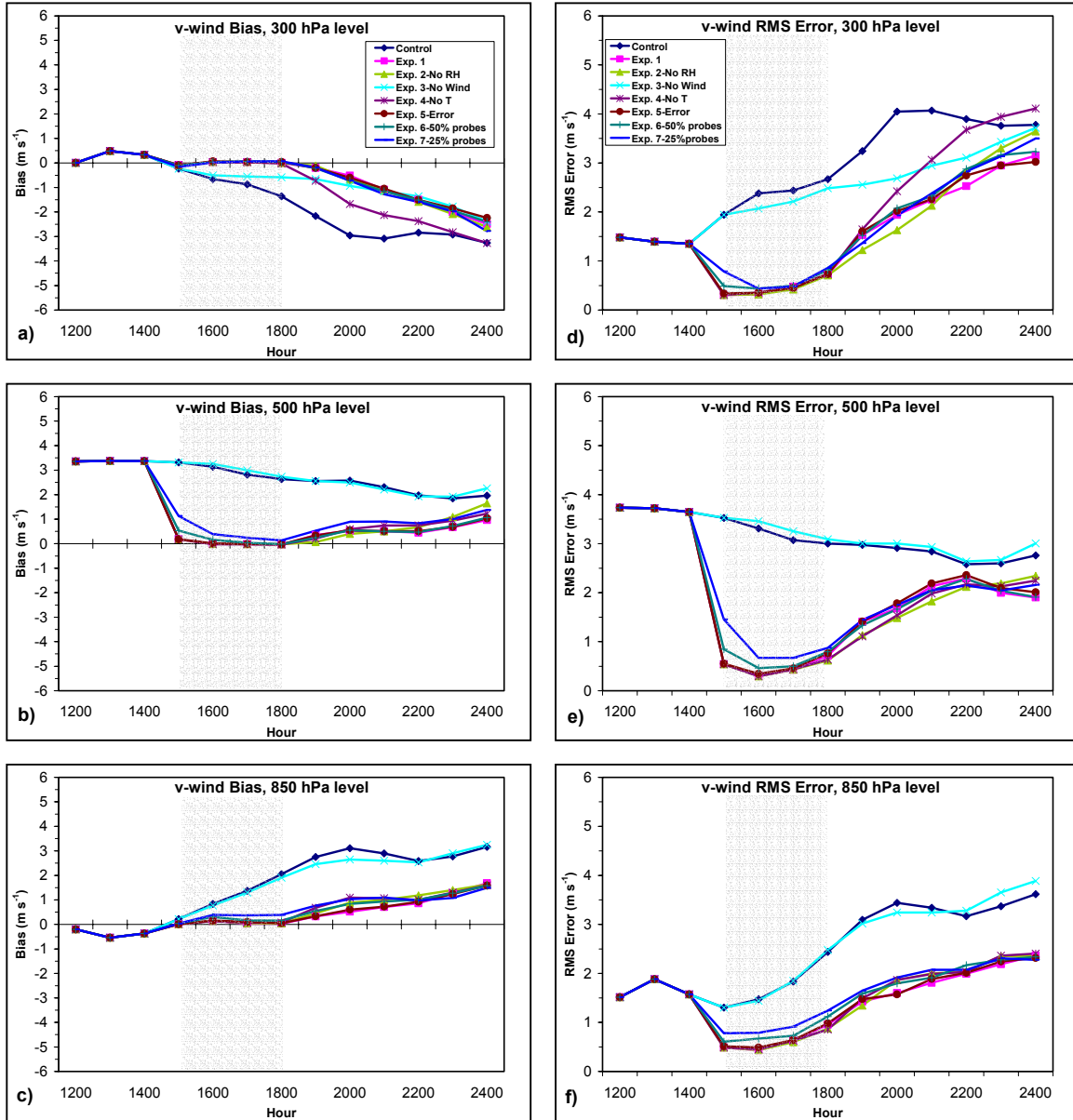


**Figure 4.9** Graphs of the v-wind component root mean square (RMS) error and bias ( $\text{m s}^{-1}$ ) for the Control and OSSE experiments 1 through 7. Data are presented for the 300-, 500-, and 850-hPa levels for the period 1200 UTC 15 June to 0000 UTC 16 June 2001. The shaded area denotes the period of data insertion from 1500 to 1800 UTC. Statistics were computed for the probe assimilation domain shown in Figure 4.1.

#### 4.5.2.2 *Precipitation Analysis*

The maps of the forecast precipitation at two-hour intervals for each OSSE are presented in Figures 4.10-4.12, and provide a comparison with the Nature and Control simulations. Figure 4.10 shows the ARPS cumulative precipitation for the four 2-hour periods from 1600–0000 UTC for the Nature and Control simulations, as well as OSSE Experiments 1 and 2. There is a notable difference between the precipitation fields of the Nature (Figs. 4.10a-d) and Control simulations (Figs. 4.10e-h) for all time periods. In the Nature simulation, ARPS began developing convective precipitation associated with the sea breeze during 1600–1800 UTC in southeast Florida (Fig. 4.10a), increasing in coverage during 1800–2000 UTC (Fig. 4.10b). During these same two 2-hour periods, the Control simulation did not produce any precipitation over Florida (Figs. 4.10e-f). For the period 2000–0000 UTC, the Nature simulation produced convective precipitation over the center of the peninsula extending from southwestern to east-central Florida (Figs 4.10c-d). The Control simulation during this period produced a few areas of scattered precipitation from the southwest coast to northeastern Florida (Figs. 4.10g-h).

Experiment 1 (all probe data) produced precipitation patterns quite similar to the Nature simulation in both areal coverage and timing (Figs. 4.10i-l). Experiment 2 (No RH) produced less precipitation in southwest Florida than the Nature simulation but generated too much precipitation in the north-central Florida peninsula (Figs. 4.10m-p).

Experiment 3 (No Wind, Figs. 4.11e-h) produced a sea breeze with associated convective precipitation that moved inland and toward the west much faster than the Nature simulation (Figs. 4.11a-d). This experiment produced significant precipitation on the west coast of Florida during the period 2200–0000 UTC. Experiment 4 (No T) generated precipitation patterns similar to Experiment 2 except for a fairly large area of precipitation greater than 100 mm over the interior of the peninsula during 2200–0000 UTC (Figs. 4.11i-l).

Experiment 5 (Instrument Error) produced precipitation patterns similar to the Nature simulation except that the precipitation area over east-central Florida began too early and was heavier than the Nature simulation during 2000–2200 UTC (Figs. 4.11m-p). Experiments 6 (50% probes; Figs. 4.12e-h) and 7 (25% probes; Figs. 4.12i-l) produced precipitation patterns similar to each other and to the Nature simulation (Figs. 4.12a-d) except that the east coast sea breeze and associated precipitation areas developed faster and produced precipitation over east-central Florida earlier than the Nature simulation (Figs. 4.12a-l).

A graph of the total grid-averaged two-hour precipitation for the Nature, Control, and each experiment is shown in Figure 4.13. This graph illustrates that all the experiments (except Control) began producing precipitation at 1600–1800 UTC, and slightly under-predicted the total grid precipitation compared to the Nature simulation at these times. At 1800–2000 UTC, Experiment 7 (25% probes) agreed most closely with the Nature simulation at 1.5 mm grid-averaged precipitation. By 2000–2200 UTC, all of the experiments except Experiment 4 (No T) were within 0.2 mm of the Nature simulation. At 2200–0000 UTC, Experiment 1 most closely agreed with the Nature simulation at 0.6 mm. The Control simulation under-predicted the grid-averaged precipitation at all times.

Based on the location of the forecast precipitation patterns and the total grid-averaged precipitation amounts, Experiment 1 (including all variables) seems to match the Nature simulation best compared to the other experiments. However, Experiments 5, 6, and 7 produced precipitation results that closely matched Experiment 1 and the Nature simulation. Experiments 2 and 4 (No RH and No T, respectively) were the least similar to the Nature simulation for precipitation patterns and amount.

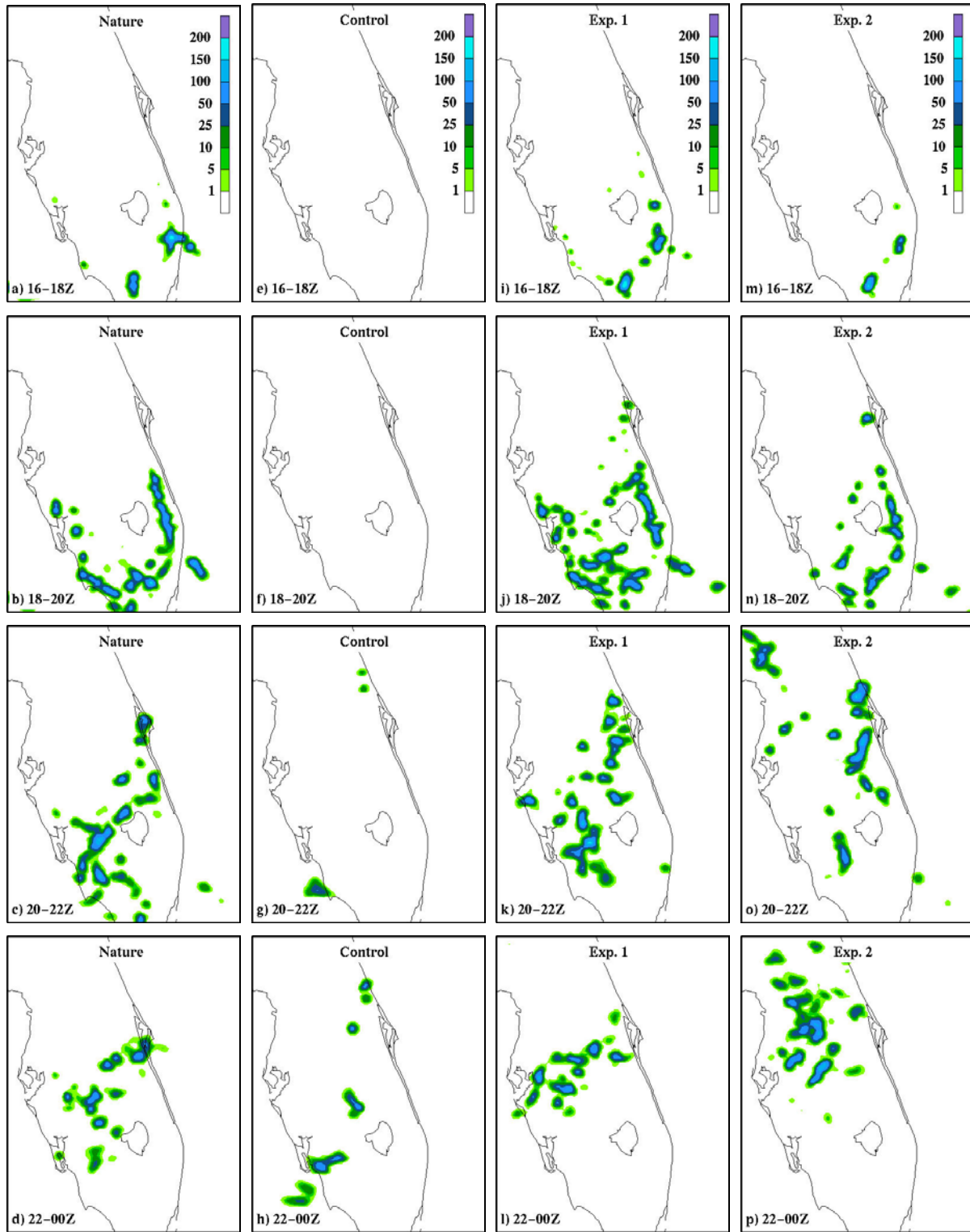


**Figure 4.10** Two-hour accumulated precipitation (mm) for the Nature simulation (a-d), Control simulation (e-h), Experiments 1 (i-l), and Experiment 2 (m-p). Shading depicts total precipitation accumulated at each grid point over the indicated two-hour periods with the legend shown by the color bar in the first panel of each column.

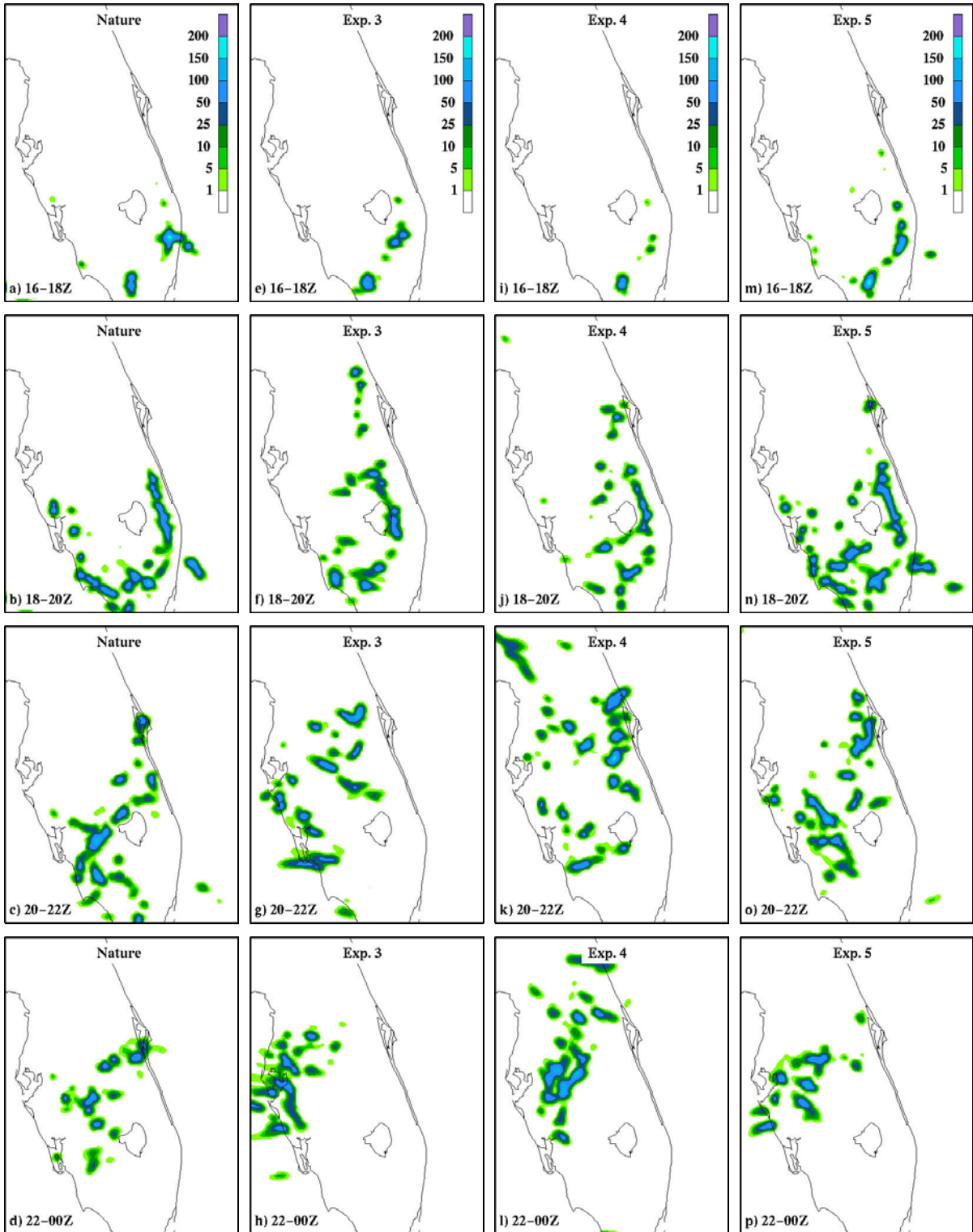


**Figure 4.11** Two-hour accumulated precipitation (mm) for the Nature simulation (a-d), Experiment 3 (e-h), Experiment 4 (i-l), and Experiment 5 (m-p). Shading depicts total precipitation accumulated at each grid point over the indicated two-hour periods with the legend shown by the color bar in the first panel of each column.

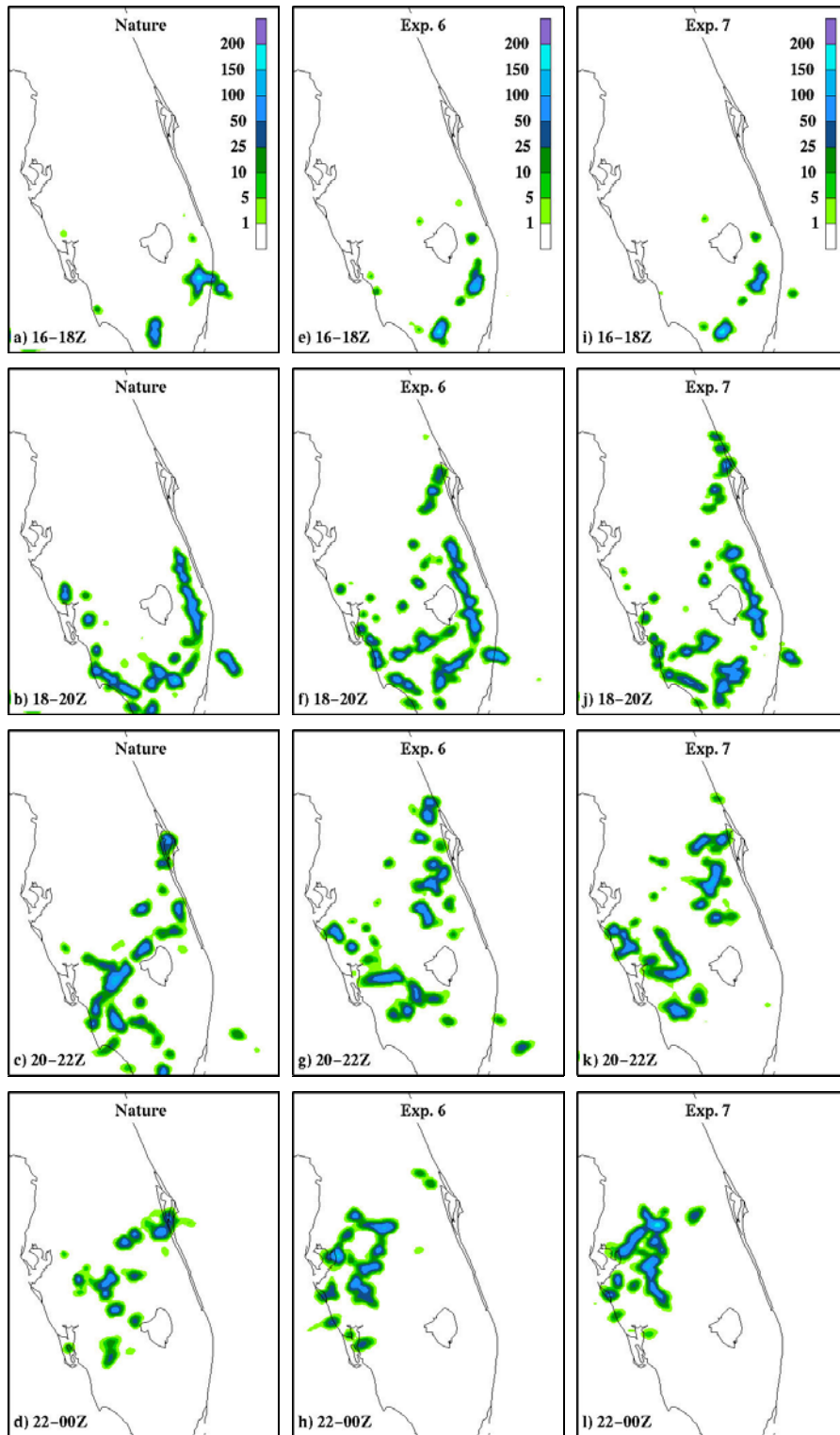


**Figure 4.12** Two-hour accumulated precipitation (mm) for the Nature simulation (a-d), Experiment 6 (e-h) and Experiment 7 (i-l). Shading depicts total precipitation accumulated at each grid point over the indicated two-hour periods with the legend shown by the color bar in the first panel of each column.

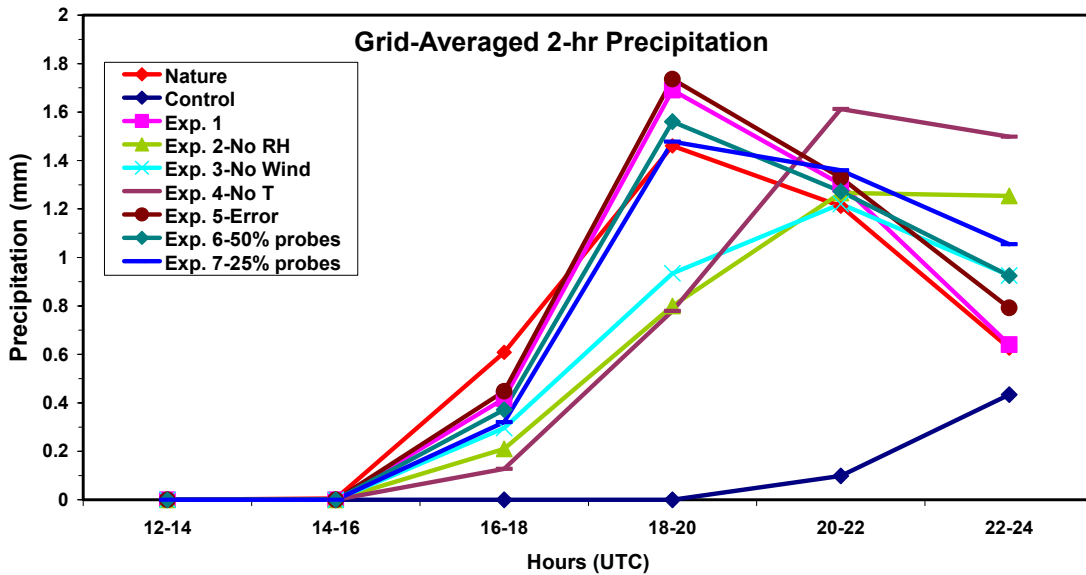


**Figure 4.13** Grid-averaged 2-hour accumulated precipitation (mm) for each ARPS simulation (Nature, Control, and Experiments 1 through 7) over the domain shown in Fig. 4.10. The line type for each simulation is given by the legend in the upper left corner.

#### 4.5.2.3 Results Summary

The key results from the OSSEs were:

- Assimilating data from only 25% of the released probes produced precipitation forecasts that were similar to the Nature run in both location and amount of precipitation. This result is important because the model produced a positive impact on the forecast with a significantly reduced number of probes. In Phase II, tests can be conducted under various deployment scenarios to determine the minimum number of probes required to still produce positive impact on the forecasts and meet communication and networking requirements.
- Excluding temperature, moisture, or wind data in the OSSE framework significantly degraded the model forecast not only for the parameter excluded but for the precipitation forecast as well. These sensitivity tests indicated that, at least for this case study, the maximum data impact resulted when GEMS provided a full suite of temperature, moisture, pressure and wind measurements.
- The inclusion of measurement errors based on current MEMS sensor accuracy did not significantly degrade the forecast for the error tolerances tested. In Phase II, it will important to explore how much observational error can be tolerated for each parameter before degrading forecasts to some pre-determined threshold. This error tolerance will determine if further improvement in sensor accuracy are justified in terms of probe cost and design complexity.

## 5 Other Issues

### 5.1 Hemispheric Deployment

The OSSEs described in Section 4 were used to study the impact of probe data on forecasts within a regional domain. Since the simulations in Phase I were run for short periods of time ( $\leq 24$  hours), they cannot be used to study probe deployment and dispersion over larger spatial and temporal scales. In order to address this issue, the ARPS and LPM were configured to run over most of the northern hemisphere for a period of 24 days from 0000 UTC 15 June through 0000 UTC 9 July 2001. The model configuration for hemispheric runs was identical to that summarized in Tables 4.1 and 4.4 for Grid C except the domain covered the area shown in Figure 5.1 at a horizontal resolution of 75 km. The ARPS initial and boundary conditions were derived from 6-h National Centers for Environmental Prediction – National Center for Atmospheric Research reanalysis (Kalnay et al. 1996). The hemispheric runs were not used to extract simulated observations and perform OSSEs in the Phase I project; however, such experiments will be the primary focus in the Phase II effort to study the major feasibility issues relating to deployment, dispersion, scavenging, and data impacts.

The deployment strategy simulated probe release from stratospheric balloons at an altitude of 18 km every 6 minutes for a period of 4 days from 0000 UTC 15 through 19 June 2001. There were a total of 193,410 probes released in the domain by the end of the deployment period. The terminal velocity of the probes was set to  $-0.01 \text{ m s}^{-1}$  for the hemispheric runs. The high altitude balloons were assumed to be spaced every  $10^\circ$  latitude  $\times$   $10^\circ$  longitude following Pankine et al. (2002), and the simulated deployment did not account for actual balloon drift. Such a deployment strategy is plausible considering that 10 kg of the maximum payload for high altitude balloons (250 kg) constitutes about 4 million probes assuming a probe mass of 2.5 mg each. If the probe volume is on the order of  $1 \text{ mm}^3$ , 4 million probes would occupy a volume of  $\sim 4000 \text{ cm}^3$  and could be released at a rate of one per minute for about 7 years which is well within the expected lifetime of the high altitude balloons (Pankine et al. 2002).

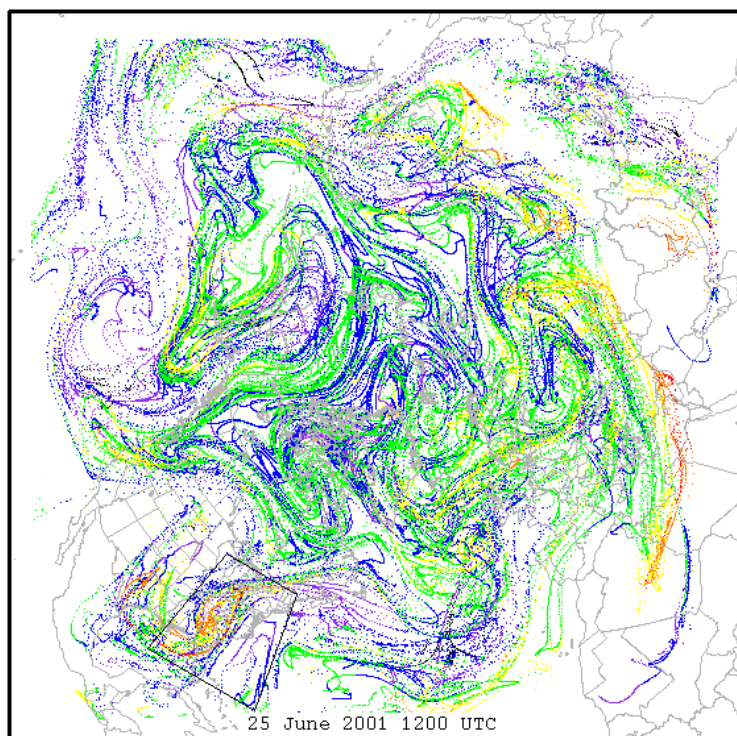


**Figure 5.1** Domain for the hemispheric ARPS simulations and probe positions at 1200 UTC 25 June 2001, 10.5 days after the model initialization time. The probe altitude is denoted by colors according to the key shown in Figure 5.2. The quadrilateral outlined by the thin black line denotes the subset region for 3-D probe positions shown in Figure 5.2.

The spatial distributions shown in Figures 5.1 and 5.2 illustrate how the large-scale atmospheric weather patterns dispersed probes through much of the northern hemisphere despite the fact that probes were released from point sources (simulated stratospheric balloons). In the absence of any vertical air motions, each probe would require more than 20 days to fall from 18 km with a terminal velocity of  $-0.01 \text{ m s}^{-1}$ . After 10.5 days, a large fraction of the probes were still at or above 7.5 km although some could be found at lower altitudes as a result of descending air motions over the eastern U.S. and other locations in the hemisphere (Figs. 5.1 and 5.2). The temporal distribution of probes as a function of altitude (Fig. 5.3) indicates that  $\sim 15,000$  probes descended to levels below 7.5 km with several hundred between the surface and 2.5 km. Figure 5.3 also shows that the total number of probes in the domain decreased after the end of the deployment period (4 days) while the number of probes at lower altitudes increased with time.

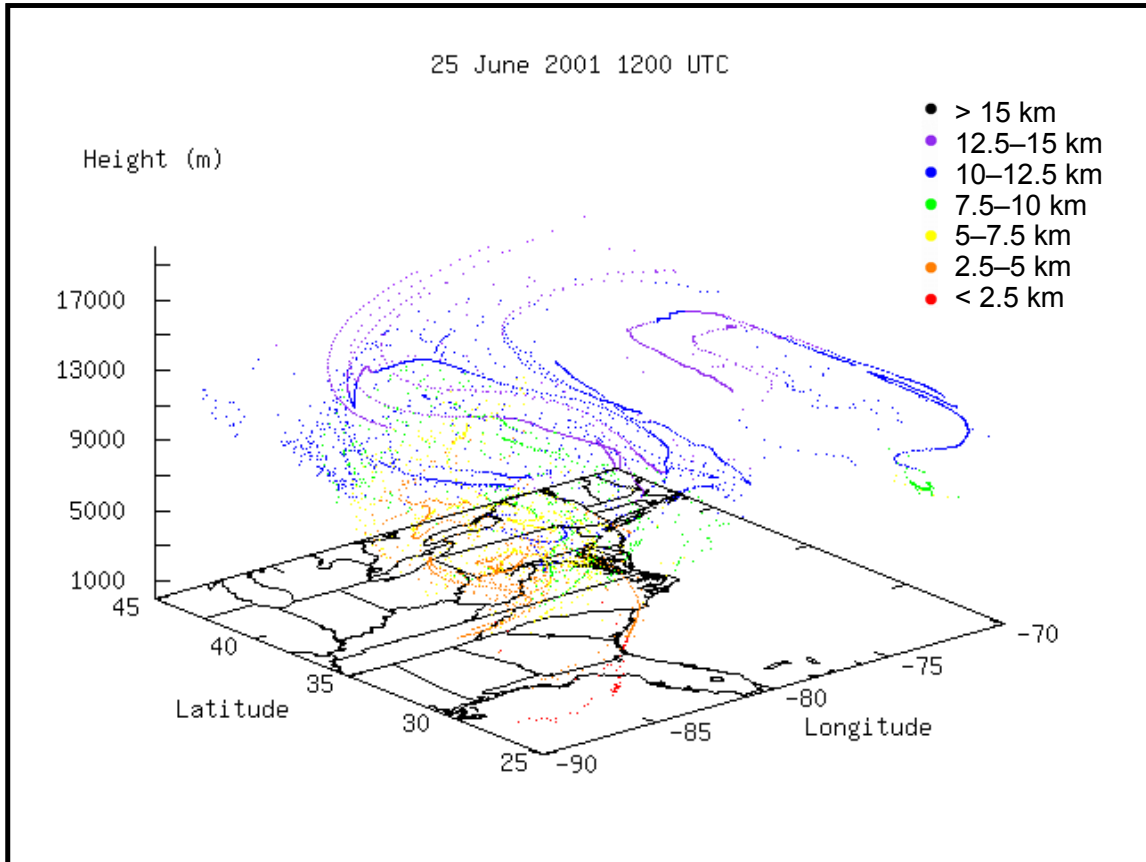


**Figure 5.2** Three-dimensional display of probe positions at 1200 UTC 25 June 2001 over the subset region delineated by the quadrilateral in Figure 5.1. The probe altitude is denoted by colors according to the key provided in the upper right, where red represents the lowest altitudes and black represents the highest altitudes.

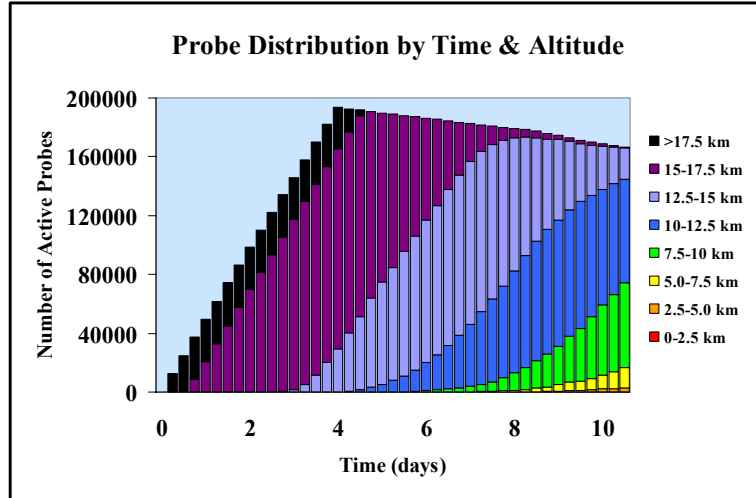


**Figure 5.3** The probe distribution as a function of time and altitude over the hemispheric domain shown in Figure 5.1.

## 5.2 Data Collection and Data Rate

Table 5.1 gives first guess estimates of the dynamic range and accuracy of simulated sensor variables, along with data storage requirements. At 20 bytes per observation per probe and an observing interval of 1 hour that is sufficient for regional analysis and forecasting, a total of 160 bits of data from each probe would be obtained every 3600 seconds, not considering additional bits for error checking, packeting, etc. Remote transmission of the data would be well within the bit-rate capability of prototype systems (Kahn et al. 2000). A rough estimate of the data rate produced by a network of  $10^{10}$  probes as outlined in the grand vision, would be  $\sim 10^{12}$  observations per day if temperature, pressure, humidity, and wind velocity are retrieved once per hour.

Variable	Dynamic Range	#bytes	Accuracy
Temperature	-80 to +40°C	1	+/- 1°C
Pressure	50 to 1050 hPa	2	+/- 1 hPa
Humidity	10 to 100 %	1	+/- 5%
Latitude	-90 to +90°	3	+/- 0.001°
Longitude	0 to 360°	3	+/- 0.001°
Altitude	-1 to +20 km	2	+/- 100 m
Time	$t_0 + 10^7$ s	4	+/- 10 s
Probe ID	1 to $10^9$	4	N/A

Phase II studies will be required to determine whether it is even practical, cost effective, and necessary to achieve and sustain 1-km global coverage based on trade-offs between the number of probes and their impacts on weather forecasts. The OSSEs discussed in Section 4 provide a framework to conduct trade-off studies between MEMS functions such as sense, compute, and transmit capabilities (as outlined by Kahn et al. 2000), and weather forecast accuracy.

A recent report from the NASA Earth Science Enterprise Computational Technology Requirements workshop (NASA 2002) projects  $\sim 10^{10}$  observations per day based on all future satellite observing systems for use in operational NWP models by 2010. The report also notes that computer requirements in 2010 will be inadequate to handle this volume of data given the current model and DA algorithms. In a similar analysis, Uccellini et al. (2001) anticipate a 5-order of magnitude increase from the current  $\sim 10^6$  to  $10^{11}$  upper-air observations per day within 10 years primarily due to planned operational satellite instruments. Although data rates from a global GEMS network are comparable with future observing systems in the next decade, there are

still substantial challenges for data communication and management which will require new paradigms for data mining, sampling and selection techniques, and optimization of observing systems (NASA 2002).

From the weather forecast point-of-view, the usefulness of meteorological observations decreases rapidly with time. As a result, future advances in the speed of internet data transfer will also be required to assure that data flow from collection nodes to central processing and relay sites is fast enough so that data can be assimilated by models to produce forecasts with useful lead-times. NASA's "Vision Architecture Study" (VAS), prepared for the Earth Science Technology Office, assumes tremendous advances in the speed and bandwidth of communication systems to support their sensorweb and model/DA system vision, as well as significant increases in data rates associated mostly with future weather satellite systems (Clausen et al. 2002).

Data collection challenges for GEMS will also be faced within networks, given the large number of probes. The cost of communicating one byte of information across a multihop channel, even with power-optimized communication hardware and protocols, is currently orders of magnitude more expensive (in energy) than performing a numerical computation with the same byte of data. This relationship is likely to become even more unbalanced over the next decade as the power consumption of digital circuits decreases with improved integrated circuit technology, but the power consumption of communication circuits will remain relatively constant, fixed by fundamental noise limits. Under these conditions, filtering and encoding by each probe as data are taken will be critical, along with data fusion from multiple probes as the data traverses the communication tree.

### **5.3 Preliminary Cost Comparison with Other Future Observing Systems**

A quantitative comparison of GEMS with a future observing system necessitates speculative scenarios and projections with large degrees of uncertainty. Nevertheless, long-term planning studies have provided sufficient information to make reasonable estimates. For example, the VAS was designed to identify science knowledge and technology improvements needed to extend the useful skill of weather forecasts from 7 to 14 days by the year 2025 (Clausen et al. 2002). The VAS concluded that the highest priority measurement needs are global 3-D tropospheric wind fields, establishing first-guess spacings of 25 km in the horizontal and 250 m in the vertical with temporal resolutions of 3 hours. These numbers were chosen to be consistent with the resolution of global NWP models expected to be running operationally in the same time frame. Approximately  $6 \times 10^7$  measurements would be required to cover the global atmosphere to a depth of 20 km, sampling into the lower stratosphere in the mid- and high-latitudes.

A rough cost comparison of GEMS with a system that could deliver such global 3-D wind data can be made by following the VAS plan for a constellation of satellites carrying lidar sensors and by using cost estimates from existing and planned weather satellite programs. The cost of NASA's recent 6-year Aqua mission has been estimated at \$952 million (Ray 2002). Based on contract award statistics, the cost to manufacture, launch and deliver to orbit the continuing series of Geostationary Operational Environmental Satellites is about \$200 million per satellite (NOAA 2000). The National Polar-orbiting Operational Environmental Satellite System is projected to provide 6 satellites with an average lifetime of 5 to 6 years and a program cost exceeding several billion dollars (NOAA 2002).

An average expenditure of \$100 million dollars per year per satellite, including manufacturing, launch and operations, appears to be consistent with current and future meteorological satellites. The VAS estimated that a constellation of 10 to 20 satellites with lidar sensors would be required to provide global coverage of 3-D winds every 3 hours. This equates to \$1 to \$2 billion dollars per year, using the estimate of \$100 million per satellite per year. For 3-hour temporal resolution, there would be almost 3000 observing periods per year or just under \$1 million dollars per 3-hour observing period. The effective cost per wind observation would be about one penny, assuming  $6 \times 10^7$  observations.

For GEMS to be cost-equivalent with the scenario outlined above on a per observation basis, each probe providing wind observations every 3 hours for about ten days (i.e. ~80 observations), would have to cost a dollar or less, including deployment. However, the analysis did not consider that the lidar-based satellite constellation will provide only wind observations whereas GEMS would provide 4 times the number of parameters (winds, temperature, moisture, and pressure) at much less than 4 times the cost per observation. Nevertheless, this per-unit cost is in line with projections that probes would cost roughly \$1.00 each in 10 years, with a further decrease to \$0.10 in the following decade.

The decrease in probe costs by an order of magnitude in the 10–20 year time frame would allow an increase in the global horizontal resolution from 25 km to about 8 km, keeping development costs comparable to the VAS vision of a constellation of satellite-borne lidar wind sensors. Sub-cubic millimeter GEMS would be so small and light, roughly a few milligrams each, that a 10 kg payload aboard an aircraft, UAV, or stratospheric balloon would provide millions of probes, keeping deployment costs per probe to a minimum. Even if satellite launch costs decreased significantly via miniaturization of components for satellite buses and sensors using MEMS and nanotechnology (Jilla and Miller 1997), probe costs for GEMS would also likely decrease dramatically once mass production was implemented.

#### 5.4 Environmental Impact

In Phase I, a preliminary examination of the potential environmental impacts of the GEMS probes was conducted based on the number, size, mass, and rate of scavenging from the atmosphere relative to other natural and anthropogenic constituents. Some simple calculations were made and the data were compared to the impacts of current known quantities.

If the probes are distributed globally with 1-km horizontal and vertical spacing up to 20 km, there would be approximately  $10^{10}$  probes covering the earth. At a 10% loss per day, replenishment would require about  $10^9$  probes per day or  $3.65 \times 10^{11}$  probes per year. Since the surface area of the earth is  $5 \times 10^{14} \text{ m}^2$  ( $5 \times 10^8 \text{ km}^2$ ), the probes would fall out at a rate of 1 probe per  $37 \text{ m}^2$  area per year, which is the area of a typical suburban lot. The estimated mass of a probe will be approximately 2500  $\mu\text{g}$ . Therefore the mass per square meter based on the coverage computed above would be approximately 2  $\mu\text{g}$  per year. That amount is negligible compared to the 2 g of African dust that settle on each square meter of Miami every year (Prospero 1999).

Based on specific applications, the probes will be as small as 50-100 microns in one or more dimensions which is about 10 times larger than the particulate size regulation for the current National Ambient Air Quality Standards (NAAQS; EPA 1997). The NAAQS for particulate matter of 10 microns in size is  $50 \mu\text{g m}^{-3}$  as an annual average and  $150 \mu\text{g m}^{-3}$  for a 24-hour average. The estimated concentration of probes in the atmosphere would be 1 probe per cubic kilometer. Assuming that each probe has a mass of 2500  $\mu\text{g}$ , this produces a concentration of 2500  $\mu\text{g}$  per  $10^9$  cubic meters or  $2.5 \times 10^{-6} \mu\text{g m}^{-3}$  that is orders of magnitude lower than the ambient standards.

## 6 Summary

The Phase I project focused on validating the viability of GEMS, defining the major feasibility issues, and determining the primary enabling technologies that must be clearly addressed for the future design and development of the system. A summary of key issues and enabling technologies affecting the design and development of GEMS is presented in Table 6.1.

<b>Major Feasibility Issues</b>	<b>Primary Enabling Technologies</b>
Probe design	Materials science, nanotechnology, biomimetics
Power	Batteries, micro fuel cells, solar energy
Communication	MEMS-based RF and/or free-space optical systems
Navigation	GPS, MEMS-based accelerometers/gyroscopes
Networking	Artificial intelligence (autonomous self-healing networks)
Measurement	MEMS-based pressure, temperature, humidity sensors
Deployment/dispersion	Numerical weather prediction and Lagrangian particle models
Data impact	Observing system simulation experiments
Data collection/management	Artificial intelligence, data mining
Cost	MEMS mass production and packaging, deployment strategies, networking and data collection infrastructure
Environmental	Biodegradable and/or bioinert materials

**Probe Design:** The size, mass, aspect ratio, component geometry, buoyancy control, and aerodynamic design will all determine how long probes remain airborne. Buoyancy control could be the most effective way to reduce the terminal velocity of probes and keep them suspended for longer periods of time. Depending on the size and shape of the probes, aerodynamic design could also reduce their ballistic coefficient and terminal velocity. Based on specific applications, the probes will be as small as 50–100 microns in one or more dimensions and lightweight enough to pose virtually no danger upon contact with persons or property.

**Power:** Power for the probes will likely come from a combination of batteries, fuel cells, and solar energy. Fuel cells are a very promising long-term solution for autonomous system power generation because their energy densities are dramatically higher than that of batteries. Both battery series resistance and fuel cell operation presents a challenge in the colder temperatures in the upper atmosphere.

**Communication:** The probes themselves are the critical element, but they will communicate with, at a minimum, some form of data collection nodes. If probe communications are handled using active RF transmissions, the power requirements are projected to be 100 times greater than free-space optical communication. Communication from airborne probes using optical frequencies can have some advantages over using RF due to the high antenna gains available when the wavelength is small; however, optical signals cannot penetrate areas of dense cloud cover.

**Navigation:** GPS and network localization will be viable long-term options for probe navigation. Advances in GPS satellite technology and the implementation of GPS satellites that broadcast stronger signals could dramatically reduce the energy requirements for making probe position measurements. With network localization, only a fraction of the probes would have knowledge of their locations, and the remaining probes would estimate their positions dynamically.

**Networking:** A critical challenge for GEMS is to define a viable networking solution given available power and probe separation. The probe separation distance as well as power constraints and communication range will determine if each probe can transmit to a remote receiving station or if mobile networking via multihop routing is viable. To study the network design issues in detail as part of the Phase II effort, it will be necessary to consider fault tolerance, scalability, production costs, operating environment, network topology, hardware constraints, transmission media, and power consumption.

**Measurement:** The probes will have to be robust enough to ensure that the electronics are isolated from the effects of liquid and frozen water, dust, chemical pollutants, radiation, and static electricity so MEMS packaging is also an issue (James 2002). It will also be necessary to shield the sensors from the electronics so that they are not affected by thermal noise in the circuits. Existing technology for MEMS-based temperature, humidity, and pressure measurements can be modified for use in integrated, low-power applications such as GEMS.

**Deployment/Dispersion:** The issues relating to probe deployment and dispersion were explored using the ARPS model coupled with a LPM. Since the simulations in Phase I were run for short periods of time ( $\leq 24$  hours), they could not be used to study probe deployment and dispersion over larger spatial and temporal scales. In order to address this issue, the ARPS/LPM were configured to run over most of the northern hemisphere for a period of 24 days, and simulate probe release from a hypothetical network of high altitude balloons. This simulation demonstrated that the large-scale atmospheric circulation patterns can disperse probes throughout the northern hemisphere in just 10 days with such a deployment scenario.

**Data Impact:** OSSEs were used to assess the impact of simulated probe data on forecasts of the selected weather event within a regional domain. The assimilation of simulated probe data resulted in a substantial reduction of forecast errors and improvements in the predicted precipitation patterns. Excluding temperature, moisture, or wind data in the OSSE framework significantly degraded the model forecast not only for the parameter excluded, but for the precipitation forecast as well. This sensitivity test indicated that, at least for case studied, the maximum data impact resulted when GEMS provided a full suite of temperature, moisture, pressure, and wind measurements.

**Data Collection/Management:** Although data rates from a global GEMS network of  $10^{10}$  probes are comparable with future observing systems in the next decade, there are still substantial challenges for data communication and management which will require new paradigms for data mining, sampling and selection techniques, and optimization of observing systems. Since the usefulness of meteorological observations decreases rapidly with age, future advances in the speed of data transfer will also be required. Data flow from collection nodes to central processing and relay sites will need to be fast enough so that data can be assimilated

by models to produce forecasts with useful lead-times. Data collection challenges for GEMS will also be faced within networks, given the large number of probes.

**Cost:** A preliminary cost comparison of GEMS with a future observing system was performed based on 10 to 20 satellites with lidar sensors that could provide global coverage of 3-D winds every 3 hours. On a per observation basis, the cost of GEMS would be equivalent to such a satellite-based observing system if each probe were manufactured for less than \$1.00. However, the analysis did not consider that the lidar-based satellite constellation will provide only wind observations whereas GEMS could provide 4 times the number of parameters (winds, temperature, moisture, and pressure) at much less than 4 times the cost per observation.

**Environmental:** Even at the smallest projected size, there is little concern that probes will alter the weather since they will be too large and too low in concentration to seed clouds like aerosols. Materials science will play a key role to limit probe mass and potentially make them biodegradable or bioinert, thereby minimizing risks to the environment when the probes settle out of the atmosphere. A preliminary examination of the potential environmental impacts of the GEMS probes was conducted based on the number, size, mass, and rate of scavenging from the atmosphere relative to other natural and anthropogenic constituents. Given the approximate mass of a single probe, the mass density would be about six orders of magnitude less than African dust and well within the ambient air-quality standards set by the Environmental Protection Agency.

## 7 Future Direction

The future direction for a NIAC Phase II project will require studying the major feasibility issues from Table 6.1 in detail to examine the potential performance and cost benefits, and developing a technology roadmap that will help NASA to integrate the GEMS into future missions and/or programs. As in Phase I, extensive use of modeling in the SDT cycle is envisioned as a cost-effective and controlled way to explore the complex trade-offs, mapping out logical and self-consistent pathways for further exploration. It will be important to formulate an overall system model of GEMS in Phase II following guidelines for systems engineering that will link together results from the SDT cycle and provide a pathway for developing the technology roadmap.

The major feasibility issues will be studied in Phase II by focusing on fundamental physical limitations for measurement and signal detection based on noise sources, scaling as the individual probes become smaller and the number of probes in the network becomes larger, and disciplined engineering optimization of the trade-offs which affect the cost, practicality, and feasibility of the overall system. The following bullets highlight specific plans that focus on the key issues identified in Table 6.1.

- Examine trade-offs to optimize the overall design of the individual probes in terms of size, shape, functionality, and cost as guided by requirements for deployment and dispersion. If necessary, Computer-Aided Design software can be used to explore the layout of probe components and determine if particular configurations are feasible and cost-effective.
- Develop a detailed power budget based on the fundamental limitations of the candidate sources identified in Phase I, along with the projected power requirements of all probe functions. As part of an optimization exercise using simple models, first-order power approximations can be developed and refined based on results from studying the other feasibility issues within the SDT cycle.
- Determine whether the viable communication and networking algorithms are scalable to regional and planetary networks, and which capabilities are critical before such networks become practical and cost effective in the 10–20 year timeframe. As the scalability of communications and networking is better understood, this information can be used in the data impact experiments to study deployment strategies and the number of probes necessary to improve NWP.
- Examine the trade-offs and cost for GPS navigation based on projected advancements to the satellite constellation and receivers.
- Determine if network localization is scalable and can be accomplished given power requirements and on-board processing power as the network size increases from hundreds to potentially millions of probes.

- Explore how much observational error can be tolerated for each parameter before degrading forecasts to some pre-determined threshold. This error tolerance will determine if any further improvements in sensor accuracy are necessary and justifiable in terms of probe cost and design complexity.
- Study probe dispersion, scavenging, and resulting distributions for several potential deployment strategies on a hemispheric scale for a period of 10 to 30 days to determine the practicality of such strategies.
- Study the data impact on NWP forecast accuracy using the OSSE framework for the most feasible deployment scenarios based on the probe dispersion results.
- Perform detailed cost-benefit analyses to explore the costs associated with building and implementing GEMS, weighed against the benefits derived from the improved weather forecasts that will result from the data. Included in this cost analysis will be a quantitative comparison of GEMS with future observing systems.
- Examine environmental, legal, and political implications of international trans-boundary movement of probes to determine if there are relevant national and international laws, treaties, or regulations governing their release and dispersion.
- Determine if the concentration of probes under various deployment scenarios would be high enough to interfere with weather and aviation radar surveillance.

## **8 Acknowledgements**

The principal investigator, Dr. John Manobianco, would like to thank ENSCO GEMS project team members Dr. David A. Short, Mr. Jonathan L. Case, and Mr. Randolph J. Evans for their outstanding technical and scientific contributions to this Phase I effort and the consultant on the project, Dr. Kristofer S. J. Pister from the University of California Berkeley, who provided MEMS and engineering expertise including all of the material presented in Section 3 of this report.

The GEMS project team gratefully acknowledges Dr. Francis Merceret from the NASA Kennedy Space Center Weather Office for granting access to the Applied Meteorology Unit Linux cluster of 32 Pentium III, 933-MHz processors used for the ARPS simulations. The team also thanks Drs. Kelvin Droegemeier, Ming Xue, and Keith Brewster from the Center for Analysis and Prediction of Storms at the University of Oklahoma for consultations regarding ARPS, and Ms. Donna Manobianco for numerous contributions including the concept acronym, on-line research, creative input regarding the use of nanobiotechnology, and editing of the Phase I proposal and final report.

Mention of a copyrighted, trademarked or proprietary product, service, or document does not constitute endorsement thereof by the authors, ENSCO, Inc., NASA, NIAC, or the U.S. Government. Any such mention is solely for the purpose of fully informing the reader of the resources used to conduct the work reported herein.

## 9 References

- Adrian, P., 2001: Wireless integrated microsystems will enhance information gathering and transmission. *Sensor Business Digest* (September issue). [Available on line at <http://www.sensorsmag.com/resources/businessdigest/main.shtml>].
- Akyildiz, I. F., W. Su, Y. Sankarasubramaniam, and E. Cayirci, 2002: Wireless sensor networks: a survey. *Networks*, **38**, 393-422.
- Allen, J. J., and Coauthors, 1998: Integrated micro-electro-mechanical sensor development for inertial applications, *Position Location and Navigation Symposium*, Rancho Mirage, CA, IEEE, 9-16.
- Aluminum Power, Inc. 2001: Aluminum: The latest fuel in the power revolution. [Available on line at <http://www.fuelcell-magazine.com/articles/april01-2.htm>. See also <http://www.aluminum-power.com/>].
- Analog Devices, 2002: Accelerometers and Gyroscopes. [Available on line at <http://www.analog.com/technology/mems/index.html>].
- Arnold, C. P. Jr., and C. H. Dey, 1986: Observing-system simulation experiments: Past, present, and future. *Bull. Amer. Meteor. Soc.*, **67**, 687-695.
- Atlas, R., 1997: Atmospheric observations and experiments to assess their usefulness in data assimilation. *J. Royal Meteor. Soc. Japan*, **75**, 111-130.
- Aylor, D. E., and T. B. Sutton, 1992: Release of *Venturia inaequalis* ascospores during unsteady rain: relationship to spore transport and deposition. *Phytopathology*, **82**, 532-540.
- Bacon, D. A., and R. A. Sarma, 1991: Agglomeration of dust in convective clouds initialized by nuclear bursts. *Atmosphere Environ.*, **25A**, 2627-2642.
- Ball Aerospace, 2002: Fast steering mirrors. [Available on line at <http://www.ball.com/aerospace/fsm.html>].
- Baltes, H., A. Koll, and D. Lange, 1997: The CMOS MEMS nose – fact or fiction?. *Proc. of the Int. Symp. On Indust. Elect. (ISIE '97)*, Guimares, Portugal, SS152-157.
- Bates, J.B.; N. J. Dudney, B. Neudecker, A. Ueda, and C. D. Evans, 2000: Thin-film lithium and lithium-ion batteries, *Solid State Ionics*, **135**, 33-45.
- Benjamin, S. G., J. M. Brown, K. J. Brundage, D. Devenyi, B. E. Schwartz, T. G. Smirnova, T. L. Smith, L. L. Morone, and G. J. DiMego, 1998: The operational RUC-2. *Sixteenth Conf. on Weather Analysis and Forecasting*, Phoenix, AZ, Amer. Meteor. Soc., 249-252.
- Bloom, S. C., L. L. Takacs, A. M. da Silva and D. Ledvina, 1996: Data assimilation using incremental analysis updates. *Mon. Wea. Rev.*, **124**, 1256-1271.
- Bluetooth, 2002: Bluetooth, How it works. [Available on line at <http://www.bluetooth.com>].
- Boltshauser, T., C. A. Leme, P. O'Leary, and H. Baltes, 1993: Humidity sensors with on-chip absolute capacitance measurement system. *Sensors & Actuators B*, **15/16**, 75-80.
- Bratseth, A., 1986: Statistical interpolation by means of successive corrections. *Tellus*, **38A**, 439-447.
- Brewster, K., 1996: Application of a Bratseth analysis scheme including Doppler radar data. Preprints, *Fifteenth Conf. on Weather Analysis and Forecasting*, Amer. Meteor. Soc., Norfolk, VA, 92-95.
- Cambridge Technologies, 2002: Galvanometers. [Available on line at <http://www.camtech.com>].

- Chambers, A., C. Park, R. T. K. Baker, and N. M. Rodriguez, 1998: Hydrogen storage in graphite nanofibers. *Journal of Physical Chemistry*, **B 102**, 4253-4256.
- Chen, P., X. Wu, J. Lin, and K. L. Tan, 1999: High H-2 uptake by alkali-doped carbon nanotubes under ambient pressure and moderate temperatures. *Science*, **285**, 91-93.
- Clausen, M., M. Kalb, G. McConaughy, R. Muller, S. Neeck, M. Seablom, and M. Steiner, 2002: Advanced weather prediction technologies: NASA's contribution to the operational agencies. Study report prepared for NASA's Earth Science Technology Office, May 2002, 93 pp.
- Coldren, L. A., S. P. DenBaars, O. Buchinsky, T. Margalith, D. A. Cohen, A. C. Abare, and M. Hansen, 1998: Blue and Green InGaN VCSEL Technology. Final Report for MICRO Project 97-033, 4 pp. [Available on line at [http://www.ucop.edu/research/micro/97\\_98/97\\_033.pdf](http://www.ucop.edu/research/micro/97_98/97_033.pdf)].
- Conant, R., J. Nee, K. Lau, and R. Muller, 2000: A fast flat scanning micromirror. *IEEE Solid-state Sensor and Actuator Workshop*, Hilton Head, SC, 6-9.
- DARPA, 2002a, MicroPower Generation. [Available on line at <http://www.darpa.mil/mto/mpg/overview/index.html>].
- DARPA, 2002b, Metamaterials. [Available on line at <http://www.darpa.mil/dso/TextOnly/future/metamaterials/metamaterials.html>].
- DARPA, 1998: Ultra photonics. [Available on line at <http://www.darpa.mil/mto/ultraphotonics/overview/ucsb3.html>].
- De Pondeca, M. S. F. V., and X. Zou, 2001: Moisture retrievals from simulated zenith delay "observations" and their impact on short-range precipitation forecasts. *Tellus*, **33A**, 192-214.
- Deardorff, J. W., 1980: Stratocumulus-capped mixed layers derived from a three-dimensional model. *Bound.-Layer Meteor.*, **7**, 199-226.
- Delin, K. A., and S. P. Jackson, 2000: Sensor Web for in situ exploration of gaseous biosignatures. Proceedings, *Aerospace Conference 2000*, **7**, IEEE, Big Sky, MT, 465-472.
- Doherty, L., B. Warneke, B. Boser, and K. S. J. Pister, 2002: Energy and performance considerations for Smart Dust. *Intl. J. Parallel and Distributed Systems and Networks*, 121-133.
- Du, Z., K. Gong, J. S. Fu, and B. Gao, 2001: Analysis of microstrip fractal patch antenna for multi-band communication [by FDTD]. *Electronics Letters*, **37**, 805-806.
- Dutton, J. A., 2002: Opportunities and priorities in a new era for weather and climate services. *Bull. Amer. Meteor. Soc.*, **83**, 1303-1312.
- EPA, 1997: U.S. Environmental Protection Agency's updated clean air standards. [Available on line at: [http://www.epa.gov/ttnnaqs/standards/pm/s\\_pm\\_index.html](http://www.epa.gov/ttnnaqs/standards/pm/s_pm_index.html)].
- Eveready, 2002a: Energizer AC675 button cell. [Available on line at [http://data.energizer.com/batteryinfo/product\\_offerings/zinc\\_air/zinc\\_air.htm](http://data.energizer.com/batteryinfo/product_offerings/zinc_air/zinc_air.htm)].
- Eveready, 2002b: Energizer zinc air (Zn/O<sub>2</sub>) batteries. [Available on-line at [http://data.energizer.com/batteryinfo/application\\_manuals/zinc\\_air.htm](http://data.energizer.com/batteryinfo/application_manuals/zinc_air.htm)].
- Franklin, J. L., L. A. Avila, J. L. Bevin, M. B. Lawrence, R. J. Pasch, and S. R. Stewart, 2001: Atlantic hurricane season of 2000. *Mon. Wea. Rev.*, **129**, 3037-3056.
- Girz, C. M. I. R, and Coauthors, 2002: Results of the demonstration flight of the GAINS prototype III balloon. Preprints, *Sixth Symp. On Integrated Observing Systems*, Amer. Meteor. Soc., Orlando, FL, 248-253.

- Gosele, U. M., 1998: Fast diffusion in semiconductors. *Annual review of materials science*, Huggins, R.A., Giordmaine, J.A., Wachtman, J.B., Jr., eds., **18**, Palo Alto, CA, 257-282.
- Green M. A, K. Emery, D. L. King, S. Igari, and W. Warta, 2001: Solar cell efficiency tables. [Available on line at <http://www.pv.unsw.edu.au/eff/>].
- Gtierrez, R. C, T. K. Tang, J. Wilcox, W. J. Kaiser, C. B. Stell, V. Vorperian, and K. V. Shcheglov, 2001: Pressure sensor based on measurement of vibration damping. *NASA Tech. Brief*, **25**. [Available on line at <http://www.nasatech.com/Briefs/June01/NPO20052.html>].
- Hierlemann, A., D. Lange, C. Hagleitner, N. Kerness, A. Koll, O. Brand, and H. Baltes, 2000: Application-specific sensor systems based on CMOS chemical microsensors. *Sensors & Actuators B*, **70**, 2-11.
- Hitachi, 2002: Coil on a chip RF-ID systems. [Available on line at <http://www.maxell.co.jp/e/products/industrial/rfid/siyou.html>].
- Hoenk, M., T. VanZandt, D. Cheng, and W. Kaiser: 1996. Surface acoustic wave hygrometer: measuring water vapor in Earth's atmosphere. [Available on line at [http://mishkin.jpl.nasa.gov/spacemicro/MWS\\_PAPER](http://mishkin.jpl.nasa.gov/spacemicro/MWS_PAPER)].
- Holland, G. J., and Coauthors, 2001: The aerosonde robotic aircraft: A new paradigm for environmental observations. *Bull. Amer. Meteor. Soc.*, **82**, 889-901.
- IMI, 2002: Integrated Micro Instruments. [Available on line at <http://www.imi-mems.com/>].
- James, K., 2002: For MEMS, the key to lowering cost is all in the packaging. *Small Times* [Available on line at [http://www.smalltimes.com/document\\_display.cfm?document\\_id=5079](http://www.smalltimes.com/document_display.cfm?document_id=5079)].
- Jilla, C. D., and D. W. Miller, 1997: Satellite design: Past, present and future. *International Journal of Small Satellite Engineering*. [Available on line at <http://www.ee.surrey.ac.uk/Research/CSER/UOSAT/IJSSE/issue1/issue1.html>].
- Kahn, J. M., R. H. Katz, and K. S. J. Pister, 2000: Emerging challenges: mobile networking for Smart Dust. *J. of Commun. and Networks*, **2**, 188-196.
- Kalnay, E., and Coauthors, 1996: The NCEP/NCAR 40-year reanalysis project. *Bull. Amer. Meteor. Soc.*, **77**, 437-471.
- Kovacs, G. T. A., 1998: *Micromachined Transducers Sourcebook*. McGraw-Hill, New York, 944 pp.
- Kuo, Y.-H., X. Zou, and W. Huang, 1997: The impact of Global Positioning System data on the prediction of an extratropical cyclone: an observing system simulation experiment. *Dyn. Atmos. Oceans*, **27**, 439-470.
- Last, M, B. Fisher, C. Ezekwe, S. Hubert, S. Patel, S. Hollar, B. Leibowitz, and K. S. J. Pister, 2001: Video semaphore decoding for free-space optical communication, Proceedings, *SPIE*, **4303**, San Jose, CA, 21-26.
- Last, M., and K. S. J. Pister, 2000: An 8 mm<sup>3</sup> digitally steered laser beam transmitter. Proceedings, *2000 IEEE/LEOS Conference on Optical MEMS*, Kauai, HI, 69-70.
- Laville, C., and C. Pellet, 2002: Comparison of three humidity sensors for a pulmonary function diagnosis microsystem. *IEEE Sensors Journal*, **2**, 304-309.
- Lee, W. C.-Y., 1995: *Mobile Cellular Communications*, 2nd. Ed., McGraw-Hill.
- Lei, C., H. Deng, J. J. Dudley, S-F. Lim, B. Liang, M. Tashima, and R. W. Herrick, 1999: Manufacturing of oxide VCSEL at Hewlett Packard. [Available on line at <http://www.ieee.org/organizations/pubs/newsletters/leos/aug99/article6.htm>].

- Lord, S. J., E. Kalnay, R. Daley, G. D. Emmitt, and R. Atlas, 1997: Using OSSEs in the design of the future generation of integrated observing systems. Preprints, *First Symposium on Integrated Observing Systems*, Amer. Meteor. Soc., Long Beach, CA, 45-47.
- Lorenz, E. N., 1969: The predictability of a flow which possesses many scales of motion. *Tellus*, **21**, 289-307.
- Madou, M. J., and S. R. Morrison, 1989: *Chemical Sensing with Solid-State Devices*. Academic Press, Inc. New York, 547 pp.
- Martin, S. J., G. C. Frye, J. J. Spates, and M. A. Butler, 1996: Gas sensing with acoustic devices. *Proc. IEEE Ultrasonic Symposium*, San Antonio, TX, 423- 433.
- Matsuguchi, M., T. Kuroiwa, T. Miyagishi, S. Suzuki, T. Ogura, and Y. Sakai, 1998: Stability and reliability of capacitive-type relative humidity sensors using cross-linked polyimide films. *Sensors & Actuators B*, **52**, 53-57.
- Mellor, G. L., and T. Yamada, 1982: Development of a turbulence closure model for geophysical fluid problems. *Rev. Geophys. Space Phys.*, **20**, 851-875.
- Milanovic, V., M. Last, and K. S. J. Pister, 2001: Torsional micromirrors with lateral actuators. *Transducers 2001*, Muenchen Germany.
- Murphy, A. H., 1988: Skill scores based on the mean square error and their relationships to the correlation coefficient. *Mon. Wea. Rev.*, **116**, 2417-2424.
- NASA, 2002: Report from the NASA Earth Science Enterprise Computational Technology Requirements Workshop. 30 April – 1 May 2002. [Available on line at <http://esto.gsfc.nasa.gov/>].
- Nascatec, 2002: Products. [Available on line at <http://www.nascatec.com/products.html>].
- Nguyen, C. T.-C., 1999: Frequency-selective MEMS for miniaturized low-power communication devices. *IEEE Trans. Microwave Theory Tech.*, **47**, 486-1503.
- \_\_\_\_\_, 2001: Vibrating RF MEMS for low power wireless communication. *Proceedings, 2000 Int. MEMS Workshop (iMEMS '01)*, Singapore, Japan, 21-34.
- NOAA, 2000: NOAA's environmental satellites: A history. [Available on line at <http://www.noaanews.noaa.gov/stories/s402b.htm>].
- NOAA, 2002: The National Polar-orbiting Operational Environmental Satellite System (NPOESS). [Available on line at <http://www.publicaffairs.noaa.gov/grounders/npoess.html>].
- NSIDC, 2002: Radiosonde systems, Historical Arctic Rawinsonde Archive (HARA). [Available on line at [http://nsidc.org/data/docs/daac/radiosondes\\_instrument.gd.html](http://nsidc.org/data/docs/daac/radiosondes_instrument.gd.html)].
- Nutter, P. A., and J. Manobianco, 1999: Evaluation of the 29-km Eta model. Part I: Objective verification at three selected stations. *Wea. Forecasting*, **14**, 5-17.
- NWS, 2002: Upper air observations program. [Available on line at <http://www.ua.nws.noaa.gov/>].
- OFCM, 1997: National plan for tropical cyclone research and reconnaissance (1997-2000). FCM-P25-1997, 137 pp. [Available online from the Office of the Federal Coordinator for Meteorology at <http://www.ofcm.gov/homepage/text/pubs.htm>].
- Ohmori, M., T. Takamoto, E. Ikeda and H. Kurita, 1996: High efficiency InGaP/GaAs tandem solar cells. *Tech. Digest, International PVSEC-9*, Miyasaki, Japan, November 1996, 525-528.

- Pankine, A. A., E. Weinstock, M. K. Heun, and K. T. Nock, 2002: In-situ science from global networks of stratospheric satellites. Preprints, *Sixth Symp. On Integrated Observing Systems*, Amer. Meteor. Soc., Orlando, FL, 260-266.
- PhysikInstrumente, 2002: Fast steering mirrors, piezo tip/tilt platforms. [Available on line at <http://katalog.physikinstrumente.com/TOCs/3index.html>].
- Pielke, R. A., and Coauthors, 1997: Workshop on the societal and economic impacts of weather, 2-4 April 1997. [Available online at <http://sciencepolicy.colorado.edu/socasp/weather1>].
- Prospero, J. M, 1999: Long-term measurements of the transport of African mineral dust to the southeastern United States: Implications for regional air quality. *J. Geo. Research*, **104**, 15917-15927.
- Qui, Y. Y., C. Azeredo-Leme, L. R. Alcacer, and J. E. Franca, 2001: A CMOS humidity sensor with on-chip calibration. *Sensors & Actuators A*, **92**, 80-87.
- Ray, J, 2002: New environmental eye on Earth launched into space, 4 May 2002. [Available on line at <http://spaceflightnow.com/delta/d291/>].
- RF-ID, 2002, 2.4 GHz tag products. [Available on line at <http://www.rf-id.com/24ghztag.htm> RF-ID02].
- Rohaly, G. D., and T. N. Krishnamurti, 1993: An observing system simulation experiment for the Laser Atmospheric Wind Sounder (LAWS). *J. Applied Meteor.*, **32**, 1453-1471.
- Rogers, E., T. L. Black, D. G. Deaven, G. J. DiMego, Q. Zhao, M. Baldwin, N. W. Junker, and Y. Lin, 1996: Changes to the operational “early” eta analysis/forecast system at the National Centers for Environmental Prediction. *Wea. Forecasting*, **11**, 391-413.
- Rossing, T. D., and N. H. Fletcher, 1995: *Principles of Vibration and Sound*, Springer-Verlag, New York, 247 pp.
- Sarna-Wojcicki, A.M., S. Shipley, S., R. B. Waitt, D. Dzurisin, and S. H. Wood, 1981: Areal distribution, thickness, mass, volume, and grain size of air-fall ash from six major eruptions of 1980. The 1980 eruptions of Mount St. Helens. *U.S. Geological Survey Professional Paper 1250*, 577-600.
- Savvides, A., C. Han, and M. Srivastava, 2001: Dynamic fine-grained localization in ad-hoc networks of sensors. Proceedings, *ACM MobiCom 2001*, Rome, Italy, 166-179.
- Seinfeld, J. H., and S. N. Pandis, 1998: *Atmospheric Chemistry and Physics – From Air Pollution to Climate Change*, John Wiley and Sons Inc., New York, 1326 pp.
- Shuman, F., 1989: History of numerical weather prediction at the National Meteorological Center. *Wea. Forecasting*, **4**, 286-296.
- Soong, R. K., and Coauthors, 2000: Powering an inorganic nanodevice with a biomolecular motor. *Science*, **290**, 1555-1558.
- Sze, S. M. (ed), 1994: *Semiconductor Sensors*. John Wiley & Sons, Inc., New York, 576 pp.
- Tadiran, 2002: Tadium lithium batteries. [Available on line at <http://www.tadiranbat.com/compare.htm>].
- Uccellini, L., and Coauthors, 2001: Weather prediction improvement using advanced satellite technology. Preprints, *Eleventh Conf. on Satellite Meteorology and Oceanography*, Amer. Meteor. Soc., Madison, WI, 216-219.
- Unninayar, S., and R. A. Schiffer, 1997: *In-situ Observations for the Global Observing Systems, A Compendium of Requirements and Systems*, Office of Mission to Planet Earth, NASA, Chapter 1. [Available online at <http://www.earth.nasa.gov/visions/insitu/chap1.htm>].

- Vaisala, 2002: *RS90 Radiosondes*. [Available on line at [http://www.vaisala.com/DynaGen\\_Attachments/Att2749/2749.pdf](http://www.vaisala.com/DynaGen_Attachments/Att2749/2749.pdf)].
- Walker, J., 1981: The aerodynamics of samara: winged seed of the maple, the ash, and other trees. *Sci. American*, **Oct.**, 226-237.
- Walko, R. L., C. J. Tremback, and M. J. Bell, 2001: Hybrid particle and concentration transport model (HYPACT) user's guide, version 1.2.0. [Available on-line from <http://www.atmet.com/html/docs/hypact/1.2.0/hypact.htm>].
- Wilson, K, and M. Enoch, 2000: Optical communications for deep space missions. *IEEE Communications Magazine*, **August**, 134-139.
- Xue, M., K. K. Droegemeier, and V. Wong, 2000: The Advanced Regional Prediction System (ARPS) — A multi-scale nonhydrostatic atmospheric simulation and prediction model. Part I: Model dynamics and verification. *Meteor. Atmos. Phys.*, **75**, 161-193.
- \_\_\_\_\_, and Coauthors, 2001: The Advanced Regional Prediction System (ARPS) — A multiscale nonhydrostatic atmospheric simulation and prediction tool. Part II: Model physics and applications. *Meteor. Atmos. Phys.*, **76**, 143-165.
- Zhao, J., A. Wang, M. Green and F. Ferrazza, 1998: Novel 19.8% efficient “honeycomb” textured multicrystalline and 24.4% monocrystalline silicon solar cell. *Appl. Phys. Letters*, **73**, 1991-1993.

## List of Abbreviations

<b>Term</b>	<b>Description</b>
3-D	Three-Dimensional
ADAS	ARPS Data Analysis System
ADC	Analog to Digital Conversion
ARPS	Advanced Regional Prediction System
CCD	Charge Coupled Device
CMOS	Complementary Metal-Oxide Semiconductor
DA	Data Assimilation
DARPA	Defense Advanced Research Projects Agency
DC	Direct Current
GEMS	Global Environmental MEMS Sensors
GPS	Global Positioning System
GSM	Global System for Mobile
IAU	Incremental Analysis Update
IC	Integrated Circuit
INS	Inertial Navigation System
ISM	Industrial, Scientific, and Medical
LEO	Low Earth Orbiting
LPM	Lagrangian Particle Model
MEMS	MicroElectroMechanical Systems
MPI	Message Passing Interface
NAAQS	National Ambient Air Quality Standards
NDVI	Normalized Difference Vegetation Index
NIAC	NASA Institute for Advanced Concepts
NOGAPS	Navy Operational Global Atmospheric Prediction System
NWP	Numerical Weather Prediction
OI	Optimum Interpolation
OSSE	Observing System Simulation Experiment
PTAT	Proportional-To-Absolute-Temperature
Q	Quality factor
RF	Radio Frequency
RH	Relative Humidity
RMS	Root Mean Square
RUC	Rapid Update Cycle
SCM	Successive Corrections Method

SD	Standard Deviation
SDT	Simulation-Design-Test
SGS	Sub-Grid Scale
SNR	Signal to Noise Ratio
TKE	Turbulent Kinetic Energy
UAV	Unmanned Aerial Vehicle
UC	University of California
VAS	Vision Architecture Study
VCSEL	Vertical Cavity Surface Emitting Laser